

2018-09

Study of crustacean biomass wastes for water defluoridation

Wagutu, Agatha W.

NM-AIST

<https://doi.org/10.58694/20.500.12479/286>

Provided with love from The Nelson Mandela African Institution of Science and Technology

**STUDY OF CRUSTACEAN BIOMASS WASTES FOR WATER
DEFLUORIDATION**

Agatha W. Wagutu

**A Dissertation Submitted in Partial Fulfillment of the Requirements for the Degree
of Doctor of Philosophy in Materials and Energy Science and Engineering of the
Nelson Mandela African Institution of Science and Technology**

Arusha, Tanzania

September, 2018

ABSTRACT

High levels of fluoride (F^-) in community drinking water supply is recognized as one of the major public health problems. Until now no efficient and affordable F^- removal technology exists in many regions. This research explored crustacean biomass waste for development of adsorbent for F^- removal. Chitin and calcium carbonate components in crabs and prawns shells were selected for development of three adsorbents: chitosan, calcium phosphate systems (CAPs) and composite of chitosan and CAPs. All the adsorbents were characterized using XRD and FT-IR. Chitosan was obtained by deacetylation of chitin and then modified by cross-linking with glutaraldehyde and protonated using hydrochloric acid. Interaction of F^- with the modified chitosan was studied using batch adsorption test and theoretical Density Function Theory (DFT) calculations. Results indicated that computed parameters matched well with experimental results and confirmed that electropositivity of hydrogen atoms influenced F^- adsorption by electrostatic attraction. Best performance was achieved in low F^- polluted water (≤ 5 mg/l) with adsorption capacity 1.6 mg/g. Calcium recovered from demineralization of shells was precipitated into CAPs using ammonium dihydrogen phosphate. Crab shell produced dicalcium phosphate dehydrate or brushite ($CaHPO_4 \cdot 2H_2O$) while prawns shell gave hydroxyapatite ($Ca_5(PO_4)_6(OH)_2$) form of CAPs. Brushite was more effective in F^- adsorption with efficiencies above 92% and highest capacity of 13.6 mg/g in field water with fluoride concentration of 5-70 mg/l compared to prawns shell hydroxyapatite with capacity of 8.5 mg/g. FT-IR analysis and kinetic studies predicted defluoridation occurred by ion exchange and ion adsorption mechanisms, described by pseudo 2nd order kinetics. Failure to remove microbes was identified as limitations of the CAPs. Composite of chitosan and brushite was thus developed to address the problem. Analysis with XRD and FT-IR confirmed transformation of brushite phases into hydroxyapatite and formation hybrid composite. Highest F^- adsorption efficiency (88%) was achieved for water with $F^- \leq 10$ mg/l. Microbial count significantly reduced in treated water and final pH was within the acceptable range of 6-9. Adsorbate-adsorbent interaction was best described by pseudo 2nd order kinetics.

DECLARATION

I, **Agatha W. Wagutu**, do hereby declare to the Senate of Nelson Mandela African Institution of Science and Technology that this dissertation is my own original work and that it has neither been submitted nor being concurrently submitted for degree award in any other institution.

Agatha W. Wagutu _____

Name and signature of candidate

_____ **Date**

The above declaration is confirmed

Dr. Revocatus L. Machunda _____

Name and signature of supervisor 1

_____ **Date**

Dr. Yusufu A. C. Jande _____

Name and signature of supervisor 2

_____ **Date**

COPYRIGHT

This dissertation is copyright material protected under the Berne Convention, the Copyright Act of 1999 and other international and national enactments, in that behalf, on intellectual property. It must not be reproduced by any means, in full or in part, except for short extracts in fair dealing; for researcher private study, critical scholarly review or discourse with an acknowledgement, without a written permission of the Deputy Vice Chancellor for Academic, Research and Innovation, on behalf of both the author and the Nelson Mandela African Institution of Science and Technology.

CERTIFICATION

The undersigned certifies that they have read and hereby recommend for acceptance by the Nelson Mandela Institution of Science and Technology a dissertation titled “*Study of Crustacean Biomass Wastes for Water Defluoridation*” in fulfillment of the requirements for the Degree of Doctor of Philosophy in Materials and Energy Science and Engineering (MESE) at the Nelson Mandela African Institution of Science and Technology (NM-AIST).

Dr. Revocatus L. Machunda _____

Name and signature of supervisor 1

_____ **Date**

Dr. Yusufu A. C. Jande _____

Name and signature of supervisor 2

_____ **Date**

ACKNOWLEDGEMENTS

This dissertation work was carried out under supervision of Dr. Revocatus L. Machunda and Dr. Yusufu A. C. Jande. I am indebted to their support during the period of the study. Many thanks goes to Prof. Tatiana Pogrebnaya for her mentorship in computational chemistry. This lead to combination of computational methods and experimental data in chapter 2 of this work. Prof. Eugene Park laid the foundation of my PhD studies at NM-AIST, all are humbly acknowledged.

Support accorded in all ways by academic and technical staff from schools of MEWES, LiSBE and CoCSE is gratefully acknowledged.

It is with sincere gratitude that I appreciate the African Union Commission for the award of full PhD scholarship under the Mwalimu Nyerere African Union Scholarship Scheme (MNAUSS), 2014-2017.

This project received funding from the European Union's Horizon 2020 research and innovation program, grant agreement Number 690378, under the leadership of Dr. Revocatus L. Machunda.

Finally, most sincere gratitude to my family, all my colleagues, my close friends and relatives for all forms of support accorded during the entire study time.

DEDICATION

To my loved ones: I am because you are.

TABLE OF CONTENTS

ABSTRACT	i
DECLARATION	ii
COPYRIGHT	iii
CERTIFICATION	iv
ACKNOWLEDGEMENTS	v
DEDICATION	vi
TABLE OF CONTENTS	vii
LIST OF TABLES	xi
LIST OF FIGURES	xiii
LIST OF ABBREVIATIONS AND SYMBOLS	xv
CHAPTER ONE	1
General Introduction	1
1.0 Introduction.....	1
1.1 Background.....	1
1.2 Fluoride Occurrence.....	2
1.3 Defluoridation Methods	3
1.3.1 Membrane techniques	3
1.3.2. Adsorption techniques	4
1.3.3 Precipitation techniques	5
1.4 Materials Under Study	5
1.4.1 Chitosan polymer	5
1.4.2 Availability of crustacean waste in Tanzania	7

1.4.3 Calcium phosphate systems	8
1.4.4 Chitosan hydroxyapatite composite	9
1.5 Problem Statement	10
1.6 Justification	11
1.7 Objectives	11
1.7.1 Specific objectives	11
1.8 Dissertation Framework	12
CHAPTER TWO	13
Interaction of Chitosan with Fluoride: Experimental Study and Density Function	
Theory Modelling.....	13
Abstract	13
2.1 Introduction.....	13
2.2 Materials and Method	15
2.2.1 Experimental details.....	15
2.2.2 Computational details	18
2.3 Results and Discussion	18
2.3.1 Properties of chitosan (CHS), protonated cross-linked chitosan (PCCs) and glucosamine (GlcN)	18
2.3.2 Analysis of protonated β -GlcN and PCCs	26
2.3.3 Interaction of F^- with chitosan	28
2.4 Conclusion	33

CHAPTER THREE	35
Crustacean Derived Calcium Phosphate Systems: Application in Defluoridation...	35
Abstract	35
3.1 Introduction.....	35
3.2 Materials and Methods.....	38
3.2.1 Raw materials.....	38
3.2.2 Preparation of CAPs	38
3.2.3 Material characterization	39
3.2.4 Batch adsorption tests	39
3.3 Results and Discussion	40
3.3.1 Preparation of CAPs	40
3.3.2 Characterization of CAPs	41
3.3.3 Batch absorption test.....	46
3.3.4 Effect of pH.....	50
3.3.5 Adsorption isotherms	51
3.3.6 Effect of contact time and adsorption kinetics.....	55
3.3.7 Effect of temperature and thermodynamic parameters	58
3.3.8 Elucidation of F- removal mechanism.....	61
3.4 Conclusion	61
CHAPTER FOUR.....	63
Preparation and Characterization of Chitosan-Calcium Phosphate Composite	63
Abstract	63
4.1 Introduction.....	63

4.2 Materials and Methods.....	65
4.2.1 Raw materials.....	65
4.2.2 Preparation and characterization of chitosan-hydroxyapatite (Cs-HA).....	65
4.2.3 Batch adsorption tests	65
4.3 Results and Discussion	66
4.3.1 Characterization of chitosan - hydroxyapatite	66
4.3.2 Batch absorption test.....	69
4.3.3 Effect of pH.....	72
4.3.4 Adsorption isotherms	73
4.3.5 Effect of contact time and adsorption kinetics.....	75
4.3.6 Effect of temperature and thermodynamic parameters	77
4.3.7 Proposed mechanism	79
4.4 Conclusion	80
CHAPTER FIVE	81
General Discussion, Conclusion and Recommendations.....	81
5.1 General Discussion	81
5.2 Conclusions.....	84
5.3 Recommendations.....	85
REFERENCES.....	87

LIST OF TABLES

Table 1: Compounds of calcium phosphate family	9
Table 2: Lattice parameters of CHS and PCCs refined cells.....	20
Table 3: Comparison of parameters of α - and β -GlcN with XRD values of CHS.	22
Table 4: Geometric parameters of the optimized structures of the GlcN adducts.....	29
Table 5: Fluoride adsorption efficiency (%) and capacity (Q_e) for CHS, CCS and PCCs.	31
Table 6: Selected frequencies (cm^{-1}) F-PCCs and β -GlcN-HF.....	32
Table 7: Mineral content, Ca^{2+} concentration in acid liquors and % yields of CAPs.....	41
Table 8: Chemical composition of CAPs (wt%).....	41
Table 9: Selected XRD peaks analysis data for CAPs.....	43
Table 10: IR frequencies for CAPs and fluoride adsorbed FPHA and FCHA.	46
Table 11: Water quality parameters of field samples.	47
Table 12: Batch adsorption test with different materials.....	48
Table 13: Water quality parameters before and after treatment with CHA.....	50
Table 14: Two parameter adsorption isotherms equations.	53
Table 15: Nonlinear isotherms constants for adsorption of F^- onto CAPs.	54
Table 16: Linear isotherms constants for adsorption of F^- onto CAPs.	55
Table 17: Kinetic models equations.....	56
Table 18: Kinetic parameters of CAPs.	58
Table 19: Thermodynamic parameters of interaction of F^- with CAPS.....	60
Table 20: Chemical composition Cs-HA, F.Cs-HA and CHA (wt%).	66
Table 21: Selected XRD peaks analysis data for Cs-HA.....	67

Table 22: Batch adsorption test with Cs-HA.	70
Table 23: Linear isotherms constants for adsorption of F ⁻ onto Cs-HA.	74
Table 24: Experimental and predicted F ⁻ adsorption q _e on to Cs-HA composite	75
Table 25: Kinetic parameters of F ⁻ adsorption on Cs-HA.	76
Table 26: Thermodynamic parameters of interaction of F ⁻ with Cs-HA.	78
Table 27: Fluoride adsorption capacities on various adsorbent materials.	83

LIST OF FIGURES

Figure 1: Process of isolation of chitosan from crab shells.	6
Figure 2: Geographical location of Tanzania with major water bodies.....	7
Figure 3: Chemical interaction between chitosan and hydroxyapatite	10
Figure 4: XRD patterns CHS (upper curve) and PCCs (lower curve).....	19
Figure 5: Conformers of GlcN: (a) α -conformer (b) β -conformer.....	20
Figure 6: Optimized structures of the three rotamers of β -D-glucosamine.	21
Figure 7: IR spectra of β -GlcN for gas phase (a) solvent phase (b) and FT-IR of CHS (c).	23
Figure 8: Electronic spectra of β -GlcN gas phase (a) solvent phase (b) and UV-Vis of CHS (c).	25
Figure 9: Charge distribution in β -GlcN-H ⁺ and β -GlcN.....	26
Figure 10: Theoretical vibrational spectrum of β -GlcN-H ⁺ for gas.....	27
Figure 11: Comparison of FT-IR spectra of PCCs and CHS.....	28
Figure 12: IR spectrum of β -GlcN-F and structure of GlcN-F (embedded).	30
Figure 13: IR spectrum of β -GlcN-HF and optimized structure of adduct (embedded)...	32
Figure 14: FT-IR spectra of F-PCCs and PCCs.....	33
Figure 15: XRD patterns of CCHA, PHA and CHA.	42
Figure 16: FT-IR spectra of CAPs adsorbents.....	44
Figure 17: FT-IR spectra a) PHA and FPHA b) CHA and FCHA.	45
Figure 18: F ⁻ removal efficiency (%) and adsorption capacities (q_e) of CAPs.....	49
Figure 19: Adsorption of fluoride on CAPs as function of pH.....	51
Figure 20: Non-linear adsorption isotherms of fluoride in different CAPs.	54

Figure 21: Variation of F ⁻ removal with contact time using field water sample (F4).	56
Figure 22: Pseudo-2nd order kinetic plots for fluoride adsorption on CAPs.	57
Figure 23: Variation of F ⁻ adsorption with temperature of the medium.	59
Figure 24: Van't Hoff Plot for CHA.....	60
Figure 25: XRD patterns of Cs-HA, CHA and CHS.	67
Figure 26: FT-IR patterns of Cs-HA, CHA and CHS.....	68
Figure 27: Analysis of FT-IR spectra of Cs-HA and FCs-HA.	69
Figure 28: Efficiency of F ⁻ removal and adsorption capacities by Cs-HA.	71
Figure 29: Water quality parameters before and after treatment with Cs-HA.....	71
Figure 30: Effect of pH on removal of F ⁻ from solution by Cs-HA.	73
Figure 31: Linear regression adsorption isotherms for F ⁻ in on Cs-HA.	74
Figure 32: Effect of contact time of F ⁻ adsorption to Cs-HA.	76
Figure 33: Pseudo-2 nd order kinetic plot for fluoride adsorption on Cs-HA.	77
Figure 34: Variation of F ⁻ removal with temperature of the medium.....	78
Figure 35: Van't Hoff plot for F ⁻ adsorption on Cs-HA.	79

LIST OF ABBREVIATIONS AND SYMBOLS

a.u	Atomic units
BCA	Bone Char
CAPs	calcium phosphate systems
CCHA	Synthetic hydroxyapatite
CHA	Crab shell calcium phosphate
CHS	Chitosan
Cs-HA	Chitosan hydroxyapatite
DFT	Density functional theory
DO	Dissolved oxygen
EARV	East Africa Rift Valley
EC	Electroconductivity
EDTA	Ethylenediaminetetraacetic acid
EDX	Energy dispersive X-rays
FT-IR	Fourier transform infra-red
FWHM	Full width at half maximum
GlcN	Glucosamine
IQ	Intelligence Quotient
LDH	Layered double hydroxides
ORP	Oxidation reduction potential
PCCs	Protonated cross-linked chitosan
PHA	Prawn shell hydroxyapatite
TDDFT	Time dependent density functional theory
TDS	Total dissolved solids
TISAB	Total ionic strength adjustment buffer
UV-VIS	ultra violet –visible
XRD	X-ray diffraction

CHAPTER ONE

General Introduction

1.0 Introduction

This chapter details the general introduction of the study. It focuses mainly on the background information regarding occurrence of fluoride in water systems and techniques that have been used for defluoridation. Materials considered for adsorbent development (chitosan and calcium phosphates) in this study are also introduced in this chapter along with problem statement and objectives of the study.

1.1 Background

Natural contamination of groundwater resulting from its surrounding geological environment is an important factor determining the quality of drinking water, especially where groundwater represents the main water resource. One of the most severe natural contaminants is fluoride (F^-). It has been estimated that more than 260 million people worldwide consume drinking water with fluoride content >1.0 mg/l (Fawell and Bailey, 2006). The World Health Organization guideline threshold for fluoride in drinking water is 1.5 mg/l (WHO, 2011). While sufficient dietary F^- is beneficial for dental strength, excess consumption by humans and animals may cause varying degrees fluorosis. F^- displaces hydroxide ion (OH^-) from hydroxyapatite ($Ca_5(PO_4)_3OH$), the principal mineral constituent of teeth and bones, to form the harder and tougher fluoroapatite ($Ca_5(PO_4)_3F$) which is less soluble than hydroxyapatite. This results in the hardening of the teeth and bones, making them denser and more brittle (Dissanayake, 1991). F^- also has been shown to affect the nervous system of developing fetus at doses that are not toxic to the mother. This neuro-toxicity is manifested as reduced IQ and behavioral disorders after the child is born (Lu *et al.*, 2000). Due to these health and social economic challenges associated high consumption of fluoride, the security of drinking water supply has been identified as one of the sustainable development goals (SDGs): “*Ensure availability and sustainable management of water and sanitation for all.*”

1.2 Fluoride Occurrence

F⁻ occurs naturally in the earth's crust mainly as fluorospar (CaF₂), sellaite (MgF₂), cryolite (Na₃AlF₆) and fluorapatite (Ca₅(PO₄)₃F). These minerals are nearly insoluble in water, thus, F⁻ will be present in groundwater only when environmental conditions favor their dissolution or high F⁻ containing effluents are discharged into the water bodies from industries (Mohapatra *et al.*, 2009).

There are numerous fluoride belts throughout the world where ground waters contain unsafe levels of fluoride (>1.5 mg/l). One of the regions most affected by fluorosis is the East Africa Rift Valley (EARV). Approximately 90% of the population in this belt exhibit varying degrees of fluorosis (Yoder *et al.*, 1998), corresponding to over 80 million people (Smedley *et al.*, 2002). The anomalous high F⁻ concentrations in the region have been linked to the development of hyper-alkaline volcanic rocks in the rift zone, including nepheline and carbonatite magmas and associated ash deposits. These are capable of accumulating large concentrations of F⁻ in melts and volatile fractions. Hence, water bodies in the rift zone can accumulate F⁻ directly as a result of weathering of these rocks, as well as from high-fluoride geothermal solutions. Weathering of the silicate minerals in the lavas and ashes by silicate hydrolysis reactions produces Na-HCO₃-rich groundwater which is depleted of calcium, thus allowing higher F⁻ concentration to occur in solution instead of being precipitated out as fluorospar (Ayenew, 2008).

Due to climate change and persistent drought, groundwater from high fluoride water beds continues to be the main source of water for most communities (Yoder *et al.*, 1998). In Tanzania for instance, F⁻ concentrations of 40-45 mg/l have been reported in groundwater and up to 690 mg/l in lake Momella (Thole, 2013). Due to water shortage problems the government have set the maximum admissible concentrations in drinking waters at 4 mg/l, which is still more than double the recommended 1.5 mg/l. In neighboring Kenya, F⁻ levels of between 30-50 mg/l in groundwater have been witnessed in addition to the record breaking high F⁻ waters of lakes Elementatita and Nakuru; 1640 mg/l and 2800 mg/l, respectively (Chibole, 1987).

In Northern Tanzania, several mitigation measures have been evaluated, investigation of alternative sources of low F^- groundwater by locating aquifers unaffected by fluoride infiltration (Ghiglieri *et al.*, 2010). The hydro-geological data obtained was found difficult to implement due economic and social limitation involved in drilling new wells in low fluoride grounds or improving spring catchment of less polluted waters (Thole, 2013). Water defluoridation has thus been studied as alternative means of providing drinking water in the region.

1.3 Defluoridation Methods

Defluoridation techniques can be classified into three main categories which are: membrane, adsorption and precipitation techniques. Membrane techniques comprise of reverse osmosis, nanofiltration, dialysis and electro-dialysis. Adsorption technique functions on the physical or chemical adsorption of F^- onto the surface of active adsorbent materials. Precipitation methods are based on the use of chemicals (coagulants) to facilitate replacement of less reactive anion (such as OH^-) by F^- and the subsequent precipitation of insoluble fluoride salt (Mohapatra *et al.*, 2009).

1.3.1 Membrane techniques

In reverse osmosis, hydraulic pressure is exerted on one side of the semi-permeable membrane which forces the water across the membrane leaving the salts behind. The relative size of the pollutants left behind depends on the pressure exerted on the membrane. The process produces water of extremely high purity, > 98 % rejection of F^- (Piddennavar and Krishnappa, 2013). Electro-dialysis involves removal of F^- in aqueous form through ion exchange membranes under the driving force of an electric field. The membranes allow the ions to pass but not the water. Nanofiltration uses the same phenomenon as reverse osmosis. The membranes have slightly larger pores than those of reverse osmosis and offer less resistance to passage both of solvent and of solutes. As a consequence, pressures required are much lower, energy requirements are less but removal of solutes is much less exhaustive. Selective removal of F^- is achieved by steric and charge effects.

Fluoride is more strongly hydrated than other monovalent anions due its high charge density and thus is more strongly retained on nanofiltration membranes than competing monovalent anions such as chloride or nitrate (Diawara, 2008). Dialysis separates solutes by transport of the solutes through a membrane rather than using a membrane to retain the solutes while water passes through it as in reverse osmosis and nanofiltration. The membrane pores are much less restrictive than those for nanofiltration, and the solute can be driven through by either the Donnan effect or an applied electric field (Alkan *et al.*, 2008). Though the membrane techniques are highly efficient and selective, they are limited by several factors. They are very sensitive to pH and temperature, are expensive for application in rural areas of developing countries, subject to chemical attacks, plugging, fouling by particulate matter and concentrate large quantity of wastes. Sometimes, pre-treatment requirements are extensive. Electrodialysis is highly energy intensive and most expensive (Kumar and Gopal, 2000).

1.3.2. Adsorption techniques

The working principle of adsorptive filters involves 3 steps, diffusion of F^- from aqueous media to the external surface of the adsorbent, adsorption of the F^- on the surface of adsorbent and lastly desorption of the F^- (Dissanayake, 1991). A variety of adsorbents have been used for the removal of F^- from water. These include activated, impregnated alumina, rare earth oxides, activated clay, impregnated silica, carbonaceous materials, industrial wastes like red mud, spent catalysts and fly ash, zeolites and related ion exchangers, biosorbents, alum, chitosan composites and layered double hydroxides (Mohapatra *et al.*, 2009). The choice of adsorbent material depend on adsorption capacity, pH, contact time, stability of adsorbent, regeneration, loading capacity in presence of other anions and cations and the overall cost for F^- removal. Adsorption techniques takes a key place in defluoridation research and practice because of its general greater accessibility and lower cost. However, few adsorbents have been able to take the concentration of F^- down to or below the 1.0–1.5 mg/l level which is required for drinking water.

1.3.3 Precipitation techniques

Precipitation methods are based on the addition of coagulants and subsequent precipitation of insoluble fluoride salt. Aluminum salts (alum), lime, Polyaluminum chloride, polyaluminum hydroxyl sulphate and brushite ($\text{CaHPO}_4 \cdot 2\text{H}_2\text{O}$) are some commonly used coagulants (Mariappan and Vasudevan, 2002). The best examples for this technique are the famous *Nalgonda* technique of defluoridation- using alum, lime plus bleaching powder and contact precipitation using bone char. These methods have been extensively applied in Kenya and Tanzania for water purification. Though the precipitation methods are found to be simple and low cost for rural water treatment, there are concerns in many areas. The *Nalgonda* technique is highly limited by the large quantities of alum needed for treatment. This results into high aluminum contamination ($> 0.2 \text{ Mg/l}$). Discarding sludge from the process is also an environmental risk since it is toxic and contains the removed F^- (Modi and Soni, 2013). Bone char can easily harbor bacteria and is thus unhygienic. The efficiency of bone char as an adsorbent for F^- is a function of the charring procedure which should be done cautiously. Moreover, the use of bone-char may invite cultural and religious objections (Larsen and Pearce, 2002).

1.4 Materials Under Study

This research work studied chitosan polymer, calcium phosphate systems and composite material of chitosan and hydroxyapatite for defluoridation of field water in Northern Tanzania. A brief description of each material is here by discussed.

1.4.1 Chitosan polymer

Chitosan (glucosamine polymer) is a polycationic naturally occurring bio-degradable, non-toxic, non-allergenic and antibacterial polysaccharide derived from chitin (*N*-acetyl glucosamine polymer). Chitin is abundantly found in the exoskeletons of crustaceans (prawns and crabs) and cell walls of fungi and insects (Chandur *et al.*, 2011). Its isolation from shells requires the removal of proteins and inorganic calcium carbonate by demineralization, together with small amounts of pigments and lipids.

Chitosan is commercially obtained by alkali hydrolysis of chitin (Fig. 1). Unlike most other forms of natural polymers such as cellulose, chitosan is a nitrogen containing compound with high chelating ability. It has extensive applications in the food industry, agriculture, and medicine and water treatment (Younes and Rinaudo, 2015).

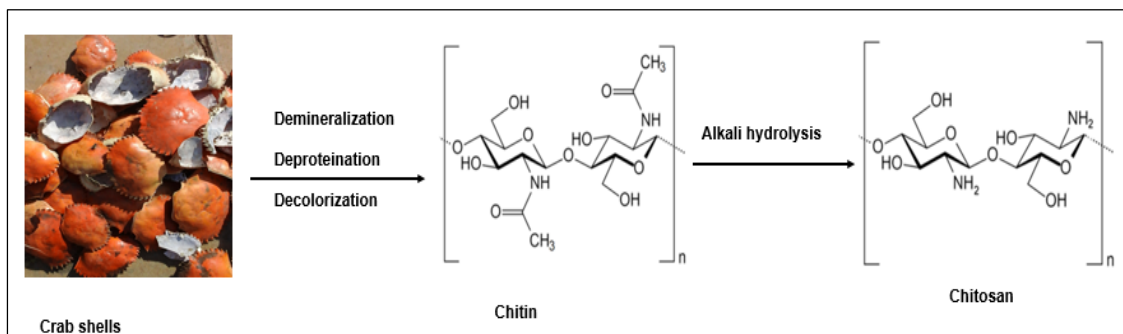


Figure 1: Process of isolation of chitosan from crab shells.

Chitosan is an attractive adsorbent because of its unique properties of biodegradability, biocompatibility and low cost, in addition to its mechanical properties and chelating effects, resulting from the presence of reactive hydroxyl and amino functional groups in polymer chains (Thakre *et al.*, 2010). In the sorption process, chitosan is often used in the form of flakes or powders which are less stable and cause a significant pressure drop which would affect filtration during field applications. The defluoridation capacity of the unmodified chitosan is thus low. If chitosan is suitably modified into a form which could overcome the above mentioned challenges, then it would throw more light on the field of defluoridation (Habuda-Stanić *et al.*, 2014).

For selectivity in the sorption of F⁻, specific functional groups have been introduced into its polymeric matrix of chitosan. Such modifications include magnetic chitosan, composites of silica gel/chitosan, mixed metal oxides/chitosan, electropositive metal/chitosan, hydroxyapatite/chitosan, carboxylated and protonated chitosan beads and titanium/ chitosan microspheres. For chitosan and/or its composite and derivatives to be considered as potential adsorbents for water purification, their availability and sustainability should be indicated (Jagtap *et al.*, 2009; Prabhu *et al.*, 2014; Viswanathan *et al.*, 2014).

1.4.2 Availability of crustacean waste in Tanzania

Tanzania has a great fisheries potential which arises naturally from its geographical location which is bounded to large water bodies. To the North is Lake Victoria which is fresh water lake, Western is Lake Tanganyika, to the south is Lake Nyasa and India Ocean to the East (Fig. 2).

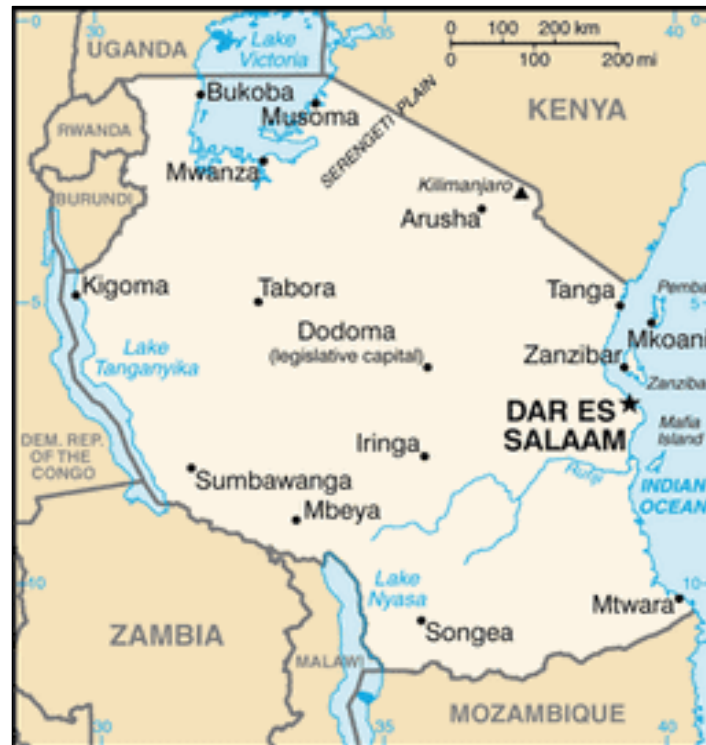


Figure 2: Geographical location of Tanzania with major water bodies.
(<http://www.mapsofworld.com/tanzania/river-map.html>)

Major prawns and crabs harvesting is done in the shallow marine waters of Indian Ocean, in three major areas namely Bagamoyo (-6.4 °N, 38.9 °E), Kisiju (-7.4°S, 39.3 °E) and Rufiji (-8.1°S, 38.4°E). Kisiju area is the most productive contributing up to 45% of the annual catch. Bagamoyo fishing ground contributes 25% and Rufiji area 30% of the prawns annual catches. In all three areas, artisanal fishing accounts for larger catch compared to commercial fisheries (Haule, 2001). According to a report by ministry of livestock and fisheries in 2013, total tonnage of prawns exported in that year was 270 metric tons and 249 tons of live crabs (Rocliffe *et al.*, 2014).

Out of the live weight of the crustaceans, only 20-30% is suitable for human consumption. The rest, viscera and exoskeleton (70-80% on wet basis) are discarded as waste during processing. Major components on dry weight basis are protein (30–40%), chitin (20–30%), minerals (30–50%) and carotenoids (Arbia *et al.*, 2013). Considering the 2013 statistics in Tanzania, volume of waste shells generated from processing of frozen prawns for export, can be estimated as 189 tons (moisture content (65%), totaling to 66 tons on dry basis. With an estimated chitin recovery of 21% there was potential to produce 13.5 tons of chitin from prawn waste only.

The recovery of the waste is however marginal, with only a small volume of available tonnage, being dried, ground and marketed as poultry feed. The rest are dumped into water ways adjacent to processing plant and localities where processing activities are concentrated. Extraction of chitosan within the vicinity the processing plants could reduce the pollution and produce other valuable by-products such as protein which can be used for fortifying animal feeds, calcium carbonate which can be used for soil treatment or precursor for calcium phosphate systems (Anderson *et al.*, 2013) and natural carotenoids, especially astaxanthin which has profound utility value in fish culture as well as in fish products industries (Cahú *et al.*, 2012).

1.4.3 Calcium phosphate systems

Calcium phosphate systems (CAPs) belong to a family bioactive ceramics containing nontoxic ions; Ca^{2+} , PO_4^{3-} , OH^- and water molecules. Their physical properties can range from hard and insoluble to soft, friable and soluble. Control of the properties is by a variety of factors that include setting the calcium to phosphorous ratio, the presence of traces of other biocompatible metal ions, control of density and inclusion of porosity (Radin and Ducheyne, 1993). Calcium phosphate compounds exhibit excellent biocompatibility due to their chemical and crystallographic similarities with the mineral constituents of bones and teeth. They are also promising material for preparation of composites and as a reinforcements (Ioku, 1998). Compounds included in calcium phosphate family are listed in Table 1 (Tung, 1998; Aizawa *et al.*, 2006).

Table 1: Compounds of calcium phosphate family.

Ca/P ratio	Name and abbreviation		Chemical formula	Description
0.5	Monocalcium phosphate monohydrate (MCPM)	phosphate	$\text{Ca}(\text{H}_2\text{PO}_4)_2 \cdot \text{H}_2\text{O}$	Highly soluble and acidic.
0.5	Monocalcium anhydrous (MCP)	phosphate	$\text{Ca}(\text{H}_2\text{PO}_4)_2$	incompatible
1.0	Dicalcium phosphate brushite (DCPD)	dehydrate,	$\text{CaHPO}_4 \cdot 2\text{H}_2\text{O}$	Solubility 0.02 g/100 ml,
1.0	Dicalcium phosphate monetite (DCPA)	anhydrous,	CaHPO_4	Biocompatible, Biodegradable, Osteoconductive.
1.3	Octacalcium phosphate (OCP)		$\text{Ca}_8\text{H}_2(\text{PO}_4)_6 \cdot 5\text{H}_2\text{O}$	
1.5	α -Tricalcium phosphate (α -TCP)		$\text{Ca}_3(\text{PO}_4)_2$	Insoluble
1.5	β -Tricalcium phosphate (β -TCP)		$\text{Ca}_3(\text{PO}_4)_2$	
1.67	Hydroxyapatite (HAP)		$\text{Ca}_{10}(\text{PO}_4)_6(\text{OH})_2$	Insoluble, most stable CAP
2.0	Tetracalcium phosphate (TTCP)		$\text{Ca}_4(\text{PO}_4)_2\text{O}$	Soluble below pH 5, most basic

Bone char, a biogenic HAP is the oldest known adsorbent for F^- . Comparison of defluoridation efficiency of bone char and insoluble calcium phosphates indicated the following trend, TCP (87.0%) > HAP (68.0%) > bone char (66.4%) in batch procedure with water of initial F^- concentration 10.4 mg/l. When little amount of more soluble MCP was added to bone char the removal efficiency increased to 94% (He and Cao, 1996). This gives an indication of influence of Ca/P ratio and solubility on defluoridation efficiency.

1.4.4 Chitosan hydroxyapatite composite

Chitosan hydroxyapatite (Cs-HA) is a biomaterials composed of chitosan polymer matrix and inorganic HAP. The composite formed is biocompatible, biodegradable and exhibits excellent bioactivity in addition to enhanced mechanical properties (Pighinelli and Kucharska, 2013). Chemical interactions between the chitosan and HAP constituents in the composite, probably takes place via chelation between Ca^{2+} and the NH_2 group of chitosan as shown in Fig. 3 (Li *et al.*, 2005; Wang and Li, 2007; Venkatesan and Kim, 2010). The composite have significant application in environmental remediation and biomedical regeneration of bone tissue.

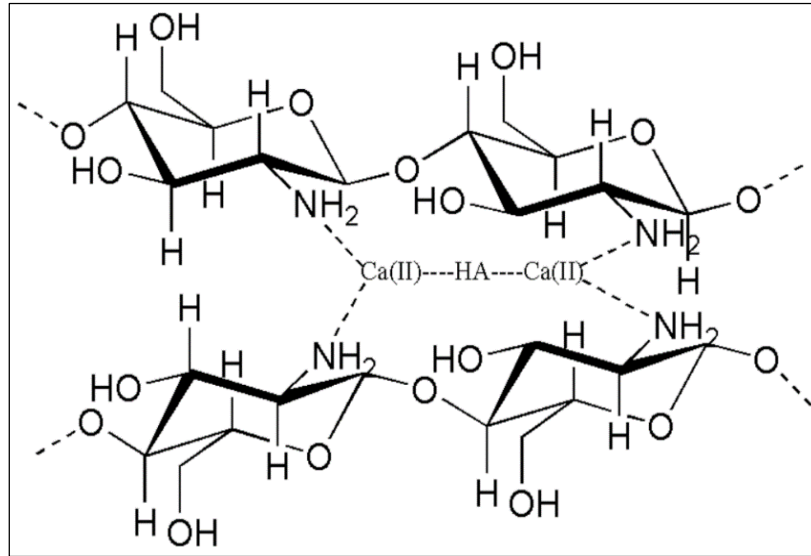


Figure 3: Chemical interaction between chitosan and hydroxyapatite (Venkatesan and Kim, 2010).

1.5 Problem Statement

The EARV is still an active volcanic region, the rocks particularly in the young basalt contain high concentrations of fluorite and fluorapatite. The floor of the Rift Valley which is characterized by high hydrothermal activity accelerates the solubility of these minerals. Due to climate change and persistent drought, ground water from high fluoride water beds continues to be the main source of drinking water for the communities living in this regions. High-fluoride in drinking water represents a health hazard to more than 80 million people in the region. Risks of permanent physical disability due to skeletal and dental fluorosis are high. Until now no reliable and affordable fluoride removal technology exists for the poor communities in this area. Most of the methods currently available for the removal of fluoride from drinking water are complex and/or costly, or not fully tested. In addition, few or no investigations have been undertaken on implications (public health, technology acceptance, environmental and economic impacts) of current fluoride removal technologies that are being applied in local communities. Others have not been piloted or validated in the field setting despite showing good removal efficiencies in the laboratory using simulated water.

1.6 Justification

The development of low cost water defluoridation materials to deal with environmental, socio-economic and health risks associated with drinking contaminated water is crucial for many rural areas in Africa. In the EARV, high levels of fluoride in community drinking water supply are recognized as one of the major public health problems. The utilization of commercially available adsorbents can be exchanged by the inexpensive and effective biogenic adsorbent derived from biomass wastes. Chitosan is attractive because of its unique properties of biodegradability, biocompatibility and low cost, in addition to its mechanical properties and chelating effects, resulting from the presence of chemically reactive groups (hydroxyl and amino functions) in polymer chains giving it a pseudo cationic nature. These properties enable it to efficiently interact with charged surfaces and particles. It is thus envisaged that it could be applicable in treating F^- contaminated water and remove microbes at no extra cost. Calcium phosphates derived from crustacean biomass waste is another very attractive material for water defluoridation, experience derived of effectiveness of bone char in defluoridation of low fluoride water, show that calcium phosphate systems have a potential to be modified to improve capacity and performance in highly fluoride contaminated water.

1.7 Objectives

The general objective of the study was to develop local, efficient and sustainable material for defluoridation of drinking water.

1.7.1 Specific objectives

- (i) To synthesize protonated cross-linked chitosan from crustacean shells and study its interaction with fluoride experimentally and theoretically.
- (ii) To prepare crustacean derived calcium phosphates and test their defluoridation capacity
- (iii) To prepare chitosan-crustacean derived calcium phosphate composite and test its defluoridation capacity.

1.8 Dissertation Framework

This dissertation reports the study of crustacean biomass waste derived adsorbent for purification of fluoride contaminated water in Northern Tanzania, along the EARV belt. Synthesis, characterization of the materials and their fluoride adsorption capacities and efficiencies is discussed. The dissertation is divided into 5 chapters; Chapter one is the introduction, problem statement and objectives. Chapters two, three, and four are manuscripts prepared for submission to various journals for publication. Chapter two gives account of chitosan isolation, modification, experimental and theoretical interaction with fluoride ions. Chapter three describes synthesis of calcium phosphates derived from crabs and prawns shells, their characterization and fluoride adsorption characteristics. Chapter four discusses a composite of chitosan and calcium phosphate as hybrid adsorbent for both fluoride and microbial contaminants in drinking water. Characterization using XRD and FT-IR is also presented for composite study. Chapter five constitutes the general discussion, overall conclusion and recommendations.

CHAPTER TWO

Interaction of Chitosan with Fluoride: Experimental Study and Density Function Theory Modelling¹

Abstract

Interaction of chitosan with F⁻ has been studied using experimental and DFT computational methods. For experimental investigation, chitosan was isolated from prawns shells and characterized using XRD, FT-IR and UV-Vis. It was further modified by cross-linking with glutaraldehyde and protonated with concentrated hydrochloric acid. Adsorption of F⁻ from solution of concentration 10 mg/l was determined using ion selective electrode meter. The β-D-glucosamine (β-GlcN) monomer was used to model chitosan. DFT/B3LYP method with 6-311**G (d,p) basis set was employed for characterization of geometric parameters and harmonic vibrations. The electronic spectrum was calculated by Time Dependent-DFT/B3LYP method. Theoretical computed parameters of β-GlcN are presented and compared with experimental results. The computed IR frequencies in β-GlcN and adducts were used to identify FT-IR bands observed in F⁻ treated protonated cross-linked chitosan (F-PCCs). Results of both computational and experimental studies confirmed that the electropositivity of H atoms of amine and its adjacent OH groups in chitosan influence adsorption of F⁻ by electrostatic attraction and that protonation of the amine group increases F⁻ adsorption capacity and efficiency significantly.

2.1 Introduction

Chitosan is a naturally occurring copolymer of D-glucosamine (GlcN) and N-acetyl-D-glucosamine (GlcNac) linked by β-(1,4)-glycosidic bonds. Commercially, chitosan is obtained by alkali hydrolysis of chitin, which can be extracted from exoskeleton of insects and crustaceans.

¹ Published in Journal of Bio-interface Research in Applied Chemistry, **8** (2018): 3170-3177, ISSN 2069-5837.

Due to its pseudo polycationic properties, in addition to being biodegradable, biocompatible and non-toxic, chitosan has potential applications in fields of environmental remediation of both organic and inorganic contaminants in aqueous solution and soils, biomedicine, food packing and agriculture (Yong *et al.*, 2015). Investigations of interaction of chitosan and its derivatives with charged ions is thus necessary in determination of the mechanism, the efficacy and stability of complexes formed in the environments (Terreux *et al.*, 2006; Miretzky and Cirelli, 2011).

Worldwide, F^- is one of the most important contaminants of drinking water. Though F^- is essential for dental health, when consumed at concentration above 1.5 mg/l it can trigger dental and skeletal fluorosis and increase susceptibility to other health risks such as renal diseases, cancer and neurological damage (Islam and Patel, 2011; WHO, 2011). To mitigate and control occurrence of fluorosis in many regions, defluoridation of drinking water is crucial (Khairnar *et al.*, 2015). Various technologies and adsorbents have been studied and applied in sorption of F^- from water of varying concentrations. Among them, chitosan has received considerable attention as a sustainable biosorbents (Miretzky and Cirelli, 2011). Chitosan application is however, limited due to its poor stability in acidic environments. Hence, it requires to be modified into a stable form before effective use. Cross-linking chitosan with glutaraldehyde or other cross-linking agents have been found to enhance stability in acidic and alkaline environments (Chen and Chen, 2009).

Several experimental studies on the interactions of chitosan and its derivatives with F^- are available in the literature. Chitosan modified by carboxylation of OH groups after cross-linking with glutaraldehyde showed defluoridation capacity 1.4 mg/g which was higher than 0.05 mg/g obtained with unmodified chitosan (Viswanathan *et al.*, 2009b). When the same authors protonated the cross-linked chitosan in concentrated HCl for 30 minutes, F^- adsorption capacity increased to 1.7 mg/g (Viswanathan *et al.*, 2009a). In a similar study, glutaraldehyde cross-linked chitosan membranes that were protonated for 90 minutes in concentrated HCl gave F^- adsorption capacity of 1.3 mg/g (Huang *et al.*, 2012). In all cases the initial F^- concentration of the water was 10 mg/l and batch tests were performed in 50 ml of NaF solution with adsorbent dose of 0.2-0.5 g.

Modification of chitosan by incorporation of electropositive multivalent metals has also been reported. Titanium incorporated chitosan beads gave adsorption capacity of 1.1 mg/g, slightly lower than that for protonated chitosan (Jagtap *et al.*, 2009). Incorporation of rare earth metals such as lanthanum and cerium into the chitosan beads recorded high adsorption capacity in the range 3.7 - 4.7 mg/g (Thakre *et al.*, 2010; Liang *et al.*, 2013). Only few computational studies explain the theory of binding of F⁻ ions to chitosan (Marwa, 2016). Computational analysis is however, seen as an important predictive tool in formulating a guiding protocol for clear understanding and interpretation of various aspects of adsorbent-adsorbate interaction. The present study aimed to investigate the interaction of F⁻ with protonated chitosan using experimental and DFT methods. The most favorable site of attachment of F⁻ to chitosan was determined and structure of the complex formed evaluated. Theoretical IR modes of β -GlcN for gas phase were used to resolve the structural origins of bands observed in FT-IR spectrum of solid state chitosan.

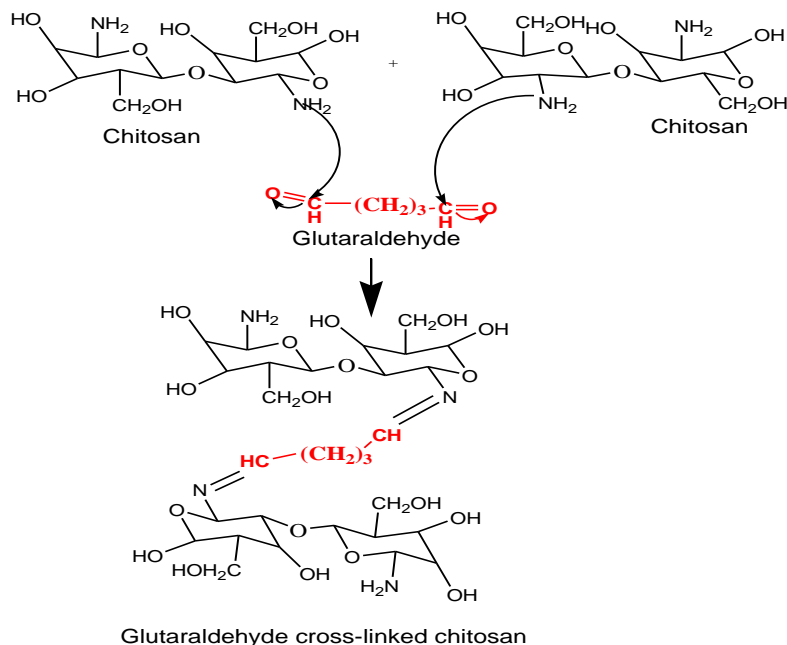
2.2 Materials and Method

2.2.1 Experimental details

(i) Extraction of chitosan from prawns shells

Samples of white prawns (*Fenneropenaeus indicus*) waste shells were collected from Dar es Salaam, Tanzania. Extraction of chitosan followed procedure described in literature (Sagheer *et al.*, 2009; de Queiroz Antonino *et al.*, 2017) with slight modifications. In brief, clean and dry shells were ground into 2 mm sizes and then deproteinated using 0.25 M NaOH at 70 °C for 2 h. The protein free shells were washed with water to neutral pH followed by drying in hot air oven at 50 °C for 12 h. Dry shells were treated with 2 M HCl (solid to acid ratio = 1: 4) at room temperature for 24 h. The residue (chitin) was rinsed to neutral pH, then treated with 1% potassium permanganate (KMnO₄) ratio 1:5 for 2 h, followed by 3% oxalic acid for 3 h to obtain decolorized chitin. De-acetylation of chitin was carried out using 50% NaOH at 70-75 °C for 24 h with constant stirring.

Chitosan obtained was rinsed with de-ionized water to neutral pH and oven dried in hot air for 12 h at 50 °C. Purification was done by precipitation of a solution of chitosan in 1% acetic acid with 0.25 M NaOH, followed by rinsing and freeze drying. Purified chitosan was then cross-linked using 2.5% glutaraldehyde and protonated in concentrated HCl as detailed in (Huang *et al.*, 2012). Proposed reaction mechanism for cross-linking is shown in scheme 1:



Scheme 1: Reaction mechanism for cross-linking chitosan with glutaraldehyde (Hu *et al.*, 2013).

(ii) Characterization of chitosan

Elemental composition of chitosan was determined using Flash 2000 CHNS/O analyzer (Thermo Scientific). X-ray diffraction patterns were evaluated using a Bruker D2 PHASER bench-top diffractometer with monochromatized $\text{CuK}\alpha$ radiation ($\lambda = 0.15406 \text{ nm}$) over 2θ range of $3 - 75^\circ$ at a scanning speed of 3° per minute and a step size of 0.02° . Diffraction data were analyzed using EXPO 2014 software for peak indexing, lattice parameter calculation and refinement by Rietveld technique (Altomare *et al.*, 2013).

Infrared spectra analysis was conducted under vacuum at room temperature using attenuated total reflectance (ATR) with ZnSe crystal as reflection element on a Bruker Tensor 27 Fourier transform infrared (FT-IR) spectrometer in the range of 4000 - 400 cm^{-1} at a resolution of 2 cm^{-1} . Uv-Vis absorbance of chitosan solution, 10 mg dissolved in 25 ml of 0.1 M HCl, was measured using UNICO SQ-2800 single beam Uv/Vis spectrophotometer in the range 190-230 nm.

Degree of deacetylation (DDA) was calculated from CHNS analysis data by relating weight percent of elemental carbon to nitrogen following Eq (1) (Abdou *et al.*, 2008) and further verified by FT-IR spectroscopy using the relation between intensities of reference band at 1420 cm^{-1} and amide band at 1320 cm^{-1} Eq (2), as described in (Brugnerotto *et al.*, 2001).

$$DDA\% = (6.857 - C / N) / 1.714 \quad (1)$$

where: *C/N* is the ratio carbon/ nitrogen as determined by elemental analysis

$$A_{1320} / A_{1420} = 0.3822 + 0.03133 DA \quad (2)$$

where: *A₁₃₂₀/A₁₄₂₀* is the ratio of IR absorption intensity bands at 1320 and 1420 cm^{-1} and *DA* is degree of acetylation and it is equivalent to 100% - DDA .

(iii) Batch adsorption tests

Adsorption experiments were conducted in triplicate using 0.25 g of chitosan adsorbent mixed with 50 ml of fluorinated water sample of concentration 10.4 mg/l. Mixtures were shaken in 250 ml plastic bottles using a Retch AS 200 shaker with amplitude set at 70 for 12 h. Final pH and residue F^- concentration was determined using ion selective electrode. Adsorption capacity was calculated using Eq (3).

$$Q_e = (C_0 - C_e)V / M \quad (3)$$

where *Q_e* is the F^- adsorbed at equilibrium (mg/g), *C₀* is initial F^- concentration (mg/L), *C_e* is F^- concentration at equilibrium (mg/l), *V* is volume of water (L) and *M* is mass of adsorbent (g).

2.2.2 Computational details

Avogadro (1.1.0) program (Hanwell *et al.*, 2012) was used to generate structures and coordinates of GlcN molecule and adducts. Molecular mechanics simulations using Open Babel's force fields (OBForceField MMFF94) provided within Avogadro package was used for conformational search with systematic rotor search function. Lowest energy conformers were selected for DFT study. Firefly quantum chemical package, version 8.1.1 (Granovsky, 2008) partially based on the GAMESS (US) source code (Schmidt *et al.*, 1993) was employed computations. Molecular structures were fully optimized at the B3LYP/ 6-311**G (d,p) level of theory without any symmetry restrictions (Perdew, 1986; Becke, 1993). Stationary points of molecular potential energy surface were characterized using analytical harmonic vibrational analysis for optimized structures using the same level of theory. Absence of imaginary frequencies confirmed that stationary points corresponded to minima on the potential energy surface. For characterization of excited state properties, TD-DFT calculation was employed to obtain the electronic spectra for gas phase and solvent phase using polarizable continuum model (PCM). Visualization of optimized structures, spectra and assignment of vibrational modes was done using ChemCraft graphical program (Zhurko, 2017).

2.3 Results and Discussion

2.3.1 Properties of chitosan (CHS), protonated cross-linked chitosan (PCCs) and glucosamine (GlcN)

(i) Structure analysis

The average recovery of CHS from prawns shells was 16% on dry basis with elemental composition; C 36.25%, H 6.04%, N 6.75%. The DDA obtained from elemental analysis, 86.7% and FT-IR analysis 80.2%, seemed not to differ significantly, the average value of 83.5% was accepted as final DDA of CHS. This value indicated that most acetyl groups were removed from molecular chain of chitin leaving behind chitosan with more free and chemically reactive amino groups. XRD patterns of CHS and PCCs are shown in Fig. 4.

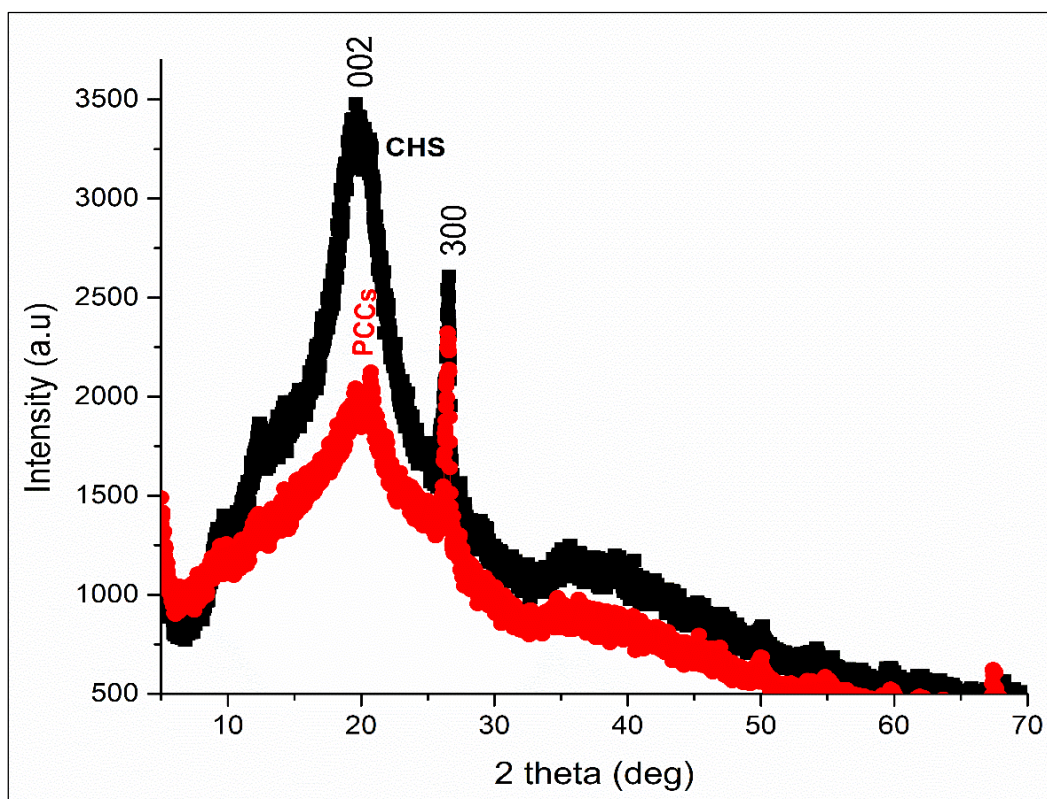


Figure 4: XRD patterns CHS (upper curve) and PCCs (lower curve).

Two peaks were identified, characteristic strong broad peak at $2\theta = 19.6^\circ$ indexed as 002 and sharp medium peak at $2\theta = 26.5^\circ$. The 002 peak was associated with semi-crystalline CHS while 300 peak indicates presence of chitin as suggested in (Sagheer *et al.*, 2009; El Knidri *et al.*, 2016). Presence of two peaks for partially deacetylated shrimps CHS at $2\theta = 20.2^\circ$ and $2\theta = 22.4^\circ$ reported in (Kucukgulmez *et al.*, 2011) compares closely with observed peaks. However, most literature report two characteristic peaks at $2\theta = 10^\circ$ and $2\theta = 20^\circ$ (Yen *et al.*, 2009). For PCCs, 002 peak weakened and became broader while the 300 peaks remained sharp with reduced intensity. The loss in crystallinity of 002 peak can be explained by possible loss of H-bonding upon interaction of glutaraldehyde with amine groups of CHS. This loss of crystallinity in cross-linked chitosan biopolymer has also been reported (Huang *et al.*, 2012; Wang *et al.*, 2015). For both CHS and PCCs, lattice parameters are shown in Table 2. Parameters of CHS corresponds well to those previously obtained for monoclinic structure (Lertworasirikul *et al.*, 2004).

Table 2: Lattice parameters of CHS and PCCs refined cells.

Lattice parameter	CHS	PCCs	CHS (Lit.)*
Crystal family	Monoclinic	Triclinic	Monoclinic
Space group	P21	P-1	P21
A (Å)	9.679	12.134	9.46
B (Å)	9.829	14.365	9.79
C (Å)	10.885	17.994	10.46
Alpha (°)	102.3	66.7	-
Beta (°)	107.5	77.6	105.3
Gamma (°)	92.9	80.9	-
Volume (Å ³)	957.7	1795.8	957.0

*Literature: (Lertworasirikul et al., 2004).

In theoretical analysis, two energetically favored conformers of GlcN, alpha (α) and beta (β) each with ⁴C₁ chair configuration were found through conformational search. The β -conformer had lower energy (-14.44 kJmol⁻¹) than the α -conformer. It is thus considered more stable. The main difference between the structures of α and β conformers is the orientation of OH group attached to carbon C1 and the H atoms attached to N1 atom, (Fig. 5).

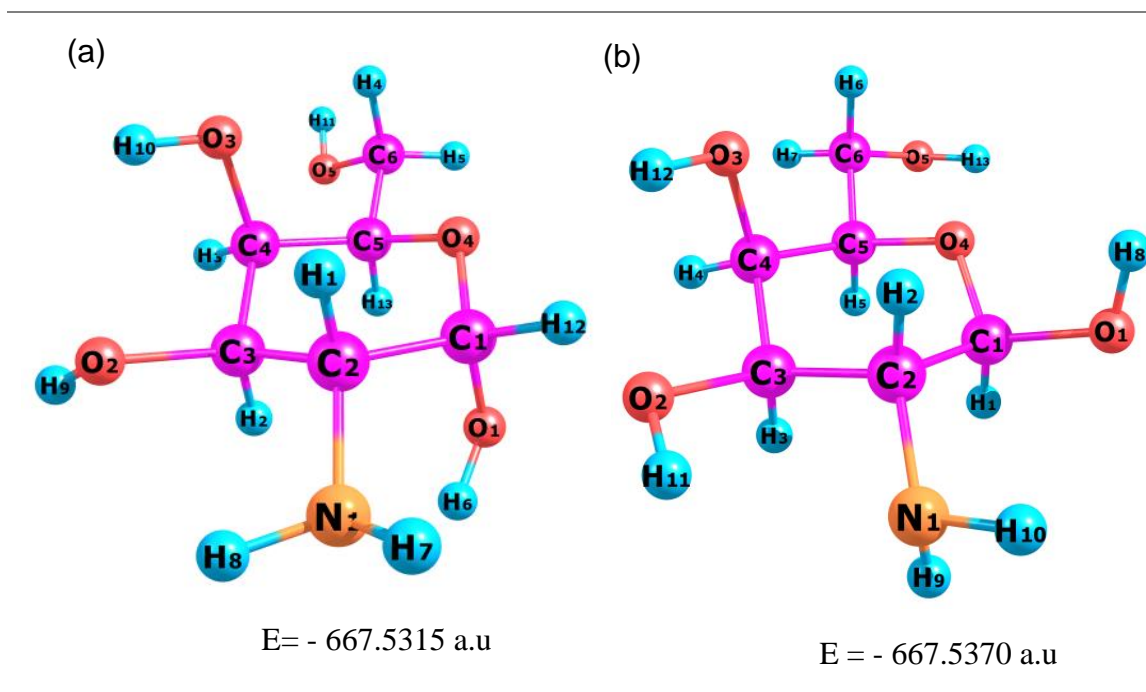


Figure 5: Conformers of GlcN: (a) α -conformer (b) β -conformer.

Upon further analysis of β -GlcN, three stable rotamers were identified; I-Gauche (G^+g^-), II-Gauche (G^-g^-) and III-Trans (Tg^-) (Fig. 6). These rotamers are defined by O5-C6-C5-O4 and H13-O5-C6-C5 dihedral angles in Newman projection as described in literature (Peña *et al.*, 2014). Selected geometrical parameters; bond lengths, valence angles and torsion angles for α and β -GlcN for gas phase are compared with those of β -GlcN for solvent phase (water) computed by PCM model and those obtained by XRD analysis of CHS, are summarized in Table 3. The bond lengths in α and β -GlcN molecules are typical values for C-O, C-C, C-N and O-H, within the range of 1.43, 1.54, 1.47 and 0.96 Å, respectively. The bond angles with C atom in vertex and C-O-H are close to tetrahedral and the pyranose ring is nonplanar. No significant difference was observed in structural parameters between gas phase and solvent phase. Parameters obtained from XRD analysis of CHS are within the same range compared to theoretical parameters. β -rotamer I, was selected for study of interaction with F^- ion and comparison with CHS.

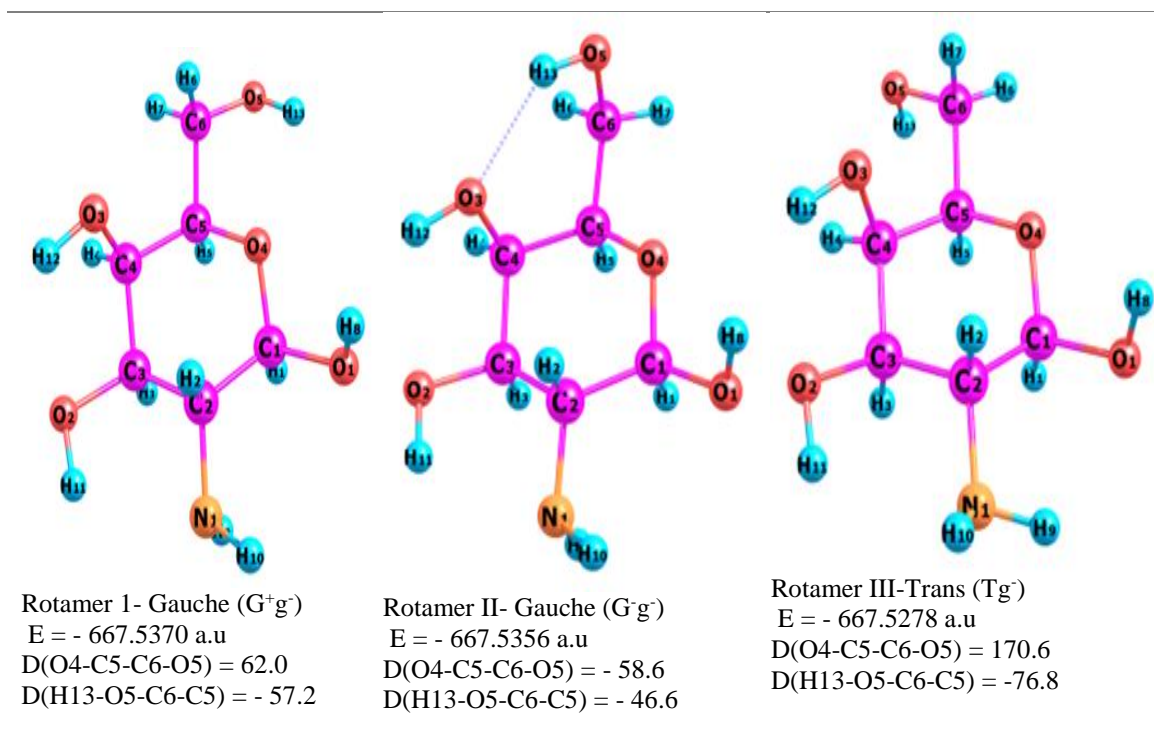


Figure 6: Optimized structures of the three rotamers of β -D-glucosamine.

Table 3: Comparison of parameters of α - and β -GlcN with XRD values of CHS.

	Bond lengths (Å)			
	α -GlcN- gas	β -GlcN - gas	β -GlcN - PCM	XRD CHS solid
R(C1-C2)	1.547	1.540	1.535	1.546
R(C2- N1)	1.470	1.463	1.465	1.537
R(C3-O2)	1.442	1.422	1.436	1.493
R(O2-H9)	0.963	-	-	
R(O2-H11)	-	0.969	0.965	
R(C1-O4)	1.399	1.419	1.424	
R(C1- O1)	1.415	1.398	1.399	
R(O1-H6)	0.971	-	-	
R(O1-H8)	-	0.966	0.968	
R(C4-O3)	1.423	1.420	1.427	
R(O3-H10)	0.965	-	-	
R(O3-H12)	-	0.966	0.968	
Bond angles (°)				
A(C1-C2-N1)	108.5	115.7	109.7	118.2
A(C3-O2-H9)	108.9	-	-	
A(C3-O2-H11)	-	106.0	108.8	
A(C1-O1-H6)	105.5	-	-	
A(C1-O1-H8)	-	107.5	108.4	
A(C4-O3-H10)	107.0	-	-	
A(C4-O3-H12)	-	106.4	106.6	
A(O4-C5-C6)	106.0	107.8	106.5	112.6
A(C1-O4-C5)	113.9	115.0	113.6	
Dihedral angles (°)				
D(C2-C1-O1-H6)	32.1			
D(C2-C1-O1-H8)		-73.6		
D(C2-C3-C4-C5)	53.7	52.3	51.2	50.9
D(O4-C5-C6-O5)	177.2	62.0	62.7	

(ii) Vibrational spectra of β -GlcN and CHS powder

Theoretical vibrational spectra of β -GlcN for gas phase and solvent phase confirmed the optimized structures were in most stable state by absence of imaginary frequency. Comparison with FT-IR spectrum of CHS is given in Fig.7 with vibrational modes assigned. Characteristic bands observed in IR spectra of β -GlcN molecules and CHS powder are as follows: Highest intensity band at 1050-1150 cm^{-1} , was associated with of C-O and C-C bonds. The band at 1650-1670 cm^{-1} was identified as free NH_2 bending, for CHS a twin band at 1590 cm^{-1} was associated with presence of acetylamide group.

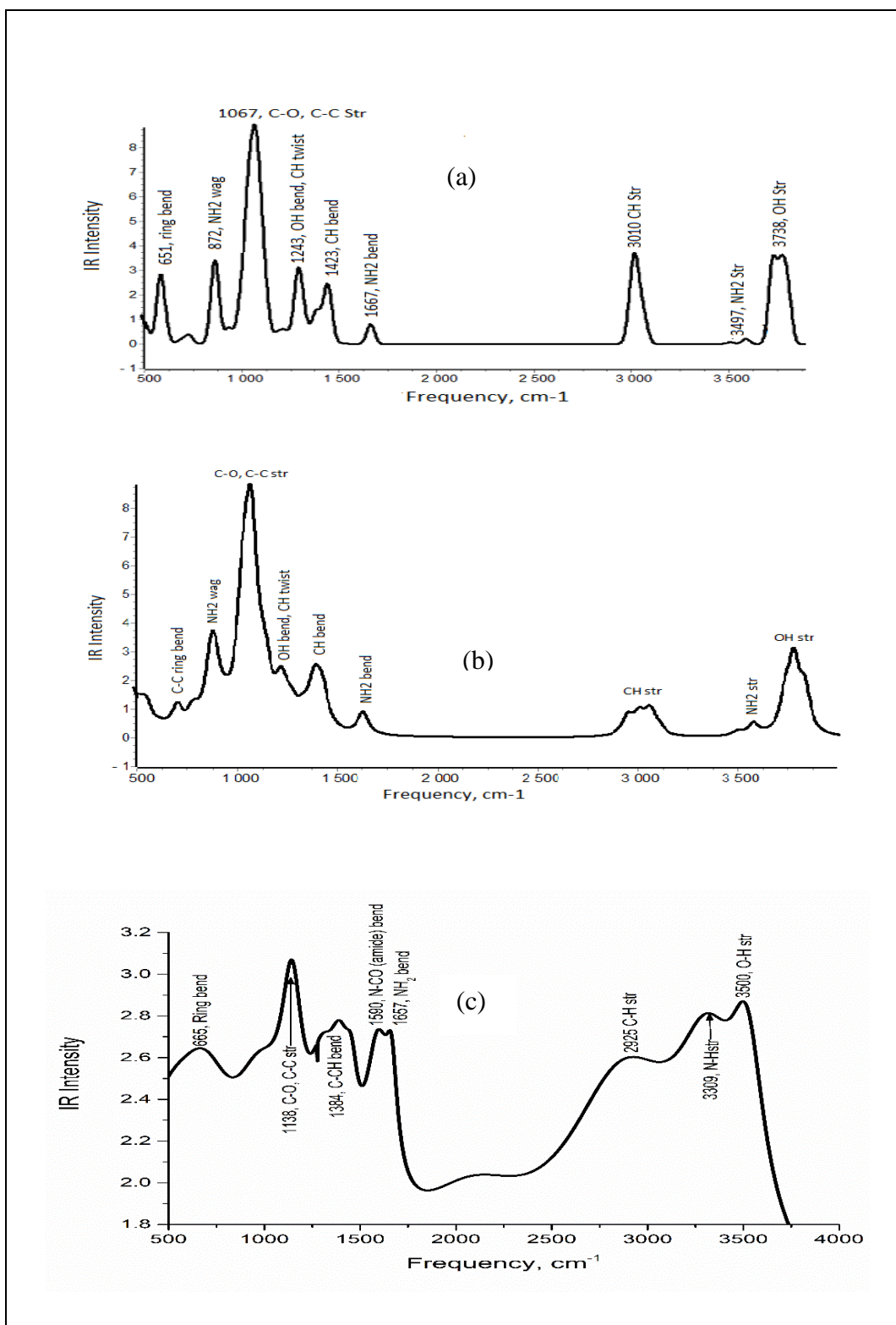


Figure 7: IR spectra of β -GlcN for gas phase (a) solvent phase (b) and FT-IR of CHS (c).

Source of acetylamide group may be explained by the fact that CHS analyzed had DDA as 83.5%, meaning there was still some remnants chitin in the sample. Presence of amide peaks in partially deacetylated CHS has been reported in literature (Prashanth *et al.*, 2002). Characteristic CH stretch peak at 3000-3100 cm^{-1} shifted to lower wavenumbers in FT-IR spectrum of CHS. The NH_2/OH bands at 3200-3700 cm^{-1} in theoretical spectra were also shift to lower wavenumbers (3200-3500 cm^{-1}) in the CHS spectrum. The FT-IR modes for CHS agree better to those of β -GlcN for gas phase than solvent phase.

(iii) Uv-Vis spectra of β -GlcN for gas phase, solvent phase and CHS powder

Uv-Vis spectra of β -GlcN for gas phase, solvent phase and CHS powder are shown in Fig. 8. Spectra of β -GlcN for gas and solvent phase corresponds well to UV-Vis spectra of CHS. The absorption peaks of β -GlcN for solvent phase are however, shifted to shorter wavelength compared to gas phase adsorptions. Two peaks identified for CHS, (206 and 217 nm) are comparable to peaks at 205 and 214 nm in β -GlcN for gas phase but differs slightly from that reported in literature (Liu *et al.*, 2006), which measured absorption maxima at 201 nm for pure chitosan and admixture of GlcNac and GlcN in a solution of 0.1M HCl. In CHS, it was not possible to isolate absorption peaks due to GlcN and GlcNac as the two chromophoric monomers are known to contribute additively to total UV absorbance at particular wavelengths (Liu *et al.*, 2006). From the comparisons of structure and spectrometric characteristic of CHS powder with β -GlcN, it was found that gas phase model parameters agrees well with CHS parameters. Thus, further analysis of GlcN adducts were conducted for gas phase only.

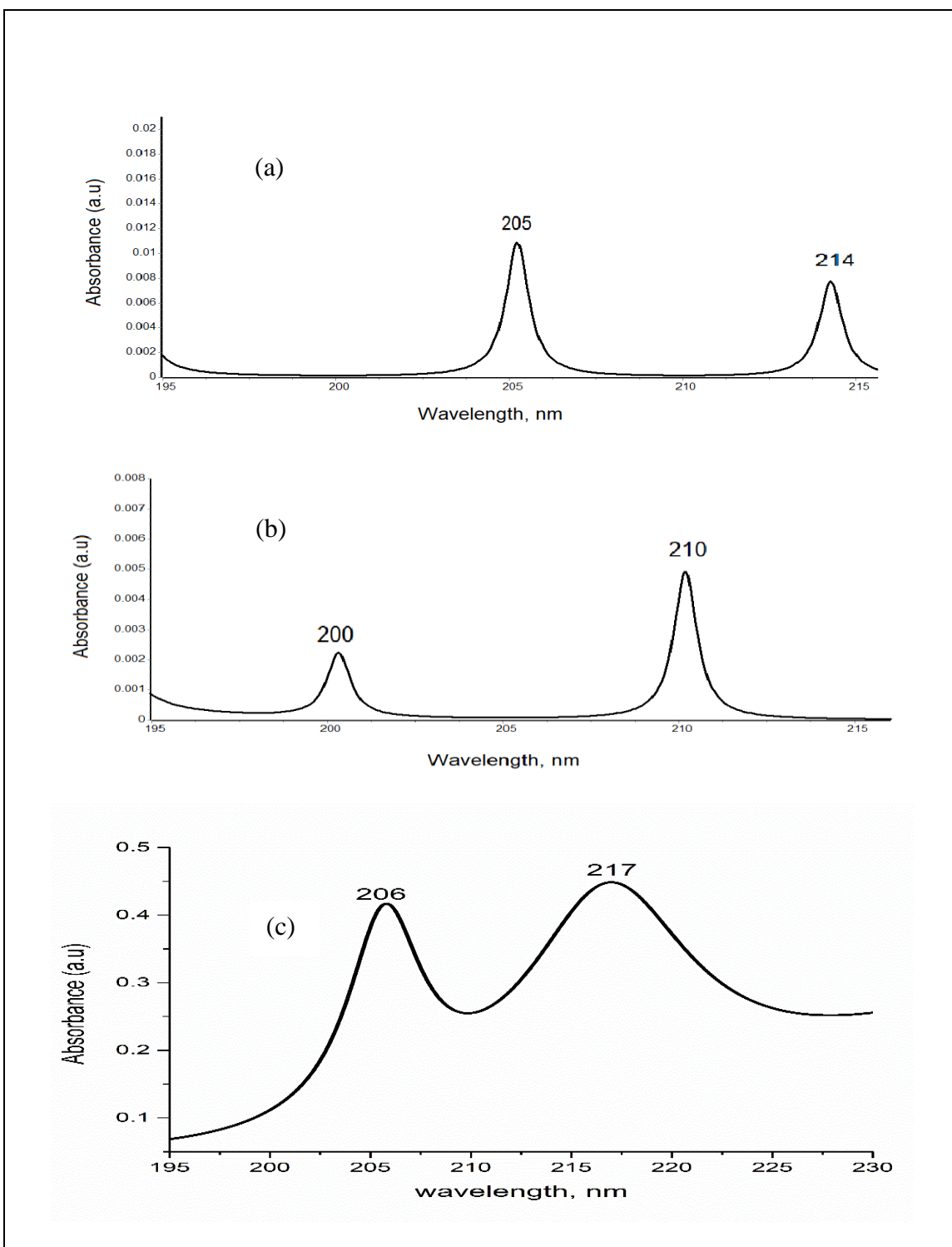


Figure 8: Electronic spectra of β -GlcN gas phase (a) solvent phase (b) and UV-Vis of CHS (c).

2.3.2 Analysis of protonated β -GlcN and PCCs

Geometrical optimized structure, charge distribution, and dipole moment (μ) of protonated glucosamine (β -GlcN- H^+) in comparison with its unprotonated form are shown in Fig. 9.

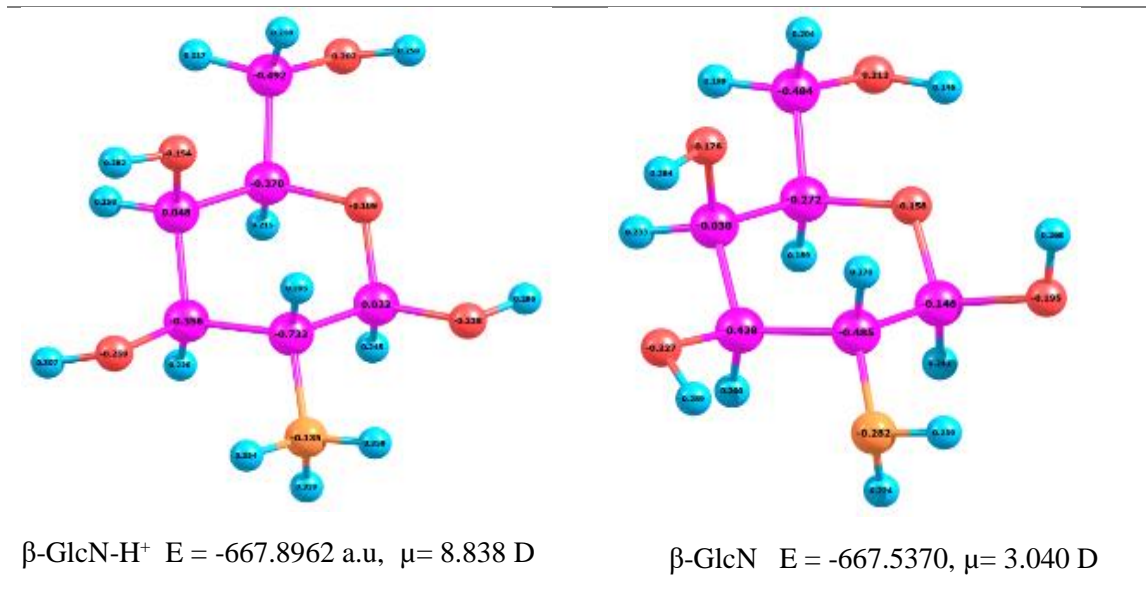


Figure 9: Charge distribution in β -GlcN- H^+ and β -GlcN.

Proton affinity was calculated to be 943 kJ mol^{-1} ($225 \text{ kcal mol}^{-1}$) which coincides with previously reported value (Fattahi *et al.*, 2008). A significant change in μ and charge distribution of atomic sites is observed after protonation. This change relates mostly to atoms and bonds of the amine group and its surroundings. Slight changes in bond lengths and bond angles was observed between β -GlcN (Table 2) and β -GlcN-H shown in Table 4. The C-N bond length increased by 0.05 \AA , ring C-O bond decreased with 0.04 \AA . A significant decrease of 4.7° was seen in C-C-N bond angles while the rest of the angles increased with $1\text{-}4^\circ$. Vibrational spectra of β -GlcN- H^+ for gas phase (Fig. 10) indicate significant changes in the frequency modes as a result of protonation of amine group. The peaks at 651 and 872 cm^{-1} representing ring bending and NH_2 vibration disappeared completely in β -GlcN- H^+ adduct.

Two new peaks at 924 and 1487 cm^{-1} representing vibration of NH_3^+ group were observed, while the intensity of NH_2 band at 3400 - 3500 cm^{-1} increased considerably. All CH vibrations are weaker in $\beta\text{-GlcN-H}^+$ as compared to $\beta\text{-GlcN}$ (Fig. 7a).

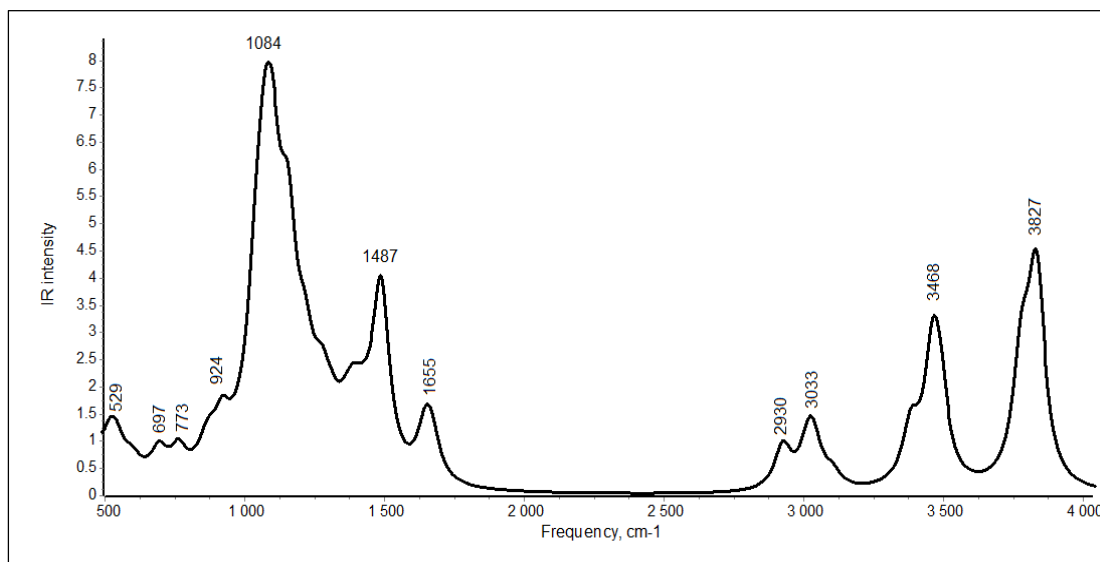


Figure 10: Theoretical vibrational spectrum of $\beta\text{-GlcN-H}^+$ for gas.

The spectral changes in the macromolecule of CHS after cross-linking and protonation to PCCs are shown in Fig. 11. A general decrease in the intensities of all peaks was observed in PCCs. CHS peaks at 640-671 cm^{-1} which are associated with ring C-C bending, disappeared in PCCs, this observation was also made for IR spectrum of $\beta\text{-GlcN-H}^+$ molecule. The NH_2 vibration mode at 3435-3470 cm^{-1} disappeared completely. This explains successful formation of Schiff base between glutaraldehyde and CHS molecule. Preserved modes of amine groups in PCCs are seen at 3380 and 3406 cm^{-1} . The bands at 1165 and 1423 cm^{-1} representing C-O and CH_2 bends, respectively weakened while characteristic NH_2 bending band at 1660 cm^{-1} became broader and stronger. This was associated with presence of C=N bond after crosslinking. New peaks observed at 1507 and 1560 cm^{-1} are attributed to NH_3^+ vibrations. The 1507 cm^{-1} peak corresponds to strong NH_3^+ bending mode at 1487 cm^{-1} observed in the spectrum of $\beta\text{-GlcN-H}^+$.

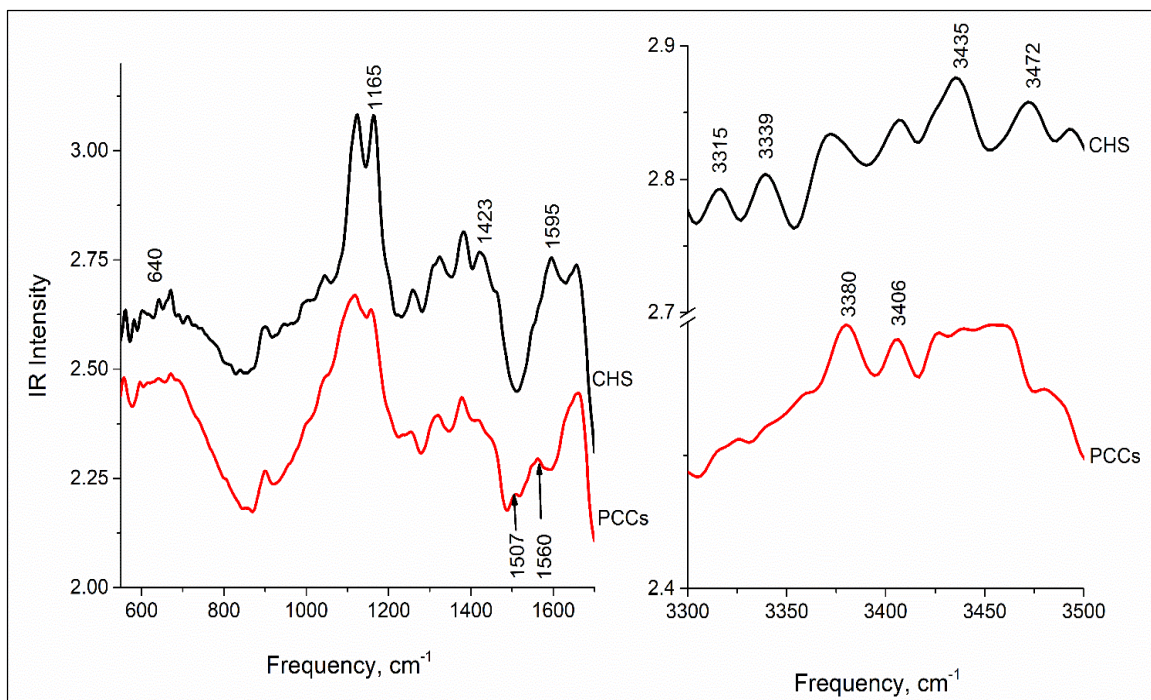


Figure 11: Comparison of FT-IR spectra of PCCs and CHS.

2.3.3 Interaction of F⁻ with chitosan

(i) Fluorinated β -GlcN

Interaction of β -GlcN with F⁻ was modelled through chemical reaction: $\text{GlcN} + \text{F}^- = \text{GlcN-F}$. Fluoride ion was ‘placed’ between NH₂ and OH group attached to C3. The H atom at that position represented the most electropositive site in the molecule (Mulliken charge (q) = 0.289 a.u) as shown in Fig. 9. The optimization, however, directed the F⁻ to the site between H9 of the amino group ($q = 0.259$ a.u) and H8 ($q = 0.268$ a.u) of OH group attached to C1 in the pyranose ring. This position, selected as the most favorable site has the highest combined electropositivity in the molecule from the charge analysis. Optimized structure of fluorinated adduct, β -GlcN-F is shown in Fig. 12 (embedded) and structural parameters are summarized in Table 4. The energy of F⁻ attachment to β -GlcN (ΔrE) was calculated to be $\Delta rE = -206 \text{ kJmol}^{-1}$. A slight change in the geometry of the molecules was observed, longer bond lengths and smaller bond angles compared to β -GlcN.

Theoretical IR spectrum of β -GlcN-F shown in Fig. 12, depicts an intense peak around 2100 cm^{-1} which is associated with vibration of OH----F bond. Another band identified in the adduct, which was absent in β -GlcN is 3275 cm^{-1} frequency, which signify stretching of intermolecular NH----F bond.

Table 4: Geometric parameters of the optimized structures of the GlcN adducts.

Parameter	Bond lengths (Å)		
	β -GlcN-F	β -GlcN-H ⁺	β -GlcN-HF
Adduct			
R(C1-C2)	1.544	1.530	1.535
R(C2- N1)	1.472	1.514	1.482
R(C3-O2)	1.430	1.425	1.417
R(O2-H11)	0.975	0.965	0.973
R(C1-O4)	1.450	1.378	1.409
R(C1- O1)	1.426	1.393	1.398
R(O1-H8)	1.067	0.966	0.964
R(C4-O3)	1.426	1.413	1.417
R(O3-H12)	0.967	0.964	0.967
R(H8.....F1)	1.362	-	
R(H9.....F1)	1.911	-	
R(N1.....H10)	-	-	1.538
R(H10-F1)	-	-	0.996
R(H11.....F1)	-	-	1.833
	Bond angles (°)		
A(C1-C2-N1)	115.8	111.1	111.1
A(C3-O2-H11)	102.5	110.9	111.8
A(C1-O1-H8)	103.9	110.5	108.7
A(C4-O3-H12)	105.2	109.9	106.3
A(O4-C5-C6)	105.6	106.9	106.5
A(C1-O4-C5)	113.4	113.6	112.8
A(O1-C1-O4)	109.0	111.2	108.9
A(O1-H8-F1)	166.9	-	-
A(H20-F1-H21)	83.7		
A(N1...H10 -F1)	-	-	168.9
A(H10-F1.....H11)	-	-	82.3
	Dihedral angles (°)		
D(C2-C1-O1-H8)	-78.9	-175.6	-176.7
D(C2-C3-C4-C5)	50.2	55.3	48.7
D(O4-C5-C6-O5)	55.2	67.8	62.6
D(O1-H8_F26_H21)	-26.8	-	-
D(C2-N1...H10-F1)	-	-	38.8
D(N1....H10-F1.....H11)	-	-	73.6

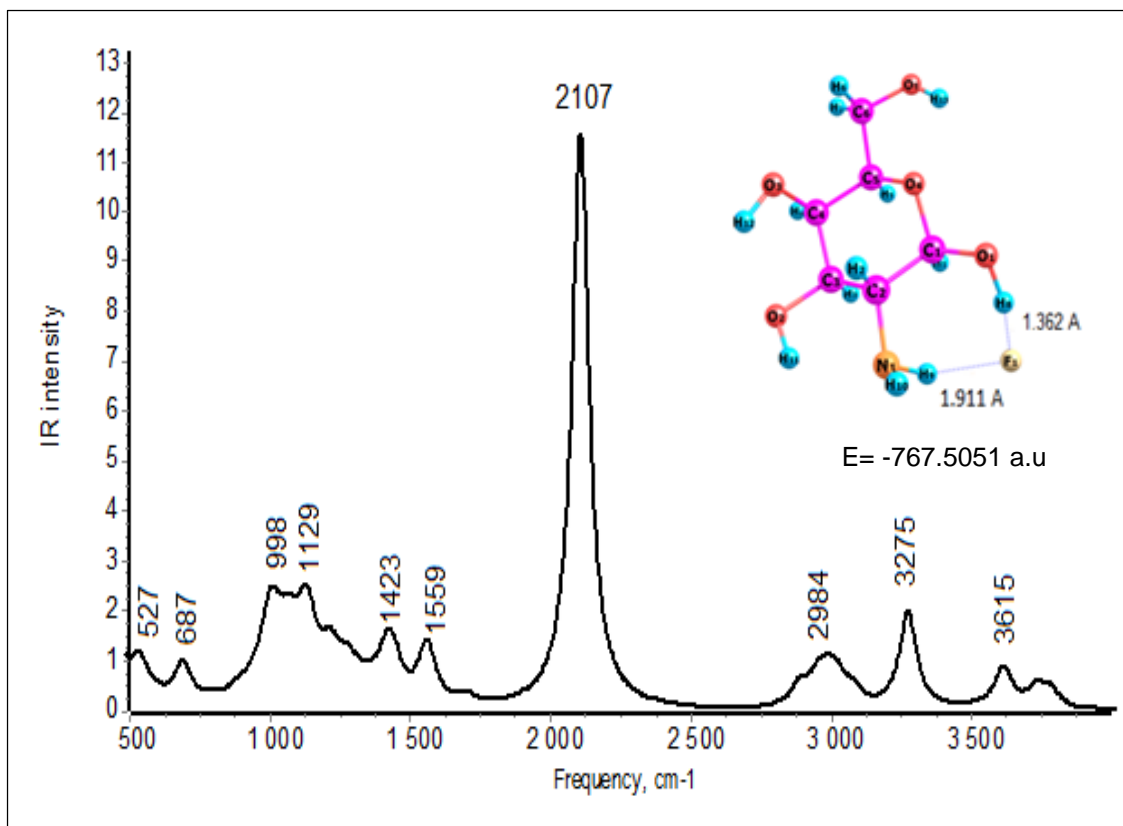


Figure 12: IR spectrum of β -GlcN-F and structure of GlcN-F (embedded).

(ii) Fluorinated GlcN-H⁺ and PCCs

Results of F^- adsorption from water using CHS in pristine and modified form are shown in Table 5. Adsorption with CHS powder and cross-linked chitosan (CCs) gave efficiencies below 20% with very low adsorption capacities (0.2-0.4 mg/g), meaning that materials in this form are not useful in treating water with F^- concentrations above 2 mg/L. PCCs on the other hand recorded a significantly high efficient F^- removal of 77% and adsorption capacity of 1.6 mg/g. These observations are supported from literature that have shown protonated and cross-linked chitosan have higher capacities than uprotonated forms (Viswanathan *et al.*, 2009a). From the data obtained here and from literature it can be concluded that PCCs may only be able to treat water with F^- concentration $\leq 5 \text{ mg/l}$ to achieve WHO recommended threshold of 1.5 mg/l.

Table 5: Fluoride adsorption efficiency (%) and capacity (Qe) for CHS, CCS and PCCs.

Adsorbent	Final pH	C _e (mg/L)	% F-adsorbed	Q _e ,(mg/g)
Cs	6.17	9.20	11.50	0.25
CCs	6.25	8.40	19.20	0.40
PCCs	6.00	2.40	77.00	1.60

Initial F⁻ (C₀) in water = 10.4 mg/L and initial pH of water = 7.2.

In theoretical model, the most favorable site for attachment of F⁻ to β-GlcN-H⁺ was identified as N-H10 and O-H11 attached to C3 of the pyranose ring. The H⁺ formed a sigma bond with F⁻, forming HF which is attached to glucosamine molecule via OH----F and FH---N hydrogen bonding (Fig. 13-embedded). Again, the position of attachment has the highest combined electropositivity in the molecule. Optimized structural parameters are summarized in Table 4. The energy of attaching F⁻ to β-GlcN-H⁺ was calculated as ΔrE= - 676 kJ mol⁻¹, which is about 3 times lower in magnitude compared to attaching F⁻ to unprotonated β-GlcN. This means that it is much easier to bind F⁻ ion to β-GlcN-H⁺. This observation is well supported by experimental data (Table 5), which show that PCCs adsorbs 4 times more F⁻ from aqueous solution than CCs. Theoretical IR spectrum of β-GlcN-HF (Fig. 13) show a blue shift (to longer wavenumbers) in the bands related to presence F⁻ in the molecules compared to unprotonated adduct. The N----HF band is observed at 2602 cm⁻¹ while OH----F stretching band appeared at 3660 cm⁻¹.

Experimental FT-IR spectra of PCCs and fluorinated adduct, F-PCCs are shown in Fig. 14. A general decrease in IR intensity was observed in F-PCCs. Frequency band 508 cm⁻¹ shifted to longer wavelength (501 cm⁻¹) followed by decrease in intensity. Band at 526 cm⁻¹ also shifted to longer wavelength (523 cm⁻¹), but is accompanied by increase in intensity. New peak in F-PCCs at 577 is identified as bending of OH---F bond. This mode was observed at 572 cm⁻¹ in theoretical IR spectrum of β-GlcN-HF (Fig. 13). Vibration mode at 2600 cm⁻¹ representing NH----F vibration mode was not observed in F-PCCs. However, in the 3300-3500 cm⁻¹ region, which is characteristic of NH₂ stretching modes, two observations can be made; the preserved peaks in PCCs at 3380 and 3406 cm⁻¹ disappeared completely and new bands between 3338 and 3444 cm⁻¹ appeared to form a broad band.

This was associated with probable formation of H-bonding between NH_3^+ and F^- . Similar observations have been reported in (Viswanathan *et al.*, 2009a). Details of main IR modes for F-PCCS are given in Table 6 in comparison with theoretical IR modes for β -GlcN-HF.

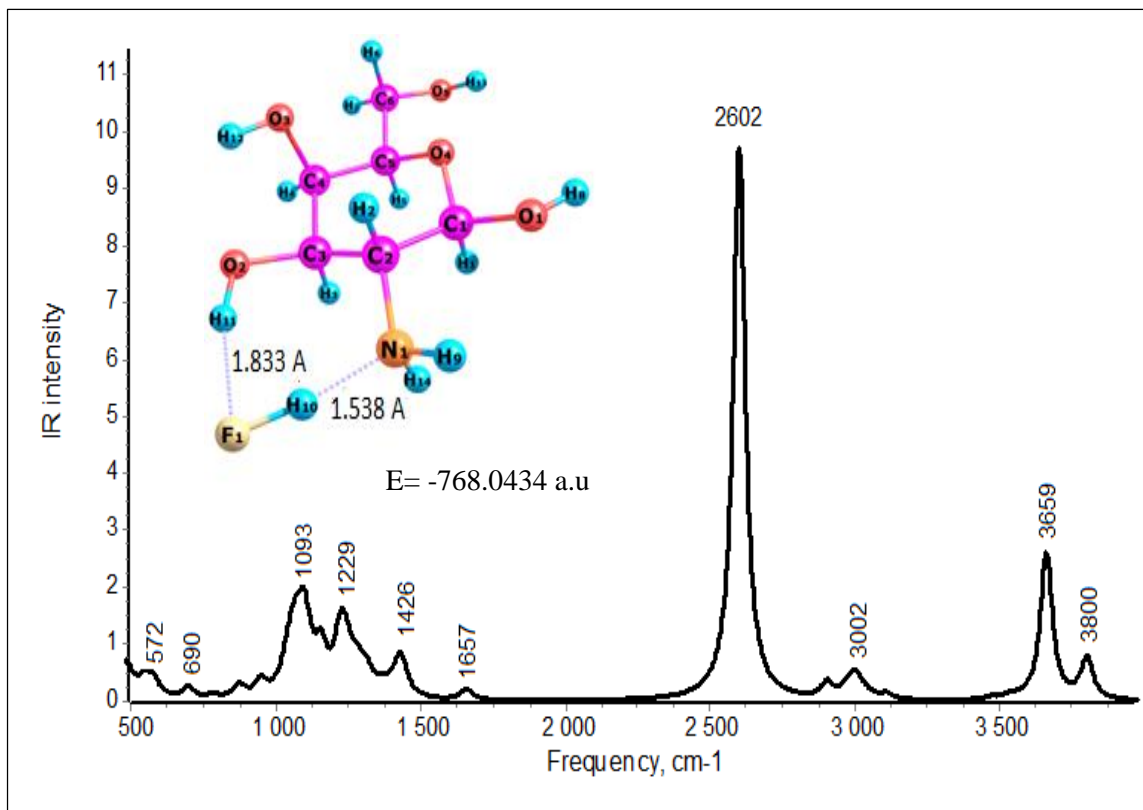


Figure 13: IR spectrum of β -GlcN-HF and optimized structure of adduct (embedded).

Table 6: Selected frequencies (cm^{-1}) F-PCCs and β -GlcN-HF.

F-PCCS	β -GlcN-HF	Vibration modes
577	572	OH...F bending
693	690	OH bending, C-C str
898	879	C-C stretch
1123	1126	H_2N -----HF bending
1156	1154	C- O-C, C-OH str.
1256	1243	CH str
1315	1318	- CH_2 bending
1659	1657	N- H_2 bending
-	2602	N-----HF stretching
2941	3002	C-H stretching
3424	3471	N-H stretching

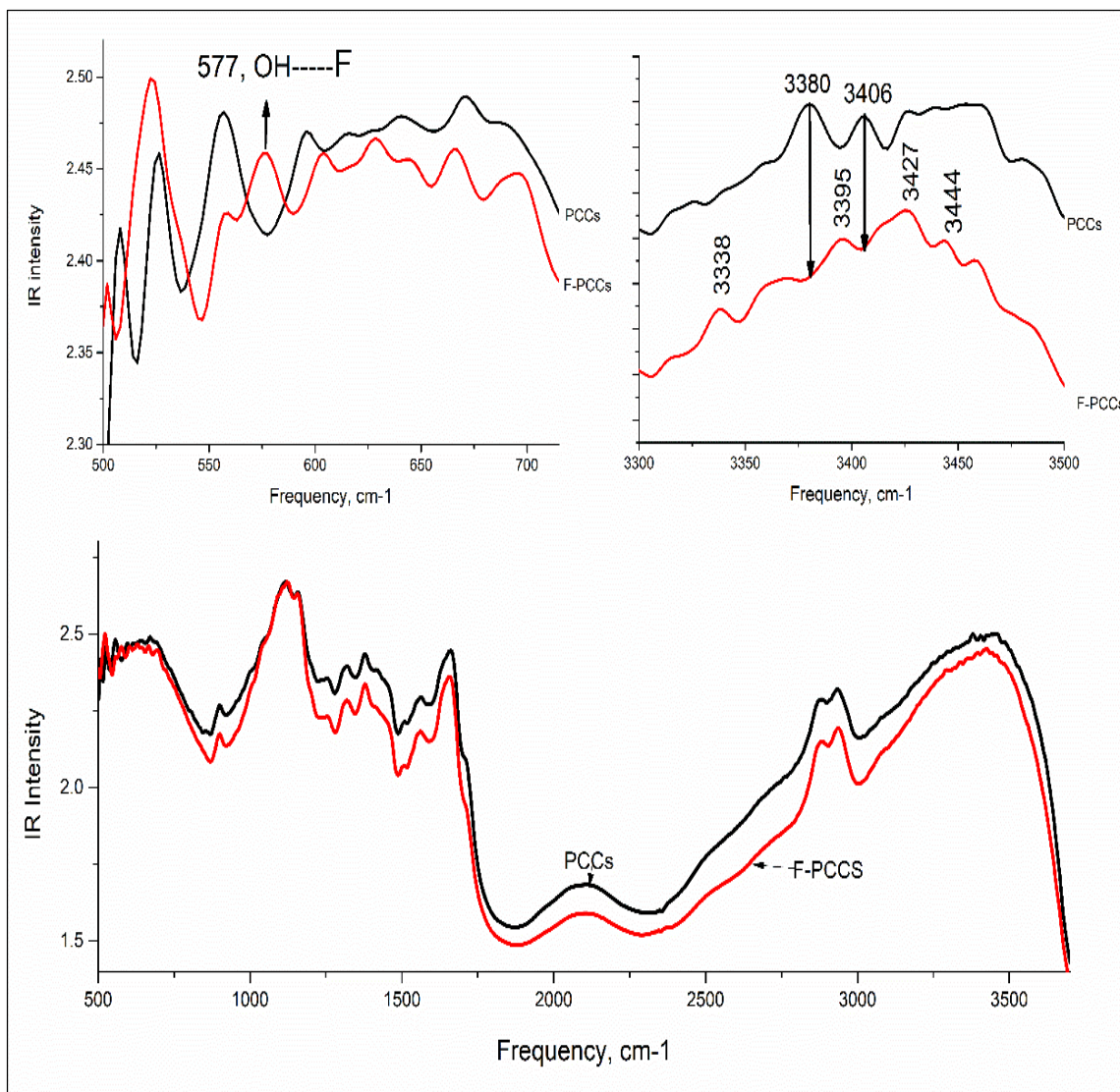


Figure 14: FT-IR spectra of F-PCCs and PCCs.

2.4 Conclusion

Chitosan molecule in crystalline phase may exist as α - or β -copolymer of D -GlcN. According to our DFT calculations, the β -form has lower energy in the potential energy surface and is thus considered to be more stable. Theoretically calculated geometrical parameters, vibrational frequencies and electronic absorption spectrum of β - D -GlcN molecule were found to correspond well with those observed in the XRD structure, FT-IR modes and UV-Vis spectrum of CHS, respectively.

When it comes to chitosan interaction with F^- , PCCs was found to possess higher F^- adsorption capacity than CHS and CCs. Analysis by DFT also confirmed that protonated β -GlcN had better ability of binding F^- than its unprotonated form. The electropositivity of H atoms attached to OH and NH_2 functional groups and the dipole moment of the molecule highly influenced the efficiency of F^- binding. FT-IR analysis of F^- treated PCCs showed presence of hydrogen bonds $OH\cdots F$ in lower frequency region and $H_2N\cdots HF$ bands in higher frequency region ($3330\text{-}3450\text{ cm}^{-1}$). Similar bands were also seen in theoretical IR spectrum of β -GlcN-HF adduct. Experimental and theoretical results in this work show that protonation of the amine groups of chitosan is highly effective in improving its capacity to decontaminate F^- polluted water. The results demonstrate that NH_2 and OH groups of chitosan work together for effective binding of F^- from solution.

CHAPTER THREE

Crustacean Derived Calcium Phosphate Systems: Application in Defluoridation²

Abstract

Calcium phosphate adsorbents, derived from prawns and crabs shell biomass wastes have been developed using wet chemistry and low temperature treatment. The adsorbents were characterized by X-ray diffractometry and Fourier transform infrared spectroscopy. Batch adsorption tests were carried out to investigate their effectiveness in adsorption of fluoride from ground and surface waters. Adsorption capacities were compared with bone char and synthetic hydroxyapatite (CCHA). Results indicate that prawns derived adsorbent (PHA) formed hexagonal structure with phases identifiable with hydroxyapatite while crabs based adsorbent (CHA) formed predominantly monoclinic structure with crystalline phase characteristic of brushite. Vibrational analysis and kinetic studies predicted defluoridation occurred mainly by ion exchange and ion adsorption mechanisms. Defluoridation capacity of the adsorbents was found to be superior compared to bone char and CCHA. CHA was the most effective with efficiencies above 92% and highest capacity of 13.6 mg/g in field water with fluoride concentration of 5-70 mg/l. PHA had highest capacity of 8.5 mg/g which was still better than 2.6 mg/g recorded by CCHA and bone char. Adsorption was best described by pseudo 2nd order kinetics. The findings indicate that crustacean derived calcium phosphate systems have better potential for defluoridation than traditional bone char and synthetic systems.

3.1 Introduction

Bone char is the oldest known calcium phosphate based adsorbent for water defluoridation, applicable in large scale and household units' levels. The technology was first reported as successful in Europe (Roche, 1968). Latter it gained momentum through advocacy for modified bone char by WHO (Phantumvanit *et al.*, 1988).

² Published in Journal of Hazardous Materials. 347, (2017): 95-105, [10.1016/j.jhazmat.2017.12.049](https://doi.org/10.1016/j.jhazmat.2017.12.049)

Currently, bone char technology is successful in Tanzania and other places like Kenya and Ethiopia. However, it has a number of limitations; the cost of processing the bone at high temperatures is high, efficiency of F⁻ removal is low, requiring enrichment with calcium and phosphate components (Albertus *et al.*, 2000) and issues with social acceptability in the communities (Dahi, 2016). These limitations have steered proposals to replace bone char with synthetic calcium phosphate system (CAPs) (Meta, 2014).

Relatively insoluble CAPs such as HAP, DCPD and TCP (Table 1) are most studied for F⁻ removal in literature. Gao *et al.* (2009) studied nanohydroxyapatite (nHAP) of different sizes fabricated by thermal decomposition of calcium nitrate tetrahydrate Ca(NO₃)₂·4H₂O and ammonium dihydrogen phosphate (NH₄H₂PO₄) precursors. Bulk HAPs were obtained by conventional solid-state reaction. Comparisons of F⁻ removal efficiency indicated that smaller sized particle were more efficient, due to higher surface area and adsorption sites concentration with size reduction (Gao *et al.*, 2009). He *et al.* (2016) prepared novel ultralong HAP nanowires by solvothermal method. Oleic acid was used as template dissolved in ethanol, while calcium chloride (CaCl₂) and sodium dihydrogen phosphate (NaH₂PO₄) were the precursors. F⁻ adsorption tested on batch mode showed maximum adsorption capacity of 40.65 mg/g at pH 7.0 when the initial fluoride concentration was 200 mg/l (He *et al.*, 2016).

Poinerna *et al.* (2011) studied performance of nHAP prepared by ultrasonic precipitation and microwave irradiation. Dihydrogen potassium phosphate (KH₂PO₄) and Ca(NO₃)₂·4H₂O, were used as precursors. Maximum monolayer adsorption capacity of 5.5 mg/g was obtained at 25 °C (Poinern *et al.*, 2011). Sundaram *et al.* (2008) synthesized n-HAPs by precipitation method with calcium hydroxide (Ca(OH)₂) and orthophosphoric acid (H₃PO₄) as the precursor at pH 7.5. Maximum defluoridation capacity of 1.8 mg /g was obtained from batch adsorption tests (Sundaram *et al.*, 2008a).

Zhang *et al.* (2012), utilized waste phosphogypsum (PG) as precursor as calcium source and prepared nHAP via microwave irradiation technology. PG was demineralized using 10% HCl to isolate Ca^{2+} ions, filtrate obtained was reacted with 26% $(\text{NH}_4)_2\text{HPO}_4$ solution at pH 11. The precipitate obtained was then transferred to microwave reactor, maintained at 60 °C for 4 h, then filtered, dried and calcined at 500 °C for 2 h to get nHAp particles for F⁻ removal. The maximum adsorption capacity calculated from Langmuir - Freundlich model was 19.7 mg/g at 298 K (Zhang *et al.*, 2012).

Mourabet *et al.* (2011, 2017) synthesized brushite by double decomposition of $\text{Ca}(\text{NO}_3)_2 \cdot 4\text{H}_2\text{O}$ and $\text{NH}_4\text{H}_2\text{PO}_4$ at room temperature. F⁻ adsorption tests, performed in batch mode obtained a maximum monolayer capacity of 6.59 mg/g at 310 K. Further study to optimize the absorption capacity were performed using Box-Behnken response surface design. Results revealed that most desirable conditions were; adsorbent dose (0.15 g), initial F⁻ concentration (49.1 mg/l), T (305 K) and pH (5.4) which gave adsorption capacity of 32.2 mg/g (Mourabet *et al.*, 2011; Mourabet *et al.*, 2017). Larsen and Pearce (2002) studied analytical grades brushite (Fluka) mixed with equal weights of calcite (Merck) in water containing 5, 10 and 20 mg/l fluoride with boiling for 30 seconds. Results showed that 0.3 - 0.5 g of brushite and equal weights of calcite reduced F⁻ concentration to 0.06, 0.4 and 5.9 mg/l, respectively (Larsen and Pearce, 2002). He and Cao (1996) studied static defluoridation of water using different combinations of relatively insoluble CAPs: TCP, bone char and HAP. Treatment of 100 ml of water with initial F⁻ concentration of 10 -12 mg/l by 0.3 g each phosphates gave efficiencies in the range of 60 - 70%. When more soluble MCP was added, the efficiencies improved by 30% (He and Cao, 1996).

From the promising F⁻ adsorption capacities, and advanced knowledge of preparation of synthetic CAPs with nanosized structures as seen in the literatures, it can be recognized that CAPs, are potential solution to the fluoride problem in endemic areas. For sustainability and availability, renewable sources of CAPs or their precursors need to be explored. Apart from mammalian bones, calcium precursor can be extracted from inexpensive natural sources such as egg shells, crustacean shells, corals and plants (Akram *et al.*, 2014).

Crustacean shells are of particular interest because of the abundance in production from sea food industry as process waste and environmental benefits associated with recycling them and expanding their utilization horizon. It is estimated that 6 - 8 million tons of crabs, prawns and lobster shells are produced annually in the world and most of it is left to rot in the sea or is dumped in landfill (Yan and Chen, 2015). This work reports a new approach to utilize the crustacean shell waste. Synthesis and characterization of calcium phosphate adsorbents derived prawns and crabs waste shells is discussed. Defluoridation capacity was investigated to evaluate potential application of materials in treatment of drinking water contaminated with fluoride.

3.2 Materials and Methods

3.2.1 Raw materials

Chemical reagents used in the study were of analytical grade from sigma Aldrich. Samples of white prawns and swimming crabs shell were used. Moisture content of clean and dry shells was determined by oven drying method and ash content using National Renewable Energy Laboratory (NREL) standard procedure LAP-005 (Sluiter *et al.*, 2004).

3.2.2 Preparation of CAPs

Dry and deproteinated prawns shells were treated with 2 M HCl (solid to acid ratio = 1: 4) at room temperature for 24 h while stirring. Crab shells were treated in same way but with solid to acid ratio of 1:8. Filtrate obtained in both cases was titrated with 0.1 M EDTA and calcon carboxylic acid indicator (C₂₁H₁₄N₂O₇S.2H₂O) to determine the concentration of Ca²⁺ in the liquor. For the purpose of comparison, filtrates were also precipitated using 0.5M Na₂CO₃ solution. All the CAPs were synthesized following Eq. 4 and procedure described in in literature (Chen *et al.*, 2002), without the calcination step.



For synthetic hydroxyapatite (CCHA), 250 ml of 1.09 M $\text{Ca}(\text{NO}_3)_2 \cdot 4\text{H}_2\text{O}$ and equal volume 0.653 M $(\text{NH}_4)_2\text{HPO}_4$ solutions were mixed slowly in a 1000 ml beaker under vigorous stirring. The pH of mixture was adjusted to 10.4 using 28% ammonium solution and stirring continued at 40 °C for 4 h. The mixture was then left to age at room temperature for 24 h while still stirring. The precipitate formed was filtered and rinsed with distilled water to neutral pH followed by a methanol rinse. The sample was dried in hot air oven at 80 °C for 24 h and ground into powder. Crustacean derived CAPs were synthesized using same general procedure described above. For crab shell calcium system (CHA), 300 ml CaCl_2 liquor (crab shell acid extract) with Ca^{2+} concentration of 43.69 g/l (1.09 M) was reacted with 300 ml of 0.653 M $(\text{NH}_4)_2\text{HPO}_4$. Prawns shell system (PHA) was synthesized using 300 ml CaCl_2 liquor from prawns shell with Ca^{2+} concentration of 27.65 g/l (0.69 M) and 300 ml of 0.416 M $(\text{NH}_4)_2\text{HPO}_4$.

3.2.3 Material characterization

Chemical composition of CAPs was evaluated using energy dispersive X-ray (EDX) spectroscopy (Shimadzu EDX-800HS). XRD and FT-IR analysis were carried out as described in chapter 2, section 2.2.1 (b).

3.2.4 Batch adsorption tests

Simulated water was prepared by dissolving 2.21 g of NaF in one liter of distilled water to make stock solution with 1000 mg/l. Serial dilution was done to obtain different concentrations of F^- in the solution. Field water samples were collected in *Ngarenyanyuki* ward (S03°10.931'E036°51.677'), Northern Tanzania. Physical parameters Electroconductivity (EC), Dissolved oxygen (DO), Oxidation reduction potential (ORP), Total dissolved solids (TDS) and temperature were measured using Hanna HI 9829 Multiparameter. F^- concentration was determined using ion selective electrode (ISE) connected to a Mettler Toledo seven compact pH/Ion S220 meter. The fluorinated water was mixed with total ionic strength adjustment buffer (TISAB) ratio of 1:1 to determine F^- concentration. TISAB solution concentration was as follows: 57.0 ml glacial acetic acid, 58.0 g NaCl, 4 g cyclohexanediaminetetraacetic acid (CDTA) and approximately 150 ml of 6 M NaOH, added to adjust pH to 5.3- 5.5 in a volume of 1L.

Values of pH were recorded using Orion Star A211 pH benchtop Meter. Microbes were determined by plate count on agar media incubated at 44.5 °C for 24 h. Levels of phosphate and color were determined using HACH DR/2800 spectrophotometer. Batch adsorption experiments were conducted using the adsorbent materials; CHA, PHA and CCHA. Bone char (BCA) was included in the field water tests for comparison. For each adsorbent, a volume of 50 ml of fluorinated water was treated with 0.25 g of adsorbent for 12 h while shaking. Final pH and residue F^- was determined and adsorption capacity calculated using Eq. 3. F^- adsorption capacity in field and simulated water samples was modeled at room temperature (298 ± 2 K) using Langmuir, Freundlich, Dubinin-Radushkevich (D-R) and Temkin isotherms (Foo and Hameed, 2010). The most reliable equilibrium correlation was identified using the R^2 values. Effect of contact time, pH and temperature on the F^- removal efficiency was determined using field ground water sample with initial fluoride concentration of 29 mg/l. Time was varied between 10 - 180 minutes at room temperature and natural pH of the water, pH was varied in the 3-9 while temperature was varied in the range 298-325 K at natural pH of water.

3.3 Results and Discussion

3.3.1 Preparation of CAPs

Mineral content, Ca^{2+} concentration in acid liquors of crustacean shells and yields of adsorbents are shown in Table 7. Theoretical yields of adsorbent was calculated using Eq 4. The molarity of $CaCl_2$ liquors was calculated from Ca^{2+} concentration values obtained by EDTA complexation. Mineral content of crab shells was found be almost double that of prawns shells by both thermal analysis and wet chemisrty analysis. Mineral content by precipitation with sodium carbonate gave values slightly higher than that obtained by complexation of Ca^{2+} with EDTA. This was attributed to presence of other ions in the shell acid liquor which co-precipitated with Ca^{2+} , especially for crab shells. This observation was supported by presence of Si, Sr and Mn in the CAPs as seen in EDX data (Table 8).

Table 7: Mineral content, Ca²⁺ concentration in acid liquors and % yields of CAPs.

Parameter	Synthetic Ca ²⁺	Prawns shell	Crabs shell
Moisture (%)	-	7.0	7.0
Ash (%)	-	34.0	68.5
Mineral content by acid dissolution (%)	-	34.5	68.8
Mineral content by CO ₃ ²⁻ precipitation (g/l)	-	32.6	46.8
Ca ²⁺ conc by EDTA complexation (g/l)	-	27.7	43.7
Volume of Ca ²⁺ solution (ml)	250	300	300
Molarity of Ca ²⁺ solution (M)	1.09	0.69	1.09
Yield of CAPs Experimental (g)	27.2	17.5	32.1
Yield of CAPs Theoretical (g)	27.7	20.9	32.8
Efficiency (%)	99.6	83.8	97.7

3.3.2 Characterization of CAPs

Chemical composition of the CAPs by EDX analysis are presented in Table 9. Major components are CaO and P₂O₅ in all adsorbents. Traces K₂O and SrO were higher in prawns shell derived adsorbent than in crab shell system. SiO₂ and MnO were identified only in crab shell derived CAPs.

Table 8: Chemical composition of CAPs (wt%).

Adsorbent	Composition of oxide (%)					
	CaO	P ₂ O ₅	K ₂ O	SiO ₂	SrO	MnO
CCHA	70.8	29.2	-	-	-	-
PHA	65.0	30.8	2.5	-	1.6	-
CHA	60.1	35.7	1.8	1.5	0.6	0.3

XRD patterns for CCHA, PHA and CHA are given in Fig. 15. Diffraction phases of CCHA and PHA were identified by orientations 002, 211, 202 and 213 occurring at 2θ values 25.9, 32.0, 34.1 and 49.5 °, respectively. Calculated lattice parameters a = b = 9.434 and c = 6.920 Å corresponded to hexagonal phases of hydroxyapatite (HAP) referenced pattern of JCPDS Number 09-0432 (a = b = 9.432, c = 6.881 Å). XRD pattern of CHA revealed presence of mostly monoclinic structure with main phase orientation 020, 12-1, 14-1 at 2θ values 11.6, 20.9 and 29.3 °, respectively and lattice parameter, b = 15.32 Å. These phases corresponded to brushite (CaHPO₄·2H₂O) crystalline structure with lattice parameter, b = 15.18 Å as referenced in JCPDS 72-0713. HAP peaks (002, 211 and 202) were also identified but to a lesser extent.

Presence of brushite in hydroxyapatite crystals have been identified as factor of reaction aging time, in which after 24 h all brushite and other calcium phosphate should convert to more stable HAP (Rusu *et al.*, 2005). This does not however, explain the presence of major brushite phases in CHA, which was synthesized using the same reaction conditions of time and temperature as CCHA and PHA samples.

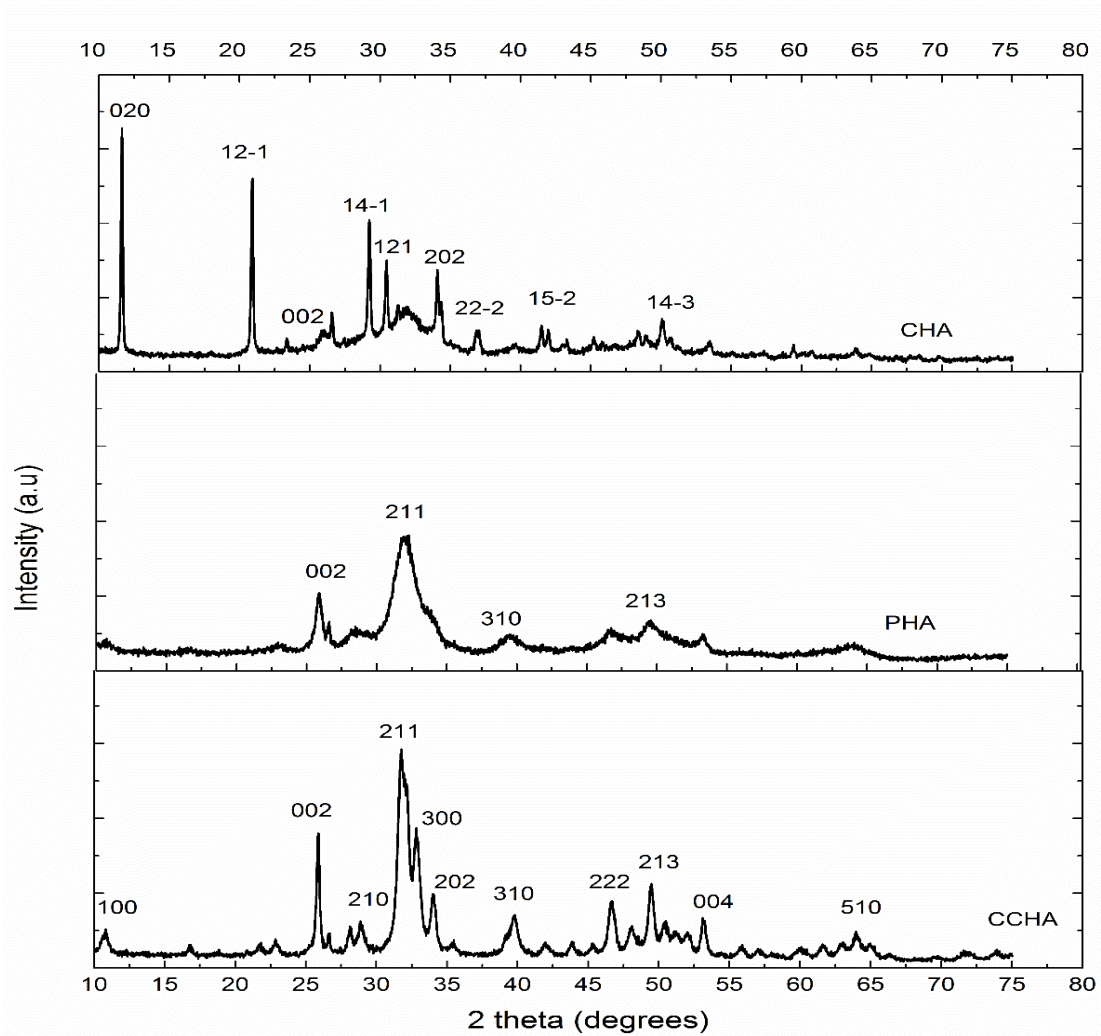


Figure 15: XRD patterns of CCHA, PHA and CHA.

PHA patterns were found to compare well with that of HAP synthesized using egg shells (Kashkarov *et al.*, 2011), while CHA pattern is identical to that reported for characteristic brushite crystals prepared by single diffusion gel technique (Rajendran and Dale Keefe, 2010). Average crystallite sizes was calculated using Scherrer's relationship; $L=0.94\lambda/\beta\cos\theta$, where β is the full width at half maximum (FWHM) of the peak.

The 002 peak was used to calculate CCHA and PHA crystallize sizes, giving 31 and 15 nm, respectively. Value for CCHA compare closely to L= 34 nm reported in literature = 34 nm (Rusu *et al.*, 2005). CHA was found to have average crystallite size, L= 47.9 nm using the (12-1) principle peak. The three sample thus produced nano-crytalline sizes as evidenced in Table 9.

Table 9: Selected XRD peaks analysis data for CAPs.

2θ peak (°)	D spacing (Å)	hkl	β-FWHM (°)	Crystallite size (nm)
CCHA				
25.80	3.46	002	0.2778	30.65
28.90	3.08	210	0.4690	18.28
32.00	2.81	211	1.2738	6.78
39.88	2.56	310	0.8878	9.95
46.49	1.95	222	0.5026	18.19
PHA				
25.89	3.44	002	0.5877	14.90
28.85	3.09	210	2.4484	3.50
32.06	2.79	211	1.8960	4.56
39.56	2.28	310	1.6613	5.21
46.80	1.94	222	0.9108	9.93
CHA				
11.62	7.61	020	0.1591	52.45
20.90	4.25	12-1	0.1761	47.93
29.23	3.05	210	0.2097	40.91
34.12	2.81	202	0.4377	19.84
41.50	2.17	15-2	0.2300	38.59

IR modes characterizing the adsorbents were determined in absorption mode, Fig. 16. The frequencies are assigned according to literature values (Panda *et al.*, 2003; Kashkarov *et al.*, 2011). Modes related to structural OH are observed in two regions; 620-635 cm⁻¹ and 3480-3570 cm⁻¹. Frequencies associated with PO₄³⁻ are identified in all samples, Table 10. The 1160-1204 cm⁻¹ intense peak observed in all sample was assigned to P=O stretching mode associated with PO₄ group (Rajendran and Dale Keefe, 2010). Spectra of CHA and PHA after defluoridation of groundwater with initial F⁻ of 29.4 mg/l are compared in Fig. 17. Only a slight difference is observed in the spent PHA (FPHA). There is split in the 630 cm⁻¹ peak forming two peaks, one to longer wavelength (620 cm⁻¹) and another to shorted wavelength 638 cm⁻¹ which is accompanied by a slight decrease in the absorption intensity of that peak (Fig. 17a).

This change has been identified earlier in pure HAP by (Freund and Knobel, 1977) but in their case the peak shifted completely from 630 cm^{-1} to $640\text{-}647\text{ cm}^{-1}$. The intense peak at 1175 cm^{-1} also shifts slightly to longer wavelength with reduced maximum intensity. The results indicate that only a small amount of F^- was adsorbed in the material as can be seen from F^- batch adsorption tests.

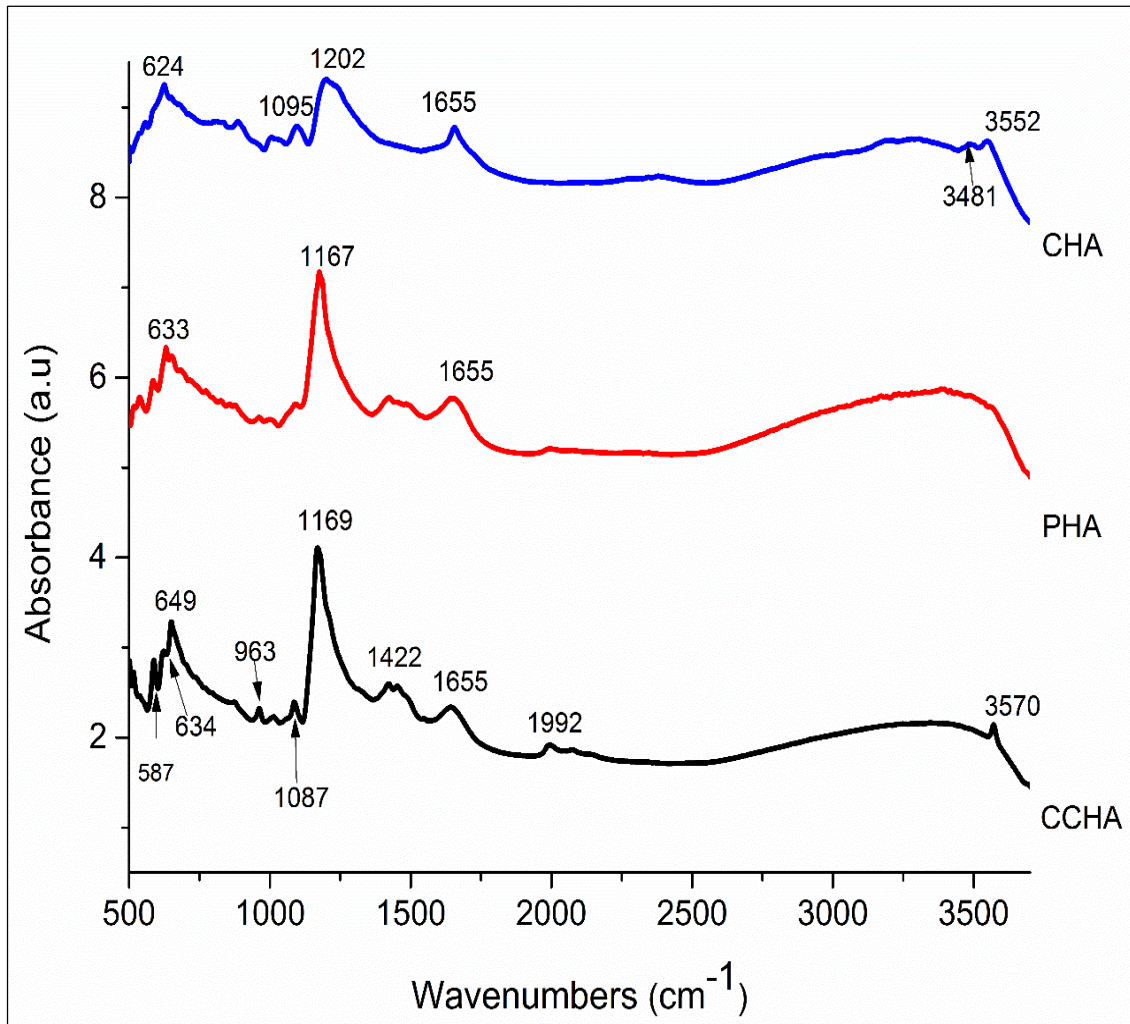


Figure 16: FT-IR spectra of CAPs adsorbents.

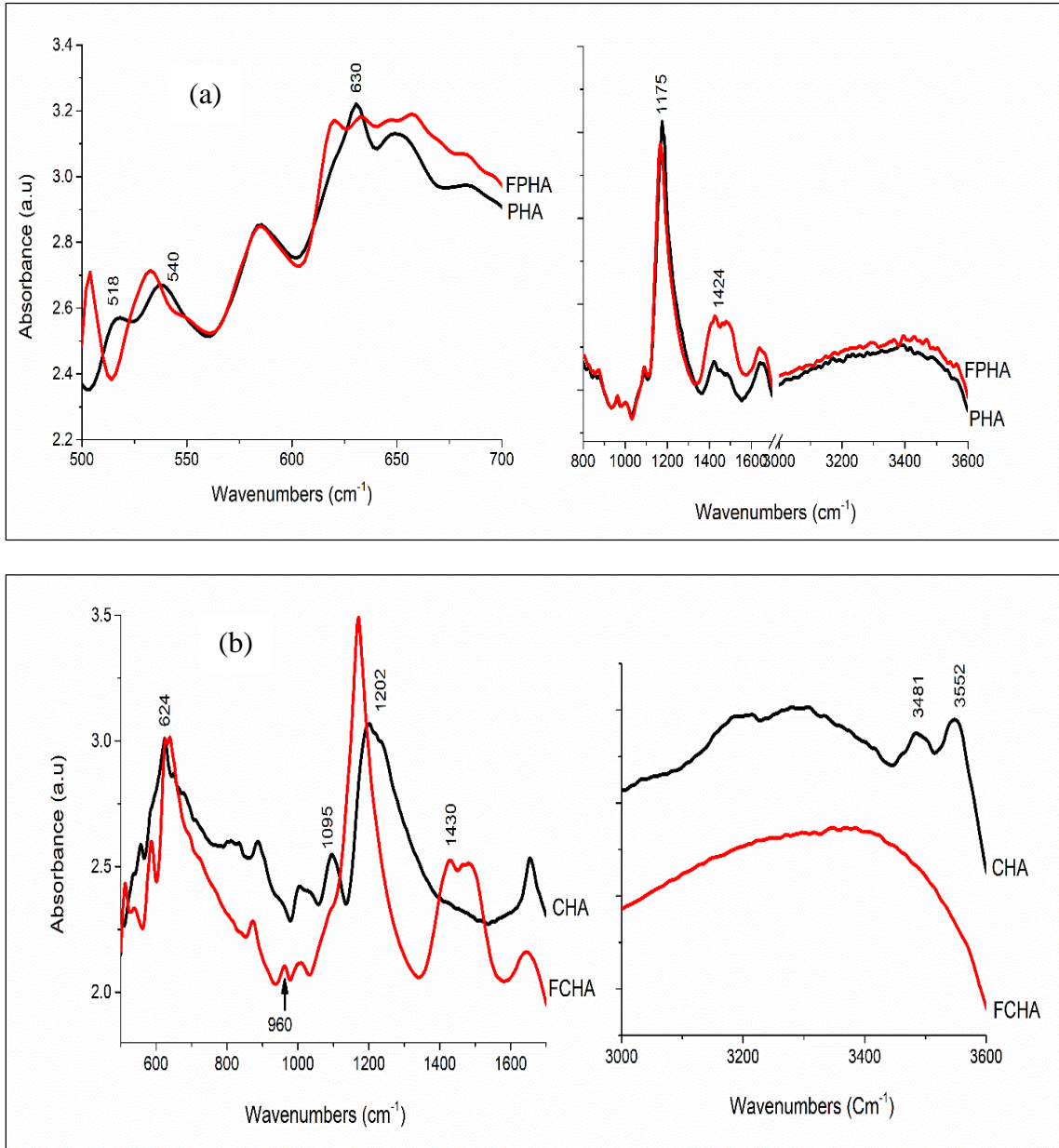


Figure 17: FT-IR spectra a) PHA and FPFA b) CHA and FCHA.

In CHA spectrum, significant decrease in absorption intensities was observed for most peaks. The 624 cm^{-1} peak shifted slightly to shorter wavelength and split into two peaks 627 and 639 cm^{-1} (Fig. 17b). This slight change in the peak position has also been reported in literature in case of fluorinated HAP (Sternitzke *et al.*, 2012).

The broad intense peak at 1202 cm^{-1} , became much narrower with shift to longer wavelength accompanied by increase in intensity. The bands at 3481 and 3552 cm^{-1} which are associated with structural OH bond stretching disappeared completely in FCHA. This indicate the OH group was effectively replaced by F^- in the water. A similar observation has been reported in literature (Namin *et al.*, 2008). This observation is well supported from F^- batch adsorption test which indicated CHA removed almost 95% of fluoride from the water

Table 10: IR frequencies for CAPs and fluoride adsorbed FPHA and FCHA.

Assignment	Vibrational frequencies				
	CCHA	PHA	FPHA	CHA	FCHA
IR Mode					
PO ₄ bending	588	583	583	584	586
Structural OH bending	620	630	638	624	635
P-O-P stretching	875	877	873	875	875
PO ₄ stretching	963	963	963	1004	961
PO ₄ bending	1087	1088	1089	1095	1081
PO ₄ P=O stretching	1169	1169	1175	1202	1169
CO ₃ ⁻ group	1422	1420	1424	-	1424
H ₂ O adsorbed	1651	1651	1655	1655	1655
Structural OH stretch	3770	-	-	3552	-

3.3.3 Batch absorption test

Parameters of field water samples collected from 7 points sources in the same ward are presented in Table 11. All samples were found to contain F^- above permissible limits of 1.5 mg/l and ORP below 400-650 mV which is deemed necessary for oxidation of contaminants like bacterial pathogens (Goncharuk *et al.*, 2010). Most of the water samples (F4-F7) were very turbid and thus failed quality test for EC and TDS. EC of 800-1000 $\mu\text{s}/\text{cm}$ and TDS 500 mg/l are acceptable for drinking water for humans and animals. Surface water samples (F3, F5 and F7) failed to meet quality standards for microbial and color requirements. Color values above 15 units are considered unacceptable for human consumption but up to 85 units is found in natural drinking waters (WHO, 2011).

Table 11: Water quality parameters of field samples.

ID	Source	Color (pt Co)	Temp (°C)	pH	ORP (mV)	DO (ppm)	EC (µS/cm)	TDS (ppm)	PO ₄ ³⁻ (mg/)	E.Coli (CFU/100 ml)	F ⁻ (mg/l)
F1	spring	7.0	16.7	7.6	92.2	6.4	483	242	0.27	00	4.20
F2	spring	8.0	19.2	7.5	91.6	5.2	816	408	0.12	00	6.48
F3	River	215.0	19.8	8.3	-6.5	6.3	445	223	0.21	200	18.70
F4	shallow well	6.0	22.0	8.0	50.6	5.6	2883	1441	0.13	00	29.40
F5	stream	710.0	24.0	9.5	21.3	7.2	2062	1032	0.71	232	31.00
F6	shallow well	6.0	23.0	8.1	39.0	5.72	3500	1749	0.13	00	33.70
F7	swamp	3781.0	26.9	8.6	190.9	3.06	4352	2178	0.65	17	70.10

F⁻ adsorption test were carried out at natural pH of the water with adsorbent dose of 0.25 g/50 ml of fluorinated water, results are shown in Table 12. Defluoridation efficiencies and capacities of the adsorbent in simulated and field water are shown in Fig. 18. The adsorption capacity indicates number of adsorption sites and available specific surface area, it's thus a thermodynamic value at equilibrium. Adsorption efficiency on the other hand tell us about the tendency of adsorbate to adsorb compared to stay in solution, the kinetic value (the rates) of adsorption.

Defluoridation capacities in low F⁻ levels (4 - 10 mg/l) was found be almost same for all adsorbents. Above 10 mg/l, a distinctive trend in performance of adsorbents is observed as follows; CHA > PHA > CCHA. Adsorption capacities of the three CAPs in simulated water of 10 mg/l are CCHA = 1.852 mg/g, PHA = 1.882 mg/g and CHA = 1.933mg/g. These results compares closely with that reported for nano-HAP, 1.845 mg/g (Sundaram *et al.*, 2008a). For high fluoride simulated water, CHA recorded the highest efficiency of 21 mg/g. This matches capacity of 19.7 mg/g reported for nano-HAP derived from waste phosphogypsum (Zhang *et al.*, 2012). In the field water samples, the highest capacities of the adsorbents in water with F⁻ concentration of 70 mg/l are 13.6, 8.5 and 2.6 for CHA, PHA and CCHA, respectively. No data was found from literature on performance of calcium phosphate based adsorbent in the field waters with fluoride concentration above 10 mg/l.

From these data it can be seen that CHA exhibits superior fluoride removal in both simulated and field waters. PHA and CCHA adsorbent materials were found appropriate for F⁻ levels below 10 mg/l, with PHA performing much better than CCHA.

Table 12: Batch adsorption test with different materials.

F ⁻ residue after 12 h treatment (pH final)							
Sample	Source	pH initial	F ⁻ initial (mg/l)	CCHA	PHA	CHA	BCA*
S1	simulated	5.90	10.30±0.1	1.01±0.2 (8.0)	0.86±0.2 (6.8)	0.607 (6.6)	-
S2	simulated	3.80	50.60±0.4	21.67±0.8(8.2)	4.95±0.2 (6.2)	0.362 (5.8)	-
S3	simulated	3.87	106.00±3.0	80.00±2.7 (7.7)	56.5±1.5 (6.4)	0.977(5.9)	-
Field waters							
F1	spring	7.60	4.20	0.64±0.3 (8.1)	0.85±0.4 (8.0)	0.275 (6.8)	1.9 (8.5)
F2	spring	7.53	6.48±0.1	1.21 (8.2)	0.74±0.2 (8.0)	0.470±0.1 (7.0)	2.6±0.2 (8.5)
F3	River	8.30	18.70	8.66±0.2 (8.0)	2.83±0.0 (7.9)	0.221 (7.3)	9.0±0.4 (8.8)
F4	shallow well	8.00	29.40±1.6	14.67±0.8 (8.4)	6.02±0.2 (8.4)	0.582±0.2 (8.0)	17.4±0.3 (8.9)
F5	stream	9.50	31.00±1.4	21.7±0.1 (9.3)	9.54±0.4 (9.1)	0.485±0.1 (7.8)	22.0 (9.4)
F6	shallow well	8.10	33.70±1.5	18.87±0.7 (8.4)	6.60±0.4 (8.5)	0.569±0.2 (8.2)	21.9±0.2 (8.8)
F7	swamp	8.60	70.10±4.2	57.20±1.6 (8.8)	27.57±0.3 (8.6)	2.160±0.4 (8.1)	57.0±0.1 (8.8)

* BCA was in granular form as obtained from defluoridation center. It thus not included in the analysis of powered adsorbed synthesized in the laboratory.

Effect of adsorbent on water quality parameters was tested for CHA adsorbent using two water samples: a shallow well sample (F4) and surface water sample (F5) which had yellow color tint. Results shown in Table 13 indicate that CHA significantly reduced color in F5. The ability of CHA adsorbent to remove color can be explained by presence of MnO in the elemental composition, Table 8. MnO or hydroxides are known to promote degradation of complex organics such as humic acid, PCBs and phenols (Tebo *et al.*, 2004). The adsorbent did not have any effect on the microbial count and increased the level of phosphate slightly. No other major changes were observed in other water qualities.

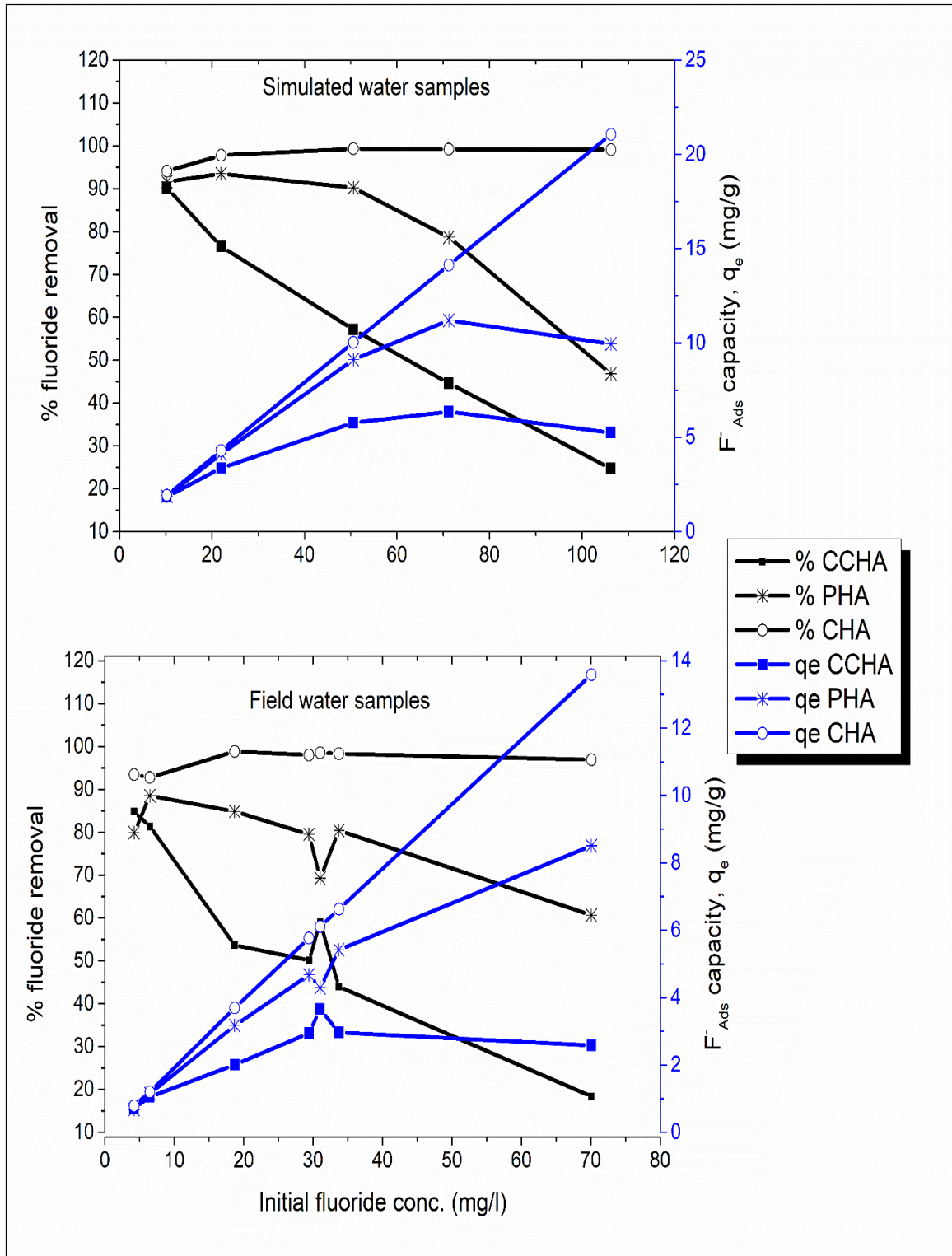


Figure 18: F^- removal efficiency (%) and adsorption capacities (q_e) of CAPs.

Table 13: Water quality parameters before and after treatment with CHA.

ID	Lab parameters	Color (pt Co)	pH	ORP (mV)	DO (ppm)	EC ($\mu\text{S}/\text{cm}$)	TDS (ppm)	PO_4^{3-} (mg/l)	E.Coli (CFU/100 ml)	F^- (mg/l)
F4	Before	6.00	8.4	149	5.2	2815	1440	0.1	00	29.40
	After	12.0	7.8	84.1	4.14	2767	1385	2.4	00	0.58
F5	Before	710.00	9.6	124	4.4	1904	959	0.7	232	31.00
	After	109	7.5	81	4.5	1952	977	2.8	232	0.49

3.3.4 Effect of pH

Influence of pH on adsorption of fluoride to CCHA, PHA and CHA using ground water sample, F4 (initial fluoride = 29.4 mg/l). The pH was varied from 3-8.5 at room temperature (25 ± 2 °C) for 180 minutes. Results of fluoride removal as a function of initial pH of the solution and final pH of treated water are shown in Fig. 19. The efficiency of all adsorbent decreased with increase in pH, and best removal was achieved at pH = 3 with over 95% removal. This can be explained by the fact that at acidic pH, protonation of surface sites responsible for binding F^- from solution occurs thus raising the adsorbents ability to uptake F^- . This phenomenon has been observed with most adsorbents for fluoride from solution (Medellin-Castillo *et al.*, 2007; Tang *et al.*, 2009; Alagumuthu and Rajan, 2010). The pH is thus one of the most important process parameter controlling the fluoride adsorbent interaction.

CCHA was most affected by change in pH, its ability to remove fluoride decreased from 96 % at pH = 3 to 42 % at pH = 8.5. PHA removal efficiency decreased within a narrow range between pH 3-5 (97-82%). For CCHA and PHA which are purely hydroxyapatite, pH > 7 was found to limit their ability significantly. Treatment at pH = 3, though excellent efficiency was achieved, its practical application could be limited because of need for acid/alkali treatment of water before and after F^- removal as the final pH of the treated water is 5.6-5.7 which is below recommended pH for drinking water. Crab shell derived adsorbent, CHA performed extremely well at all pH with efficiency range of 99-96% between pH 3-8.5.

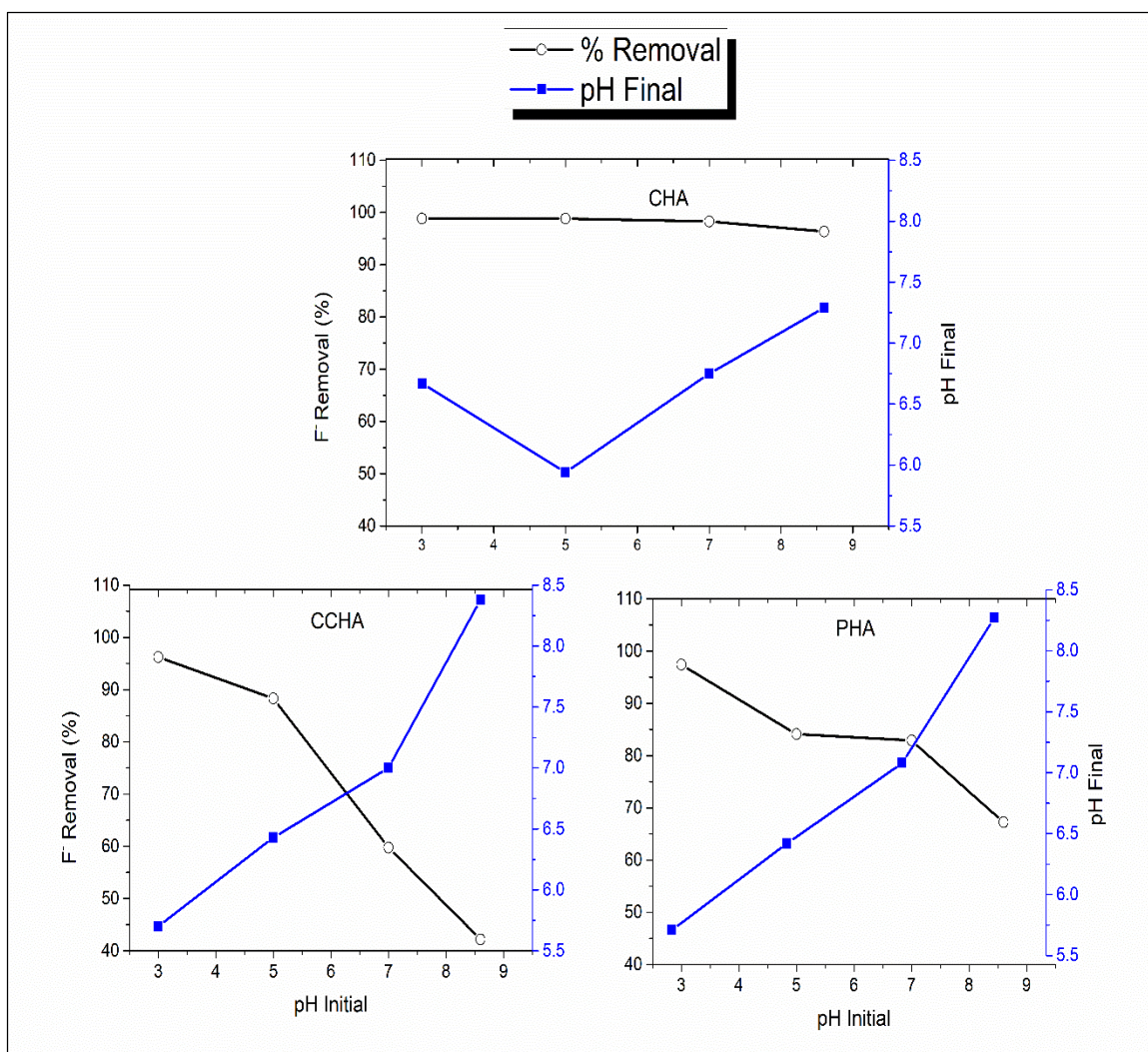


Figure 19: Adsorption of fluoride on CAPs as function of pH.

3.3.5 Adsorption isotherms

Adsorption isotherms describe the relationship between the adsorbate in aqueous phase and the adsorbate on the surface of the adsorbent at equilibrium in a given temperature and pH. The adsorption isotherm is important in designing adsorption systems and assessing their performance (Kumar and Sivanesan, 2005). Adsorption equilibrium (ratio between the adsorbed amount with the remaining in the solution) is established when an adsorbate and adsorbent have been in contact for sufficient time, determined by varying contact time up to a point when increase in time does not change the concentration of adsorbate in bulk solution.

For solid - liquid systems, several isotherm equations are available in both linear and nonlinear regression forms, including: Langmuir, Freundlich, Temkin and Dubinin-Radushkevich (D-R) models (Foo and Hameed, 2010). Linear regression are simple and most frequently used to produce the optimal goodness of fit between experimental data and predicted data. This method assumes that the scatter vertical points around the line follows a Gaussian distribution and that the error distribution is uniform at every value of the liquid-phase residual concentration. Such behavior has been indicated to be practically impossible with the equilibrium relationships as the error distribution tended to get altered after transformation into a linearized order (Wong *et al.*, 2004). In another investigation, linearized Langmuir and Freundlich isotherm models were shown to be inappropriate in predicting the goodness of fit for a particular set of variables (Mane *et al.*, 2007), and unable to provide a fundamental understanding of the ions adsorption systems, resulting in erroneous interpretation of adsorption behavior. On the contrary, nonlinear isotherm models are conducted on the same abscissa and ordinate, which minimizes the sum of the squared difference between experimental data and predicted data to yield a more precise and accurate estimation (Ayoob and Gupta, 2008).

In this work, adsorption characteristics of the CAPs in both simulated and field water was tested at room temperature (298 ± 2 °C) using the above mentioned models in linear and non-linear forms as described in Table 14. Adsorption equilibrium considered for modelling was that determined after contact time of 12 h (Table 12). Nonlinear adsorption isotherms fitted using SOLVER-add available in Microsoft excel are shown in Fig. 20 and the corresponding data in Table 15. Linearized data are illustrated in Table 16. The general observation is that adsorption data characteristics of the materials in simulated water is very different from what is observed in field waters in terms of adsorption capacity. Specifically, CCHA which recorded the lowest adsorption capacities was best modeled by linear Langmuir isotherm with $R^2 > 0.98$ for both simulated and field waters. This signifies a monolayer adsorption of a homogenous adsorbent (Günay *et al.*, 2007). This observation can be supported from XRD and EDX data which show only hydroxyapatite phases are present in the material.

Table 14: Two parameter adsorption isotherms equations.

Non-linear form	Linear form	Plot	Parameters
Langmuir $q_e = \frac{q_m K_L C_e}{1 + K_L C_e}$	$\frac{C_e}{q_e} = \frac{1}{b K_L C_e} + \frac{C_e}{q_m}$ I $\frac{1}{q_e} = \frac{1}{q_m} + \frac{1}{b q_m C_e}$ II	C_e/q_e vs C_e $1/q_e$ vs $1/C_e$	C_e =F concentration at equilibrium (mg/L), q_e = Adsorption capacity at equilibrium (mg/g), q_m = Maximum adsorption capacity (mg/g) and K_L =Langmuir constant (L/mg)
Freundlich $q_e = K_F C_e^{1/n}$	$\log q_e = \log K_F + \frac{1}{n} \log C_e$	$\log q_e$ vs $\log C_e$	K_F = Freundlich constant (mg/g)
Dubinin-R $q_e = (q_m) \text{Exp}(-K_{ad} \varepsilon^2)$	$\ln q_e = \ln q_m - K_{ad} \varepsilon^2$ $\varepsilon = RT \ln[1+1/C_e]$ $E = (2K_{ad})^{1/2}$	$\ln q_e$ vs ε^2	K_{ad} =adsorption equilibrium constant (mol ² /kJ ²), ε = Polanyi potential, E=mean free energy of adsorption (kJ/mol), R= gas constant (8.314J/mol/K) and T= Temperature at 298K.
Temkin $q_e = \frac{RT}{b_T} \ln(K_T C_e)$	$q_e = \frac{RT}{b_T} \ln K_T + \frac{RT}{b_T} \ln C_e$	q_e vs $\ln C_e$	K_T = equilibrium constant (L/g) and b = constant related to heat of adsorption (J/mol),

PHA adsorbent was best characterized by D-R isotherm in linear and non-linear form for simulated water, $R^2 > 0.98$. However for field water, Temkin was found to model the adsorption in both linear and non-linear mode more effectively with $R^2 > 0.90$. This could indicate multimolecular layers coverage in nanosized adsorbent (Foo and Hameed, 2010) as seen with XRD crystallite size of about 15 nm in Table 9. CHA, which adsorbed fluoride best from both simulated and field waters was barely modeled by linear regression analysis. Nonlinear D-R isotherm fairly represented simulated water adsorption characteristics with $R^2 = 0.82$ while fluoride adsorption in field water was equally modeled by all four isotherm with $R^2 = 0.77-0.80$. The difficulty to model CHA was attributed to multiphase structure which showed presence of mainly brushite and hydroxyapatite in the crystal lattice. Presence of MnO which has catalytic properties on the surface may also have contributed to the heterogeneity resulting in different adsorption characteristics with enhanced ability of the adsorbent to remove fluoride.

Table 15: Nonlinear isotherms constants for adsorption of F⁻ onto CAPs.

Parameter/model	Simulated water			Field water		
	CCHA	PHA	CHA	CCHA	PHA	CHA
Langmuir						
q _m (mg/g)	6.176	11.707	2913.541	3.204	10.524	32.458
K _L (L/mg)	0.325	0.428	0.006	0.470	0.124	0.336
R ²	0.900	0.910	0.409	0.790	0.930	0.804
Freundlich						
KF (mg/L)	2.523	4.750	20.554	1.411	1.741	7.701
n	4.743	4.380	0.669	4.583	2.070	1.331
R ²	0.756	0.646	0.461	0.575	0.921	0.799
Temkin						
K _T (L/g)	7.934	5.987	4.113	7.726	1.858	5.556
b _T	2.526	1.196	0.205	4.422	1.259	0.481
R ²	0.833	0.774	0.325	0.684	0.930	0.768
Dubinin-Radushkevich						
qm (mg/g)	6.673	11.481	18.177	2.854	6.782	15.446
E (kJ/mol)	2.027	1.236	0.635	1.381	0.279	3.216
R ²	0.903	0.984	0.815	0.776	0.788	0.793

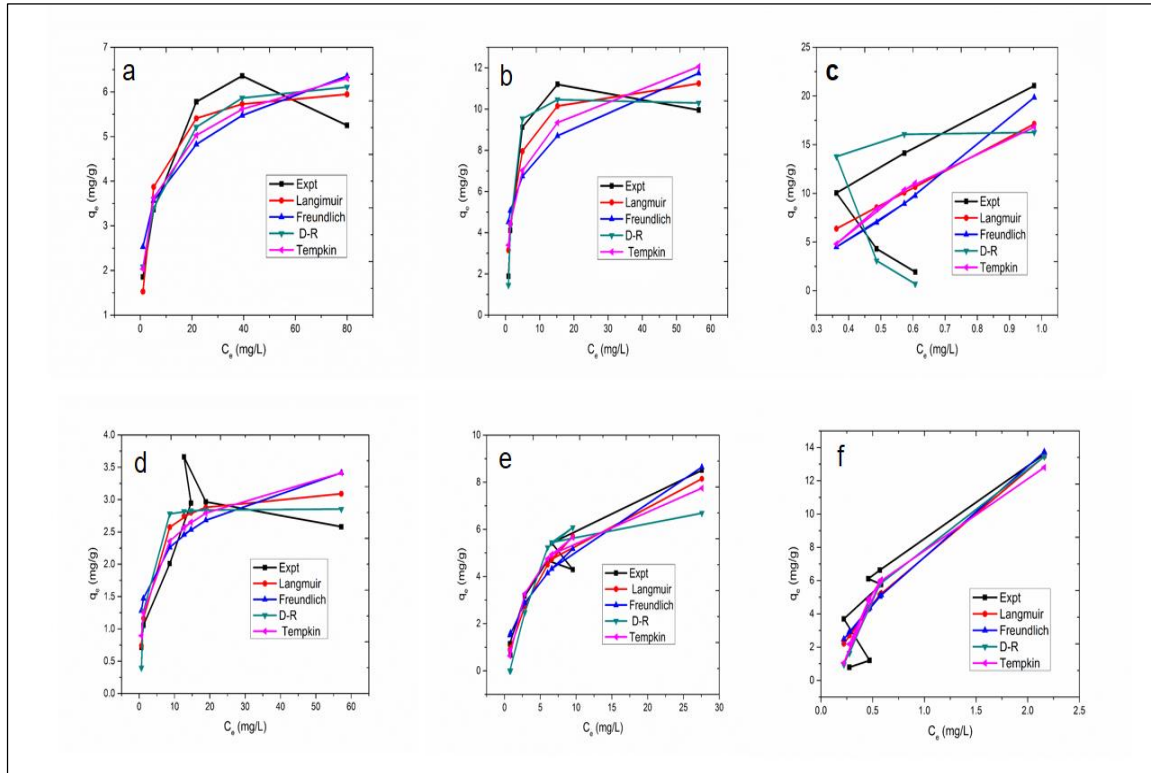


Figure 20: Non-linear adsorption isotherms of fluoride in different CAPs. *a,b,c* are simulated water fluoride adsorption in CCHA, PHA and CHA respectively while *d,e* and *f* are isotherm for field water fluoride in CCHA, PHA and CHA respectively.

Table 16: Linear isotherms constants for adsorption of F⁻ onto CAPs.

Parameter/model	Simulated water			Field water		
	CCHA	PHA	CHA	CCHA	PHA	CHA
Langmuir						
q _m (mg/g)	5.490	10.360	-	2.650	11.060	-
K _L (L/mg)	0.015	0.015	-	0.021	0.076	-
R ²	0.986	0.994	0.001	0.985	0.883	0.008
Freundlich						
K _F (mg/L)	2.054	3.151	-	1.000	1.201	-
n	3.662	2.648	-	2.925	1.526	-
R ²	0.872	0.725	0.095	0.800	0.894	0.445
Temkin						
K _T (L/g)	7.933	5.987	-	7.726	1.858	5.610
b _T	0.977	2.071	-	0.560	1.968	5.151
R ²	0.833	0.774	0.324	0.684	0.930	0.768
Dubinin-Radushkevich						
q _m (mg/g)	5.174	10.270	-	2.692	5.302	-
K (mol ² /kJ ²)	0.361	0.477	-	0.269	0.435	-
E (KJ/mol)	1.176	1.024	-	1.363	1.073	-
R ²	0.820	0.991	0.04	0.851	0.858	0.376

3.3.6 Effect of contact time and adsorption kinetics

Variation of F⁻ adsorption with contact time was studied for CAPs using field water sample F4, Fig. 21. The results indicate that for all the CAPs the uptakes was very rapid within the first 10 min with > 75% of the possible F⁻ adsorbed. CCHA for instance was able to remove 37% of the possible 42% maximum in the first 10 minutes. The process proceeds at a slow rate for the rest of reaction time. The optimum performance for all the CAPs was best after 120 minutes of adsorption. The pH also decreased significantly in the first 10 minutes and then very slightly during the rest of adsorption time. In order to define the adsorption mechanism and possible rate-determining steps for removal of fluoride in water using the CAPs adsorbent, data obtained from effect of contact time on F⁻ adsorption was analyzed using 4 kinetic models: pseudo 1st order, pseudo 2nd order, intra-particle diffusion and Elovich kinetic models (Demirbas *et al.*, 2004; Ayoob *et al.*, 2008), linear plots of these models are summarized in Table 17. The conformity between experimental data and the model calculated values was expressed by the correlation coefficients (R²) value which indicates the extent to which model successfully describes the kinetics of adsorption.

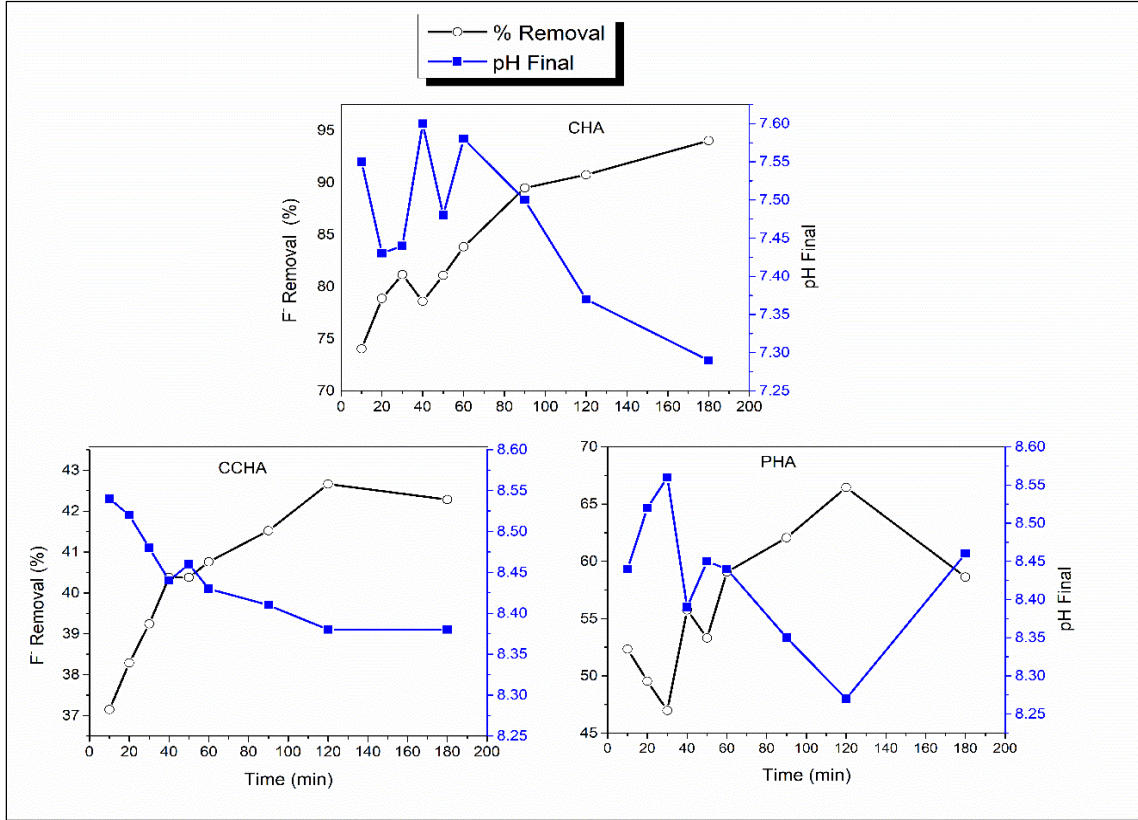


Figure 21: Variation of F⁻ removal with contact time using field water sample (F4).

Table 17: Kinetic models equations

	Linear from	Plot	Parameters
Pseudo 1 st order	$\log (q_e - q_t) = \log q_e - \frac{K_1}{2.302} t$	$\log (q_e - q_t) \text{ vs } t$	q_e =F- adsorbed at equilibrium (mg/g) q_t = F- adsorbed at time 't'(mg/g) K_1 =Rate constant for pseudo 1 st order (min ⁻¹)
Pseudo 2 st order	$\frac{t}{q_t} = \frac{1}{K_s (q_e)^2} + \frac{t}{q_e}$	$t/q_e \text{ vs } t$	K_s =Rate constant for pseudo 2 nd order (g/(mg.min))
Intra-particle diffusion	$q_t = K_{ip} t^{1/2} + C$	$q_e \text{ vs } \ln t$	K_{ip} =intra-particle diffusion (mg/(g.min ^{1/2})) C= intercept
Elovich	$q_t = \frac{1}{\beta} \ln(\alpha\beta) + \frac{1}{\beta} \ln t$	$q_t \text{ vs } \ln t$	α = initial adsorption (mg/(g.min)) β = desorption constant (g/mg)

The results presented in Table 18 show that the pseudo 2nd order model described the kinetic process of F⁻ adsorption on the CAPS more appropriately compared to other models (Fig. 22). The adsorption is thus controlled by second order mechanism. The calculated q_e values agree very well with the experimental values and $R^2 > 0.99$ shows that the model can be applied for the entire adsorption process and confirms chemisorption (Qiu *et al.*, 2009) for all CAPs. Individually, CCHA was also well modelled by Elovich equation with R^2 value 0.96, this further confirms chemisorption onto a heterogeneous surface. PHA was strictly modeled by pseudo second order kinetics. CHA was accurately modeled by all the 4 equations with $R^2 > 0.9$. This means it was difficult to make predictions as several mechanism could be invoked, hence the high adsorption capacity observed with even high concentration of fluoride in filed waters.

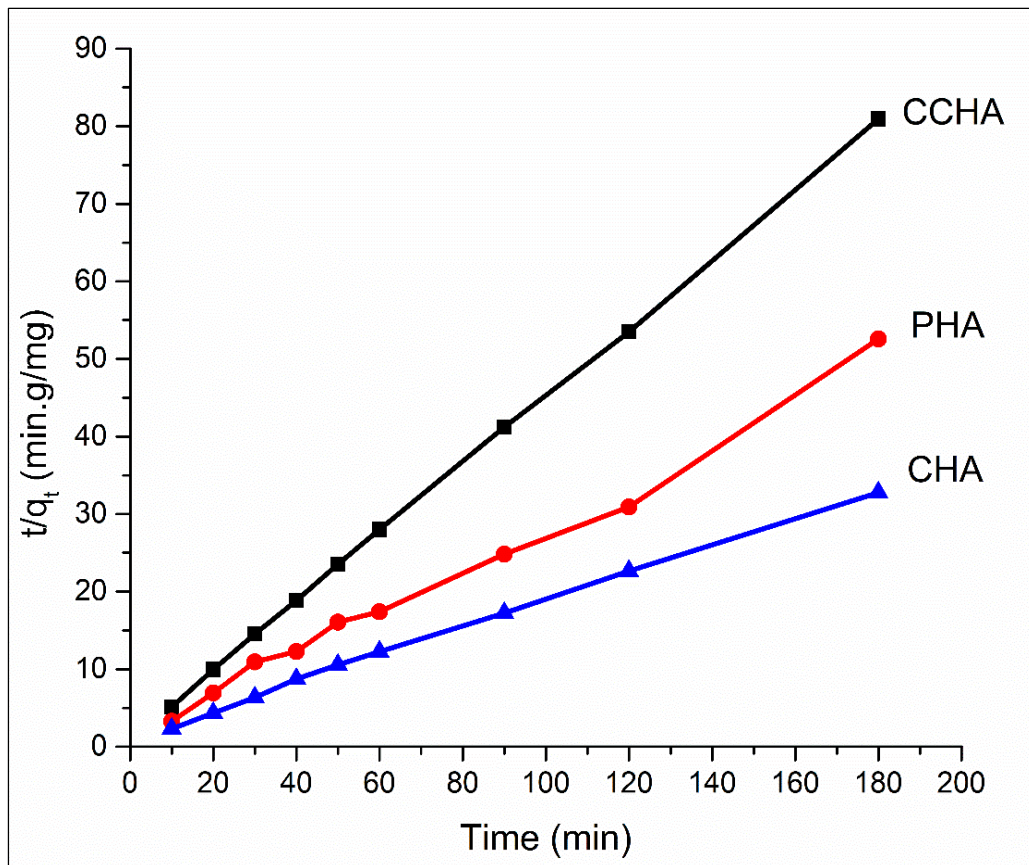


Figure 22: Pseudo-2nd order kinetic plots for fluoride adsorption on CAPs.

Table 18: Kinetic parameters of CAPs.

Parameter/model	CCHA	PHA	CHA
Pseudo 1 st order			
q _{mcal} (mg/g)	1.00	0.84	0.98
q _{mexp} (mg/g)	2.22	3.88	5.40
K ₁ (L/mg)	0.64	-0.0039	1.97
R ²	0.29	0.18	0.94
Pseudo 2 nd order			
q _{mcal} (mg/g)	2.26	3.65	5.62
q _{mexp} (mg/g)	2.22	3.88	5.40
K _s (g/mg.min)	0.180	0.06	0.03
R ²	1.00	0.99	1.00
Intra-particle diffusion			
C	1.91	2.65	-32.52
K _{ip} (mg/g.min ^{1/2})	0.03	0.08	8.22
R ²	0.88	0.55	0.94
<i>Elovich</i>			
β	9.64	3.37	2.48
R ²	0.96	0.55	0.91

3.3.7 Effect of temperature and thermodynamic parameters

Influence of temperature on the adsorption of F⁻ was verified at temperatures of 300-327 K using groundwater sample (F4) at its natural pH for 180 minutes (Fig. 23). The free energy change (ΔG°) was calculated from the variation of the thermodynamic equilibrium constant, $K_C = q_e/C_e$, at different temperatures. Thermodynamic parameters were calculated using Gibbs energy and Van't Hoff Equations (Eqs 5-6) as described in (Anastopoulos and Kyzas, 2016). The slope and intercept of Van't Hoff Plot (Fig. 24) was used to calculate enthalpy of reaction (ΔH) and Entropy (ΔS), Table 19.

$$\Delta G = - RT \ln\left(\frac{q_e}{C_e}\right) \quad (5)$$

$$\ln\left(\frac{q_e}{C_e}\right) = -\frac{\Delta H}{R} \left[\frac{1}{T}\right] + \frac{\Delta S}{R} \quad (6)$$

where, T is the temperature in Kelvin, R is the universal gas constant (8.314 J/mol K), C_e is fluoride concentration at equilibrium (mg/L) and q_e is the adsorption capacity at equilibrium (mg/g).

The values of ΔG indicated that adsorption process was nonspontaneous for CCHA, PHA and spontaneous for CHA. The best temperature for adsorption for all the CAPs was identified as $T = 307 \text{ K}$, although the adsorption was barely affected by increase in temperature. Positive values of ΔH suggested the endothermic nature of adsorption, which may be also evidenced from the slight increase F^- removal by the CAPs at temperatures 300-308 K. The positive value of $\Delta S \ll \ll \ll 1$ suggested no changes in randomness occur at the solid/liquid interface during the adsorption process.

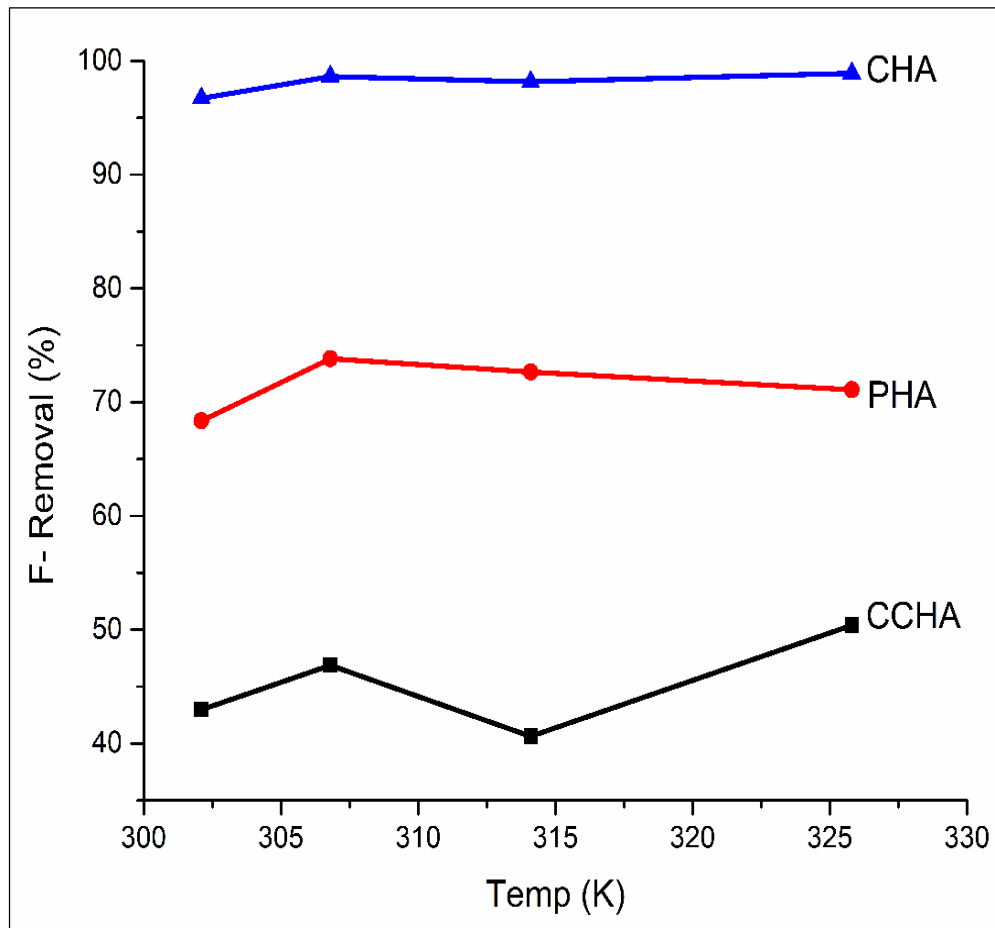


Figure 23: Variation of F^- adsorption with temperature of the medium.

Table 19: Thermodynamic parameters of interaction of F⁻ with CAPS.

Adsorbent	Temp (K)	ΔG (kJ mol ⁻¹)	ΔH (kJ mol ⁻¹)	ΔS (kJ mol ⁻¹ K ⁻¹)
CCHA	302	4.75	6.61	0.009
	307	4.42		
	314	5.19		
	325	4.32		
PHA	302	2.10	1.99	0.0007
	307	1.46		
	314	1.65		
	325	1.92		
CHA	302	-4.47	29.78	0.12
	307	-6.81		
	314	-6.19		
	325	-7.84		

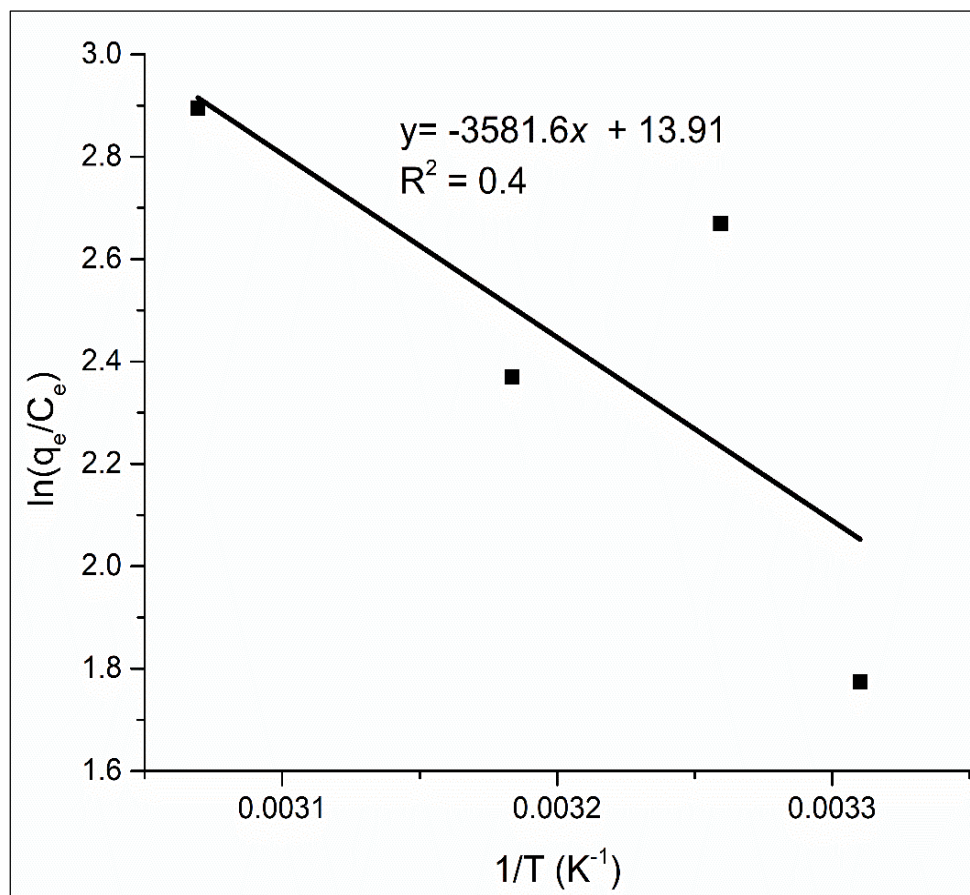
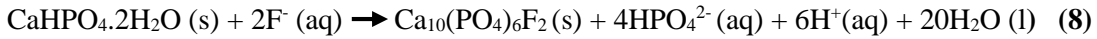
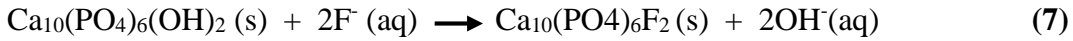


Figure 24: Van't Hoff Plot for CHA.

3.3.8 Elucidation of F⁻ removal mechanism

Mechanisms of F⁻ uptake from solutions has been evaluated by several authors (Tafu and Chohji, 2006; Sternitzke *et al.*, 2012; Zhang *et al.*, 2012). Three main processes are highlighted; Ion exchange, electrostatic adsorption and precipitation. In this study, mechanism was elucidated from kinetic and FT-IR analysis. In the spectra (Fig. 17), shift or disappearance of bands related to OH and HPO₄ bands accompanied by changes in intensity after adsorption was assumed to indicate F⁻ substitution and formation of fluorapatite by CHA and PHA as follows;



Kinetic tests showed equilibrium pH increased slightly in PHA treated water while it decreased in CHA during the rapid uptake. This was seen to confirm release of OH⁻ and H⁺ into solution from the above reactions. Slow process was predicted to indicate electrostatic adsorption which increased with decrease in pH. It can thus be concluded that though ion exchange plays a significant role, it is not the only force driving the removal of F⁻ from solution by the CAPs.

3.4 Conclusion

Calcium phosphate adsorbents derived from crustacean biomass waste have been developed using inexpensive low temperature precipitation method. The process of calcium isolation is versatile because it also allows recovery of other bioactive components like chitin which has valuable applications. Analytical characterization using XRD and FT-IR show that prawn shell produced predominantly hydroxyapatite with nanocrystallite size (~15 nm), while crab shell gave mostly brushite with average crystallite size of around 50 nm. The adsorbents are found to have excellent defluoridation capacities. The crab shell based adsorbent (CHA) recorded the highest capacity of 13.5 mg/g while prawn shell based hydroxyapatite (PHA) gave 8.5 mg/g. These capacities are order of magnitude higher than that of synthetic hydroxyapatite (2.6 mg/g) and bone char (2.6 mg/g) using field water with F⁻ concentration of 70 mg/l.

Higher capacities for fluoride removal were observed at lower pH (3-5). Kinetic study results indicated that the adsorption process followed a pseudo 2nd order kinetic model and the adsorption was better defined by non-linear Langmuir equation. Anion exchange is proposed as the main driving force for fluoride uptake onto CAPs surfaces. The results indicate that PHA adsorbent would be most fit for treating water with F⁻ levels of 10 mg/L and below while CHA is suitable for waters with higher F levels, in a wide pH 3 - 8.5 with efficiencies of 98-96%, meaning no pH adjustments are required for treatment process. These materials are thus very appropriate for high F⁻ waters found in East African Rift valley, where bone char has been the most used material despite having lower adsorption capacity and much stringent condition of temperature during preparation. The crustacean derived adsorbents were also found to considerably reduce color in tinted water samples, which adds to quality of the treated water. A slight increase in phosphate level was identified with all the adsorbents.

CHAPTER FOUR

Preparation and Characterization of Chitosan-Calcium Phosphate Composite³

Abstract

Chitosan polymer has been combined with crab shell derived brushite to form chitosan/hydroxyapatite composite. XRD and FT-IR analysis confirmed transformation of brushite phases into hydroxyapatite and formation hybrid structure. F⁻ adsorption tests, performed in batch mode recorded defluoridation capacity of up to 3.7 mg/g in field water containing fluoride concentration of 5-30 mg/l. The best performance with efficiency above 85% was observed with F⁻ concentration of 10 mg/L and below. The adsorption capacities were best modeled by Temkin adsorption isotherm and pseudo 2nd order kinetics. A part from F⁻ removal, the composite also reduced color tint and fecal coliforms significantly from surface water samples. The pH of the treated water remained around 6-9, which is acceptable for drinking water.

4.1 Introduction

Biomaterials research field is currently geared towards finding of sustainable and safe solutions to environmental pollutions and biomedical treatments. Among different materials, natural polymer-based nano-composites have become a prominent area of current research and development (Pighinelli and Kucharska, 2013). Among such materials are composites containing calcium phosphates and chitosan polymer. These composite have been intensively investigated for bone tissue engineering and water treatment applications mostly due to their compatibility, non-toxicity, mechanical strength, stability and presence of active functional groups which allow applicability by chelation, electrostatic attraction and chemical bonding (Abueva *et al.*, 2017). Majority of work on the calcium phosphate composites has been focused in biomedical application in bone regeneration (Araújo *et al.*, 2006; Danilchenko *et al.*, 2011; Pighinelli and Kucharska, 2013).

³ Published in MRS Advances (2018). DOI: 10.1557/adv.2018.206

Applications of the composite for water treatment are mostly reported in the removal of heavy metals, dyes from waste water and anionic contaminations such as nitrates and fluoride (Hou *et al.*, 2012; Saber-Samandari *et al.*, 2014; Yong Lei, 2015). Among the anionic pollutants, F⁻ is singled out as the most severe natural contaminant in drinking water.

Preparation of chitosan/ hydroxyapatite composite is mainly based on co-precipitation of calcium and phosphate precursors with chitosan solution. For instance, (NH₄)₂HPO₄ has been reacted with CaCl₂ solution for 30 minutes at 40 °C and the precipitate allowed to age 12 h. During the precipitation process, the pH of solution was maintained at 10.0 by addition of ammonia. HAP obtained was filtered off, washed with distilled water, and dried at 60 °C for 2 days and then dispersed in a solution of chitosan in acetic acid to yield a homogenous suspension after stirring for 12 h. The solution was then precipitated with 0.1 M NaOH to obtain chitosan - HAP composite (Yong Lei, 2015). Another literature reports addition of chitosan solution in 8.5% H₃PO₄ followed by reaction with Ca(OH)₂ in alkaline media (Yamaguchi *et al.*, 2001). Aqueous solutions of NH₄H₂PO₄, Ca(NO₃)₂·4H₂O and chitosan have also been used as precursors. The precipitate formed was rinsed with water to pH level 7, dried at 80 °C and calcined to 400 °C to get nano-HAP/chitosan composite (Sundaram *et al.*, 2008b). NaH₂PO₄·2H₂O has also been indicated as source of phosphate (Guo *et al.*, 2015).

In this work, crab shell brushite and chitosan isolated from prawns shell were investigated as precursors for composite which was then tested for F⁻ removal efficiency and activity against microbes in natural surface water. Composite preparation is discussed, together with its functional characteristic as identified using XRD and FT-IR analytical methods. Results of adsorption of F⁻ from ground and surface water in presence of *E. coli* microbes are presented to support effectiveness of the composite in water treatment.

4.2 Materials and Methods

4.2.1 Raw materials

Prawns shell chitosan, (DDA =83.5%) and crab shell brushite were prepared in using procedures described in chapters 2 and 3, respectively. Glacial acetic acid and sodium hydroxide used were of analytical grade from Sigma Aldrich.

4.2.2 Preparation and characterization of chitosan-hydroxyapatite (Cs-HA)

Approximately 5g of chitosan powder (CHS) was dissolved in 250 ml of 1% acetic acid. The mixture was stirred 40 °C for 24 h to completely dissolve chitosan. Undissolved chitosan particles were filtered out using a kitchen stainless fine sieve with mesh size 0.45 mm. To the homogenous chitosan acetate solution, 5 g of brushite powder was slowly dispersed and the mixture agitated vigorously using a magnetic stirrer for 24 h to achieve homogenous mixing. The colloidal mixture was then precipitated with 0.25 M NaOH. Precipitate was filtered and rinsed to neutral pH using distilled water, oven dried at 60 °C for 24 h and then ground into powder. Composite was characterized using XRD, FT-IR and EDS as described in chapter 3 (section 3.2.3). Microbial contamination was determined using plate count on agar media incubated at 44.5 °C for 24 h. Levels of phosphates and color were measured using HACHI DR/2800 spectrophotometer.

4.2.3 Batch adsorption tests

Batch adsorption experiments were conducted using, 0.25g of Cs-HA mixed with 50 ml of field and simulated water samples with different initial fluoride concentration as described in chapters 2 and 3. Final pH and residue F⁻ concentration was determined and adsorption capacity calculated. Effect of contact time, pH and temperature on F⁻ removal was determined as described in chapter 3.

4.3 Results and Discussion

4.3.1 Characterization of chitosan - hydroxyapatite

The % of major components, CaO and P₂O₅ changed significantly in Cs-HA compared to precursor CHA (Table 20). Trace elements in CHA; K⁺, Si⁴⁺ and Mn²⁺ were not identified in the Cs-HA. In fluoride treated composite (F.Cs-HA), K⁺ and Mn²⁺ resurfaced. This may signify that chitosan may have taken up the cations in solutions and given them up a fluoride from solution.

Table 20: Chemical composition Cs-HA, F.Cs-HA and CHA (wt%).

	% composition of oxide					
Adsorbent	CaO	P ₂ O ₅	K ₂ O	SiO ₂	SrO	MnO
Cs-HA	73.33	25.03	-	-	1.64	-
F.Cs-HA	73.88	22.46	2.44	-	0.70	0.52
CHA	60.14	35.71	1.83	1.48	0.59	0.26

XRD patterns of CHS, CHA and Cs-HA are given in Fig. 25. XRD peaks associated with monoclinic structure CHA were found to transform into to hexagonal phases of hydroxyapatite in the composite. Characteristic chitosan peaks was observed at $2\theta = 20.1^\circ$ with low intensity in the composite. Details of intensities and position of the peaks for Cs-HA are shown in Table 21. Transformation of crystalline peaks in CHA into hydroxyapatite phases observed in XRD pattern can also be supported by changes in the ratio CaO and P₂O₅ in Table 20. Treatment of CHS/CHA colloidal mixture with 0.25 M NaOH during preparation stage can be seen as the cause of the transformation considering information available in literature (Guo *et al.*, 2015). Average crystallite sizes was calculated using Scherrer's relationship; $L=0.94\lambda/\beta\cos\theta$ considering the 211 peak position which gave $L=27.08$ nm. This value is slightly lower compared to that reported in literature, $L = 34$ nm (Rusu *et al.*, 2005)

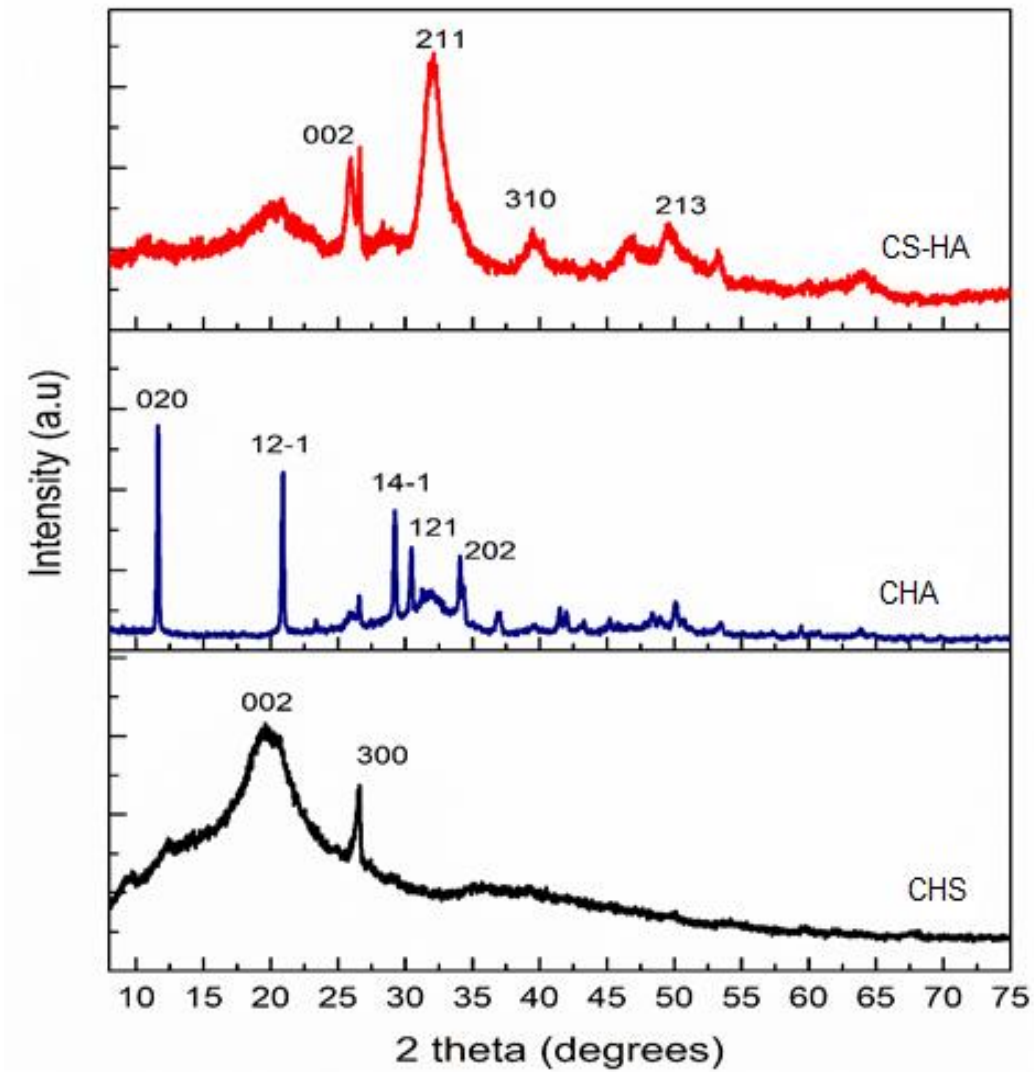


Figure 25: XRD patterns of Cs-HA, CHA and CHS.

Table 21: Selected XRD peaks analysis data for Cs-HA.

2θ peak max (°)	D spacing (Å)	100.*I/Imax	β-FWHM (°)	Crystallite size (nm)
20.89	4.25	22.56	0.5047	16.7
25.89	3.44	63.14	1.1778	7.2
26.58	3.35	74.04	0.3189	26.7
32.02	2.79	100.00	0.3189	27.1
39.45	2.28	44.50	0.4983	17.7
46.97	1.93	21.46	0.9376	9.6

FT-IR modes characteristic of both chitosan and hydroxyapatite were observed in Cs-HA composites, Fig. 26. Specifically, CH vibration, NH₂ and OH bands of chitosan are positively identified in the composite. PO₄ vibration modes in the region 500-1200 cm⁻¹ and OH bands at 624 and 3400-3500 cm⁻¹ in the composite were assigned hydroxyapatite phases.

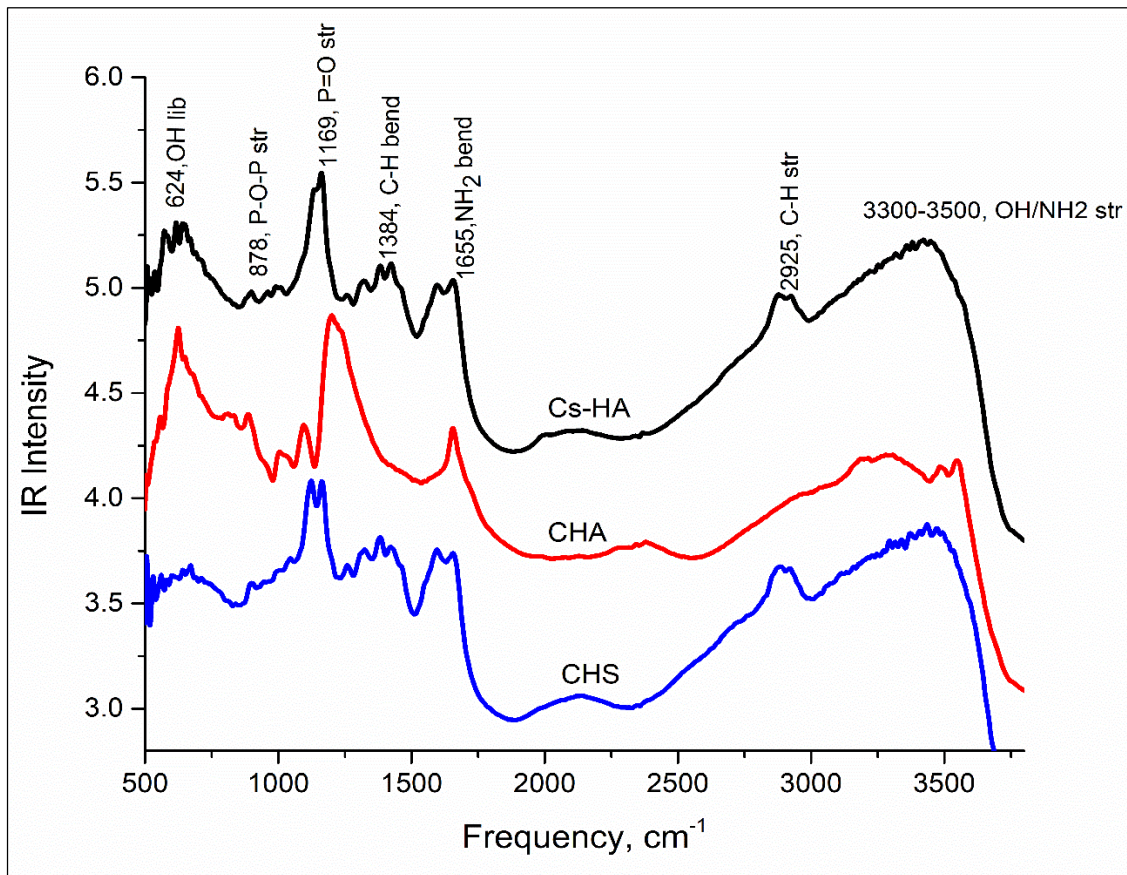


Figure 26: FT-IR patterns of Cs-HA, CHA and CHS.

Analysis of frequencies after defluoridation of groundwater with initial fluoride of 29 mg/l are shown in Fig. 27. General increase in the IR intensities of fluoride treated Cs-HA is observed in most regions, except in the peaks at 571, 615 and 645 cm⁻¹ which are shifted to higher wavenumbers accompanied with significant decrease in IR intensities. This indicate decrease in OH vibration due to uptake of F⁻ from solutions (Freund and Knobel, 1977).

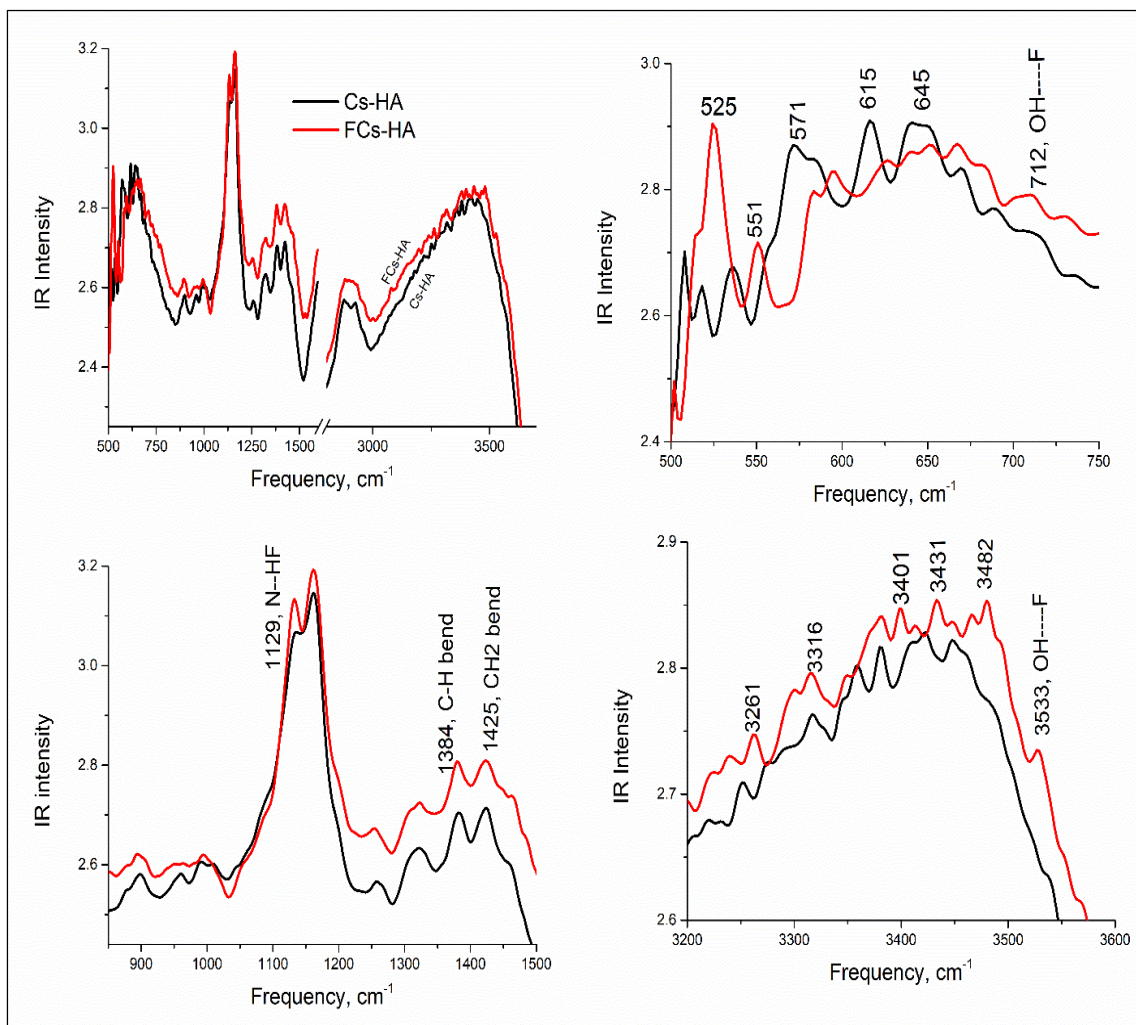


Figure 27: Analysis of FT-IR spectra of Cs-HA and FCs-HA.

4.3.2 Batch absorption test

Fluoride adsorption test were carried out using field water and simulated water at natural pH of the water and adsorbent concentration of 0.25g/50ml, results are shown in Table 22 with final pH indicated. The pH of treated water in all water samples was found to be within an acceptable range of 6-9 for drinking water. The fact the water did not require any adjustment of pH before and after defluoridation show that material have practical applicability that is not seen with most of the reported adsorbents for fluoride (Meenakshi and Maheshwari, 2006).

Table 22: Batch adsorption test with Cs-HA.

Sample	Source	pH initial	F ⁻ initial mg/l	Ecoli initial CFU/100 ml	pH final	F ⁻ final mg/l	Ecoli final CFU/100 ml
S1	simulated	5.90	10.27±0.1	-	7.70	0.70	-
S2	simulated	3.80	50.56±0.4	-	7.13	19.10±0.4	-
S3	simulated	3.87	106.3±3.0	-	7.32	74.00±1.4	-
Field water							
F1	spring	7.60	4.20	0	8.17	0.36±0.2	-
F2	spring	7.53	6.48±0.1	0	8.05	0.72±0.1	-
F3	River	8.30	18.70	200	7.80	4.81	09
F4	shallow well	8.00	29.40±1.6	0	8.53	9.80±0.2	-
F5	stream	9.50	31.00±1.4	232	9.33	15.25±0.1	39
F6	shallow well	8.10	33.70±1.5	0	8.54	13.10±0.2	-
F7	swamp	8.60	70.10±4.2	17	8.75	38.00±0.4	-

Defluoridation efficiency was found to decrease with rise in F⁻ concentrations while capacity increased with increase in initial fluoride concentration in both field and simulated water samples (Fig. 28). Adsorption capacity of crab shell derived Cs-Ha (1.90 mg/g) is higher than that reported for synthetic Cs-Ha (1.56 mg/g) using simulated waters of 10 mg/l (Sundaram *et al.*, 2008b). This could be attributed to presence of traces of Sr and Mn in the crab shell CAP precursor, which is not the case with synthetic one.

Effect of adsorbent on water quality parameters was tested using surface water sample (F5) which had yellow color tint. The results are shown in Fig. 29. Almost 50% of the color tint was removed while fecal coliform counts reduced significantly. This was attributed presence of MnO and chitosan phases in the crystal lattice of Cs-HA. Manganese oxides or hydroxides are known to promote degradation of complex organics such as humic acid, polychlorinated biphenyls (PCBs) and phenols (Tebo *et al.*, 2004). The level of phosphates in treated water remained relatively the same signifying stability of the adsorbent in solution. No other major changes were observed in other water qualities.

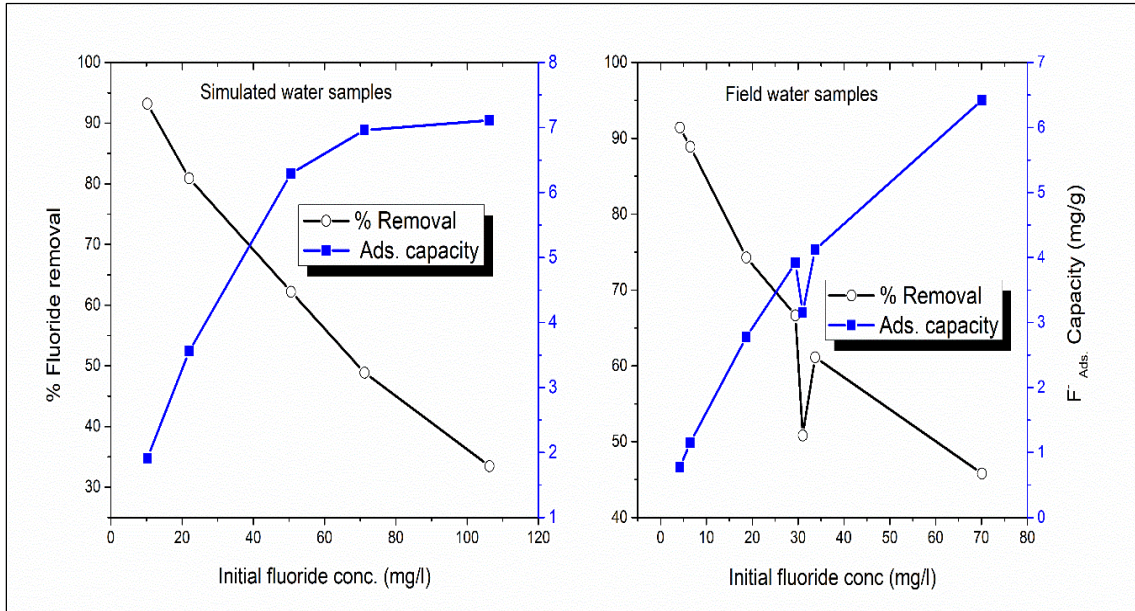


Figure 28: Efficiency of F⁻ removal and adsorption capacities by Cs-HA.

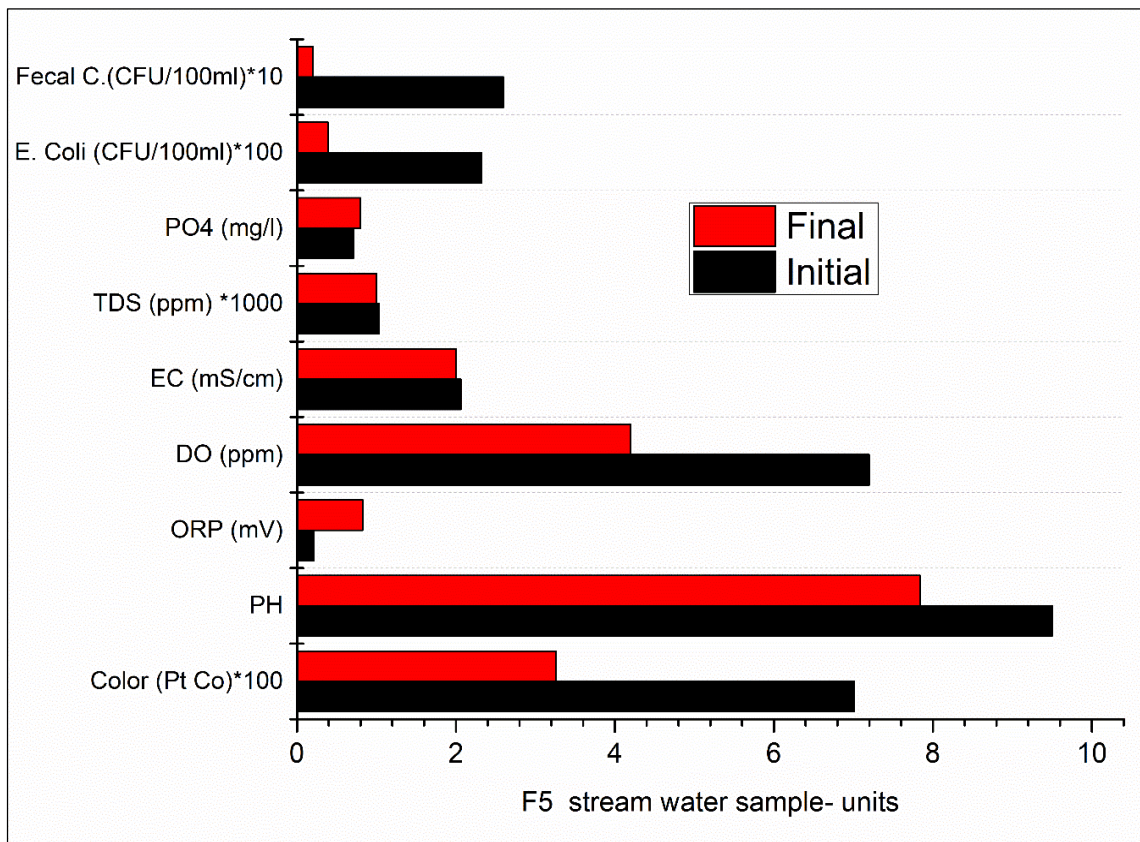


Figure 29: Water quality parameters before and after treatment with Cs-HA.

4.3.3 Effect of pH

Field water samples with high F^- concentration (> 15 mg/L) are found to also have high pH (8-9.5). The effects of the pH on adsorption efficiency of Cs-HA was thus studied to determine the optimum applicable pH for removal of F^- in groundwater sample with initial F^- concentration > 25 mg/l and pH 9. A gradual decrease in fluoride removal was observed with increase in pH (Fig. 30). The best removal (85 %) was recorded at pH 3 with the final pH of treated water at 6.7, which acceptable for drinking water. F^- concentration at the original pH of the water (8.6) was 4 times lower than at pH = 3. The high pH in the groundwater may be as result of excess HCO_3^- as seen in characterization of groundwater sample in Northern Tanzania (Ghiglieri *et al.*, 2012). The HCO_3^- in solution compete strongly with F^- for adsorption sites on the adsorbent thus low F^- removal at high pH.

In lower pH, protonation of the adsorbent surface and reduction of HCO_3^- occurs, thus increasing the adsorbent's ability to bind F^- significantly. The main challenge with applicability of adsorption at such low pH is the requirement for initial acid treatment of the water. While it could be possible for large scale centralized water treatment before supply, it may be difficult for household water treatment applications. The trend in F^- removal Vs pH observed in Cs-HA is similar to that seen for CHA (Fig. 19). This because Cs-Ha was a composite of CHA and chitosan, meaning that active component for F^- adsorption is the crab shell derived calcium phosphate. The % removal in Cs-HA were lower because the amount of CAPs is lower in composite as compared to pure CAPs given same adsorbent loading weight.

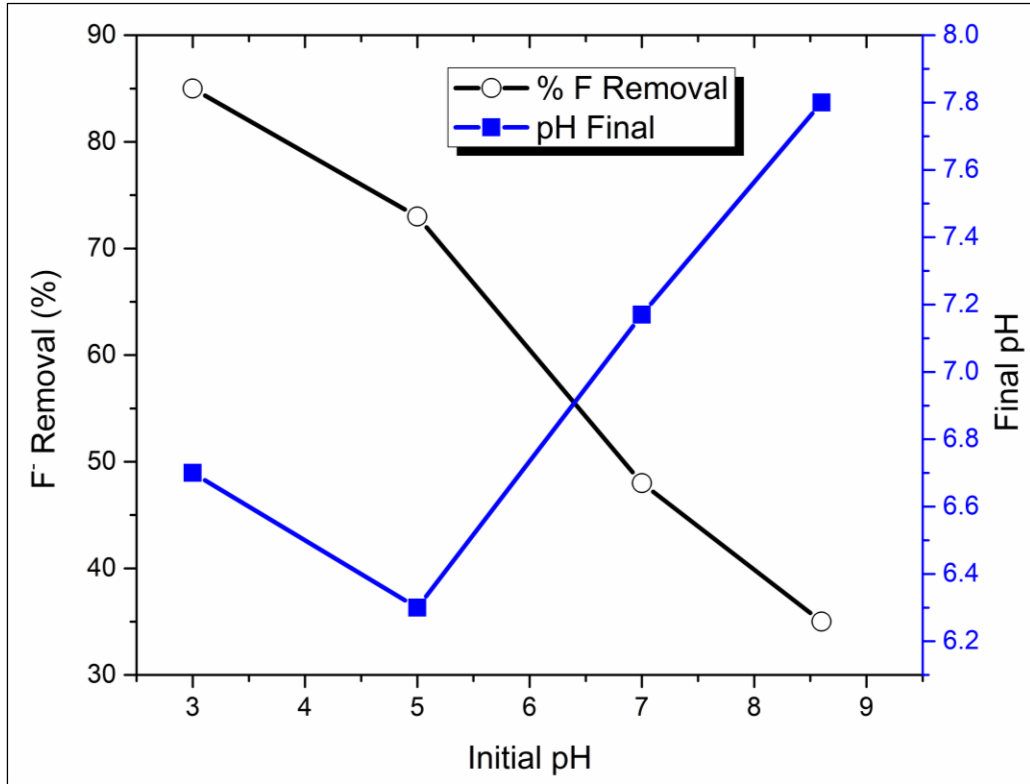


Figure 30: Effect of pH on removal of F⁻ from solution by Cs-HA.

4.3.4 Adsorption isotherms

Linear regression adsorption isotherm are presented in Fig. 31 and parameters associated with each model are illustrated in Table 23. The overall observation is that Langmuir 2 and Freundlich models had the highest correlation coefficient $R^2 > 0.95$, however, the adsorption capacities estimated from the two isotherm deviated more from the experimental data as compared to Temkin and D-R models (Table 24). For the field water, Temkin model calculated adsorption capacity agreed best with the experimentally determined capacities. This could indicate multimolecular layers coverage in nanosized adsorbent (Foo and Hameed, 2010) as seen with XRD crystallite size of about 27 nm in Table 21. Similarly, simulated water adsorption capacity was represented better by D-R isotherm despite having lower R^2 values than Langmuir and Freundlich models. It can thus be concluded that reliance on R^2 alone without considering the standard error in the

computed values could be erroneous, this phenomenon is well explained in (Kinniburgh, 1986; Chen, 2015).

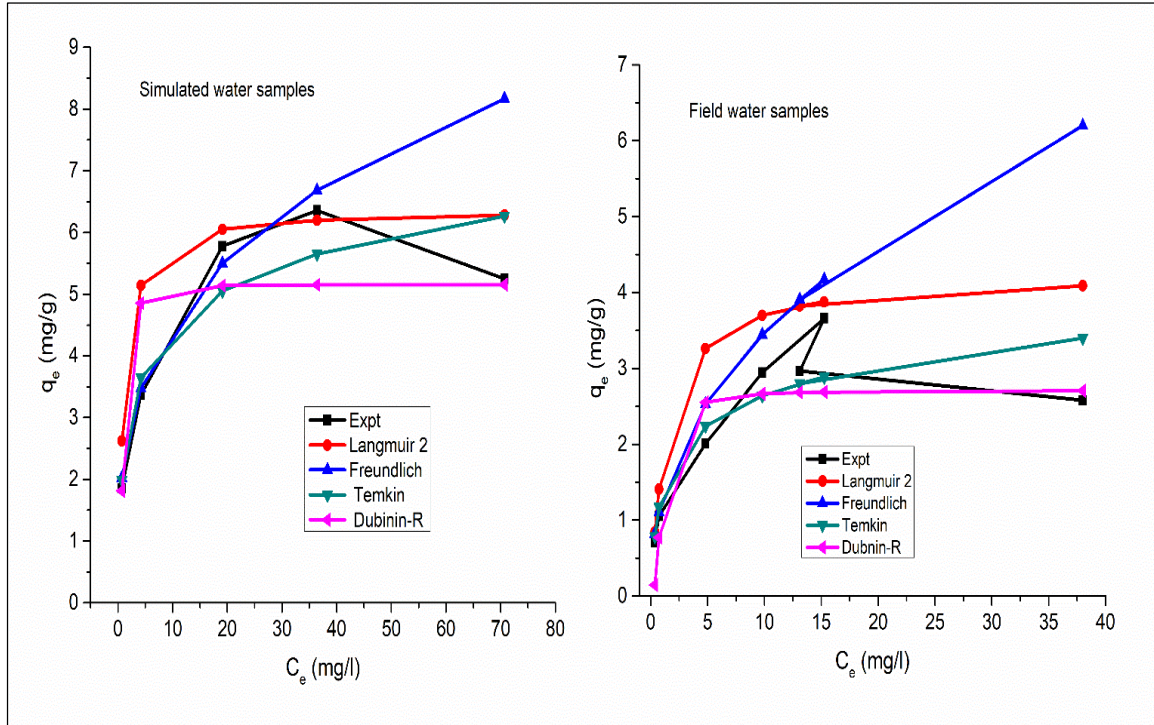


Figure 31: Linear regression adsorption isotherms for F^- in on Cs-HA.

Table 23: Linear isotherms constants for adsorption of F^- onto Cs-HA.

Parameter/model	Simulated water	Field water
Langmuir 2		
q_m (mg/g)	6.369	4.246
K_L (L/mg)	1.000	0.690
R^2	0.9548	0.978
Freundlich		
KF (mg/L)	3.310	2.306
n	2.257	1.280
R^2	0.967	0.966
Temkin		
K_T (L/g)	12.177	11.229
b_T	0.927	0.561
R^2	0.845	0.789
Dubinin-Radushkevich		
q_m (mg/g)	5.174	2.692
K (mol^2/kJ^2)	0.216	0.269
E (kJ/mol)	1.521	1.363
R^2	0.815	0.851

Table 24: Experimental and predicted F⁻ adsorption q_e on to Cs-HA composite.

Simulated water						
F ⁻ initial	C _e (mg/l)	q _e (mg/g)				
		Expt	Langmuir 2	Freundlich	Temkin	D-R
10.30	0.70	1.85	2.62	2.03	1.99	1.81
50.60	19.10	5.78	6.05	5.50	5.05	5.14
106.30	70.70	5.25	6.28	8.17	6.27	5.16
Field water						
4.20	0.36	0.71	0.84	0.82	0.79	0.15
6.50	0.72	1.05	1.41	1.11	1.17	0.77
18.70	4.81	2.01	3.26	2.53	2.24	2.55
29.40	9.80	2.95	3.70	3.44	2.64	2.67
31.00	15.25	3.66	3.88	4.17	2.89	2.69
33.70	13.10	2.97	3.82	3.91	2.80	2.68
70.10	38.00	2.58	4.09	6.20	3.40	2.71

4.3.5 Effect of contact time and adsorption kinetics

The kinetics of F⁻ adsorption on Cs-HA was modeled using pseudo-first order, second order, first order intra-particle diffusion and Elovich relations (Swain *et al.*, 2010). Ground water sample with initial fluoride concentration sample of 24 mg/l was treated with adsorbent dose of 0.25 g/50 ml at its natural pH = 9.3. Time was varied from 10-180 minutes at room temperature (289±2 K). The efficiency of F⁻ removal increased with time and reached saturation point after 80 minutes with about 40% of fluoride removal (Fig. 32). The low removal efficiency was attributed to high initial pH of the water sample.

Table 25: Kinetic parameters of F⁻ adsorption on Cs-HA.

K_1 (L/mg), K_s (g/mg.min), K_{ip} (mg/g.min^{1/2}), q_{cal} (mg/g)

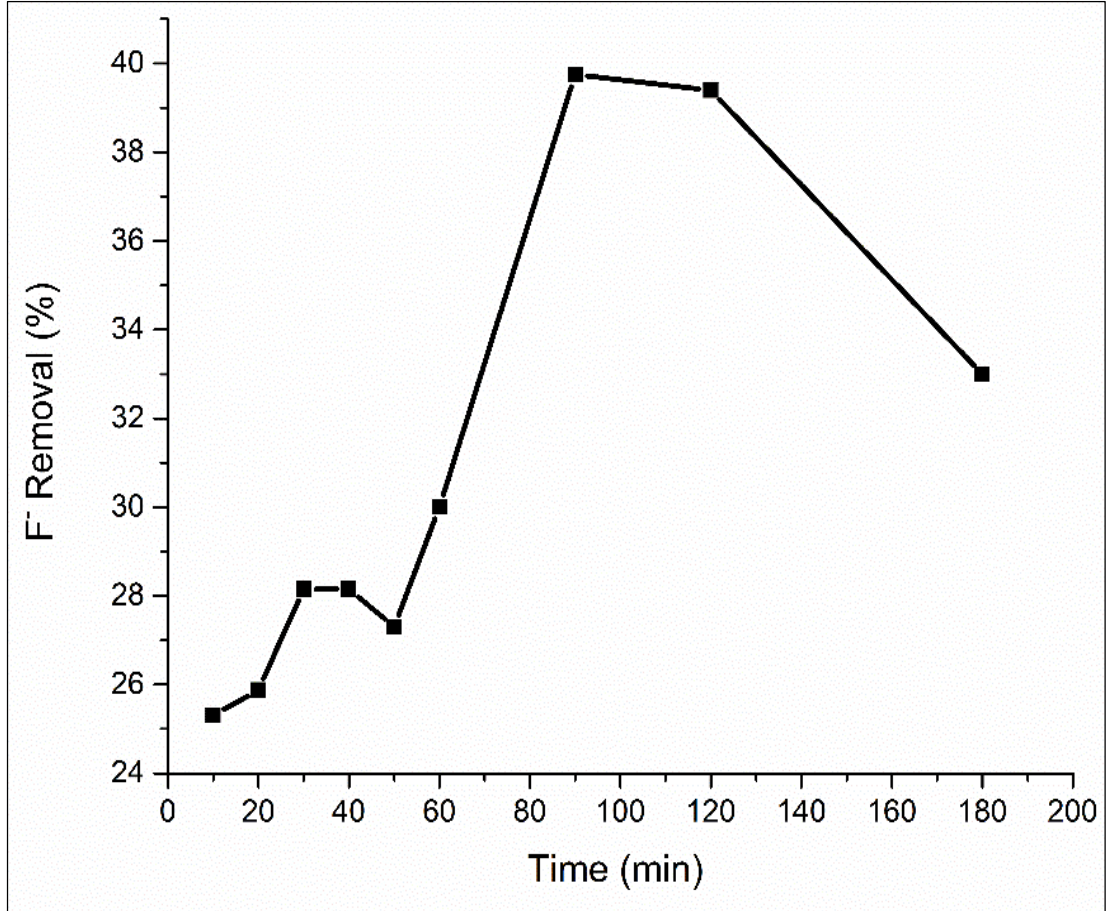


Figure 32: Effect of contact time of F⁻ adsorption to Cs-HA.

Parameter/model	q_{cal}	q_{exp}	K_1	K_s	C	K_{ip}	β	R^2
1st Pseudo kinetics	0.78	1.86	0.011					0.22
2 nd order Pseudo Kinetics	1.72	1.86	-	0.076				0.97
Intraparticle diffusion	-	-	-	-	0.99	0.060		0.58
Elvioch	-	-	-	-	-	-	4.52	0.60

Kinetic parameters calculated from the slope and intercept of the linear models (Table 25) show that pseudo-2nd order kinetics represents interaction between the Cs-HA and F⁻ better than other models (Fig. 33). Calculated q_e maximum from the model =1.72 mg/g is very

close to the experimental value, $q_e = 1.86 \text{ mg/g}$ with correlation coefficient $R^2=0.97$. The rest of the models gave $R^2 < 0.7$.

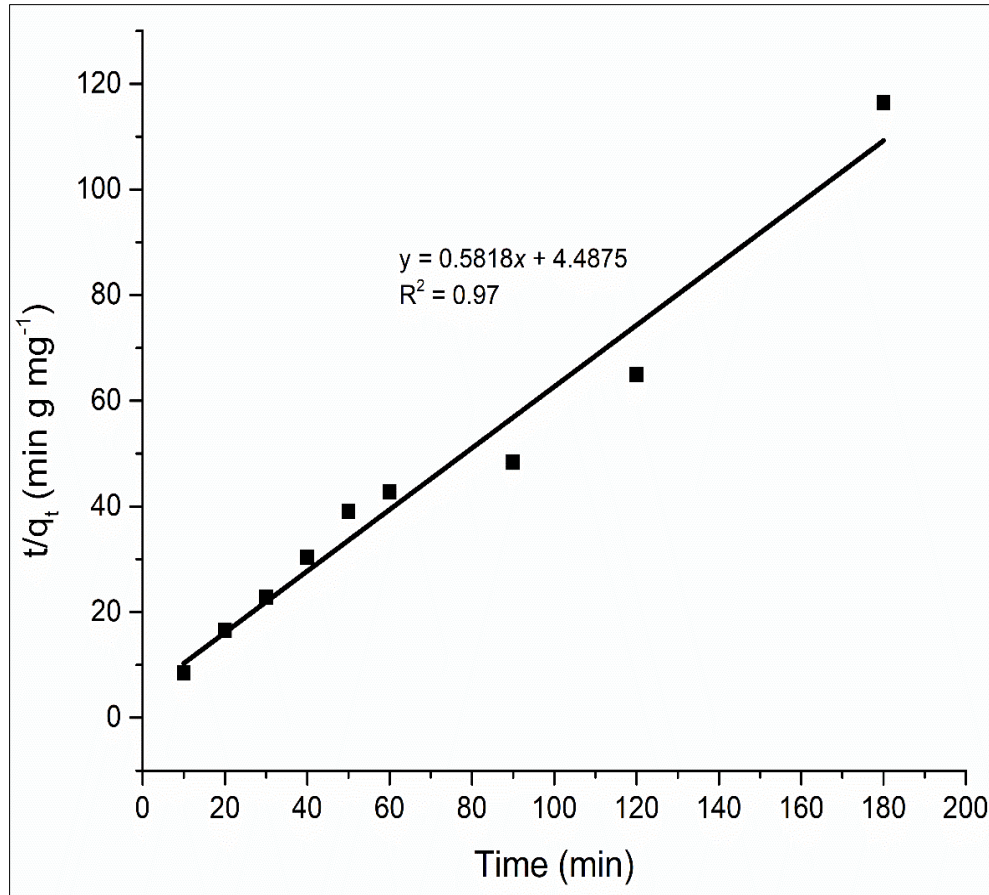


Figure 33: Pseudo-2nd order kinetic plot for fluoride adsorption on Cs-HA.

4.3.6 Effect of temperature and thermodynamic parameters

Influence of temperature on the adsorption of F^- was verified at temperatures of 300-330 K using field water sample at its natural pH for 180 minutes (Fig. 34). The adsorption of F^- was independent of temperature below 313 K. A similar observation has been made for bone char, the F^- removal remained constant for temperature range 288-308 K (Medellin-

Castillo *et al.*, 2007). The observation can be seen to indicate that the uptake of F⁻ below 313 K is dominantly by exchange of F⁻ ion from solution to the surface of Cs-HA.

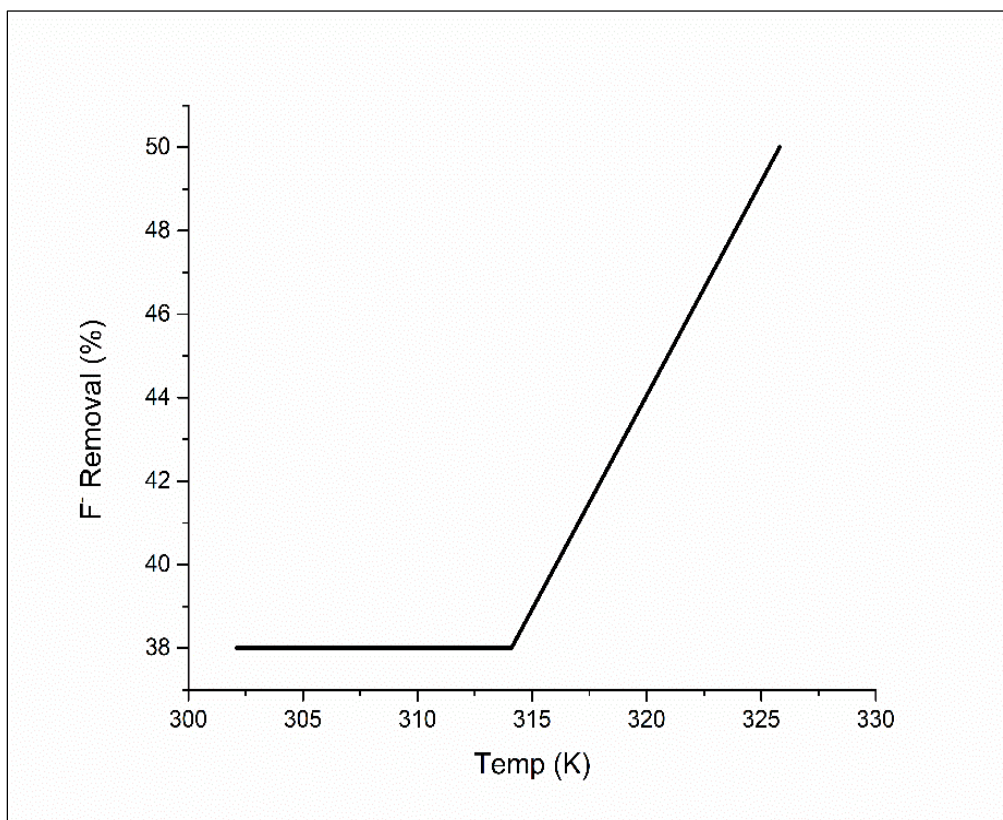


Figure 34: Variation of F⁻ removal with temperature of the medium.

Thermodynamic parameters (Table 26) calculated from slope and intercept of Van't Hoff plot (Fig. 35) show positive ΔG value, signifying that the adsorption process was nonspontaneous. Positive value of ΔH suggested endothermic nature of adsorption process. The negative value of $\Delta S \ll \ll \ll 1$ suggested a slight changes in randomness occur at the solid/liquid interface during the adsorption process.

Table 26: Thermodynamic parameters of interaction of F⁻ with Cs-HA.

F ⁻ initial (mg/l)	Temp (K)	ΔG (kJ mol ⁻¹)	ΔH (kJ mol ⁻¹)	ΔS (kJ mol ⁻¹ K ⁻¹)
25.6	302	5.33	17.34	0.039
	307	5.32		
	314	5.45		

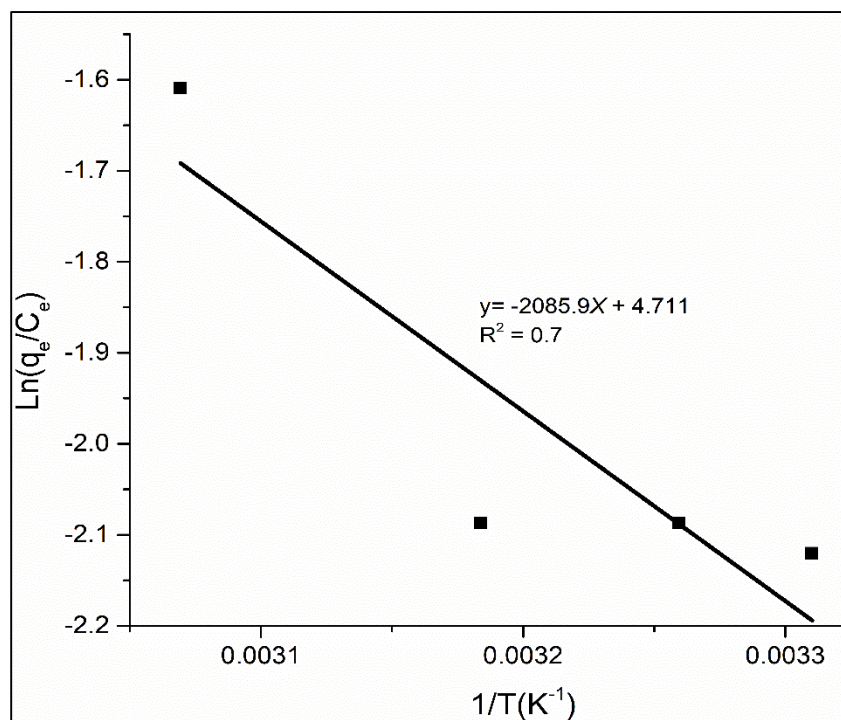


Figure 35: Van't Hoff plot for F⁻ adsorption on Cs-HA.

4.3.7 Proposed mechanism

F⁻ removal mechanism was predicted from FT-IR and adsorption analysis. FT-IR spectra (Fig. 27) confirmed shift of apatite OH bands at 571-645 cm⁻¹ to longer wavenumbers accompanied by decrease in intensity after F⁻ adsorption. This was assumed to indicate F⁻ substitution and formation of fluorapatite. This reaction was favored by the fact that both F⁻ and OH⁻ are isoelectronic with comparable ionic radius, thus ion exchange can happen forming a strong chemical bond with Ca²⁺ cations (Loganathan *et al.*, 2013). Increase in equilibrium pH after treatment was seen to ratify release of OH⁻ into solution from Eq. (7). Adsorption efficiency increased tremendously at low pH (3-5). This was attributed to protonation of large amounts of OH and NH₂ surface sites on the composite resulting to enhanced adsorption by electrostatic attraction. Presence of OH----F and NH----F vibrations in FT-IR spectrum also confirms this observation. We thus conclude that ion

exchange and electrostatic attraction are the driving force in the uptake of F^- by Cs-HA composite.

4.4 Conclusion

Brushite derived from crab shell waste was transformed into nano-structured chitosan-hydroxyapatite composite using wet chemistry precipitation method. Analytical characterization using XRD and FT-IR confirmed the transformation and nanocrystallite size (~ 27 nm). Highest fluoride adsorption capacity of 3.7 mg/g was reached for field water and 6.4 mg/g using simulated water samples of F^- concentration 5-100 mgF/L. The Adsorbate –adsorbent interaction was best described by Temkin adsorption isotherm and pseudo 2nd order kinetics. The adsorption process was highly affected by the pH of the medium, with the highest performance reached at pH =3. A closer look indicates the Cs-HA would efficiently treat field water with F^- levels of $F^- \leq 10$ mg/L and below to achieve WHO recommended 1.5 mg/l. The adsorbent also removed microbes and improved the appearance of tinted water. Unlike many adsorbent reported in literature, this biogenically derived adsorbent maintained the pH of treated water within 6-9, which is recommended for drinking water.

CHAPTER FIVE

General Discussion, Conclusion and Recommendations

5.1 General Discussion

The overall objective of this research was to develop low cost, efficient and sustainable material for defluoridation of drinking water in East African Rift Valley. Use of locally abundant crustacean biomass waste generated from sea food industry was evaluated as resource for development of adsorbents for high fluoride ground and surface waters. The targeted biomaterials were chitosan and calcium precursor for development of calcium phosphate and composite system adsorbents.

A brief survey of the availability and sustainability of crustacean biomass waste was carried out. Potential recovery of bioactive components from biomass waste was evaluated in the laboratory. Data indicated that Tanzanian coast produced at least 66 tons of prawns shell on dry basis in 2013 alone. These wastes have not been exploited for production of any bioactive components so far. Instead, it is mostly left to rot in the ocean. Laboratory analysis indicated that in 2013, there was potential to produce over 10 metric tonnes of high quality chitosan, 23 tons of CaCO_3 and 27 tons of protein, if the wastes were recycled appropriately. In this work, crustacean wastes were used to develop three adsorbent materials; chitosan, calcium phosphates, and chitosan - hydroxyapatite composite. Each of the adsorbent was tested for fluoride removal in batch mode using field water with predetermined quality parameters; color, microbes, electroconductivity and total dissolved solids.

Chitosan was isolated from prawns shell and modified by crosslinking with glutaraldehyde and protonation with concentrated hydrochloric acid. Physical properties of chitosan and its interaction with fluoride ions was studied using computational density functional theory and experimental FT-IR, CHNS/O analysis and XRD. Protonated chitosan was found to be more effective than unprotonated chitosan in F^- adsorption from both computational and experimental data.

The protonated chitosan was only effective with water of fluoride concentration below 5 mg/l at pH 7. The treated water was slightly acidic at pH 6 - 6.3. The requirement for pH adjustment after decontaminated water was found to limit the use of chitosan in household applications. Another adsorbent was developed using the Ca^{2+} recovered from demineralization of the shells. The calcium obtained was reacted with PO_4^{3-} to obtain calcium phosphates (CAPs) derived from crabs and prawns shells. The CAPs were analysed using XRD, FT-IR and EDX. Crab shell CAP was indexed as nanocrystalline mixed phases with predominately brushite structure substituted with trace levels of Sr^{2+} , Mn^{2+} , Si^{4+} , and K^+ . Prawns derived CAP was identified as pure nanocrystalline hydroxyapatite with traces of Sr^{2+} and K^+ . Its structure agreed well with that of synthetic hydroxyapatite. Fluoride removal capacities of crustacean CAPs was excellent compared to synthetic hydroxyapatite or bone char. Crab shell derived adsorbent was the most effective, with fluoride as high as 70 mg/l being reduced to 2 mg/l and color tint in surface water significantly reduced to acceptable level. CAPs synthesized were able to maintain the pH of the treated water to acceptable levels of 6.5-9. The order of effectiveness for the CAPs can be summarized as crab shell CAP > prawns shell CAP > synthetic CAP > bone char. The main limitation of CAP systems was failure to remove microbes from treated water.

To improve the limitations of chitosan (low F^- adsorption capacity and pH adjustment) and those of CAPs (lack of microbial activity). A composite of chitosan and crab shell calcium phosphate was prepared. The formation of composite was confirmed by FT-IR and XRD analysis. The composite was found to be effective in fluoride removal from field water of concentration ≤ 10 mg/l in addition to removal of microbes and light tint in surface water. The mechanism of F^- removal for all the adsorbent was controlled by pseudo second order kinetics. The optimum pH range for best performance was deduced as pH = 3 - 5 and temperature of 30 - 35 °C.

A Comparison of adsorbents performance with others reported in literature is shown in Table 27. It can be seen that most adsorbents reported with high adsorption capacities have only been tested with simulated water. However, the findings of this work indicate that adsorption capacity in field water is much lower than in simulated water.

This was attributed to interference by other parameters such as pH, turbidity, presence of organics and inorganics in field waters. In all the literature reviewed, the pH was adjusted to 3 - 5 in order to achieve the high capacities reported.

Table 27: Fluoride adsorption capacities on various adsorbent materials.

Adsorbent	F ⁻ initial/source	Adsorbent loading	Q _e (mg/g)	Reference
Phosphogypsum HAP	50 mg/l- NaF	0.1-1 g/100 ml	19.7	(Zhang <i>et al.</i> , 2012)
HAP-nano wires	200 mg/l NaF	5.00 mg/10 ml	40.7	(He <i>et al.</i> , 2016)
Nano-HAP	10 mg/l –NaF 2.3 mg/l - field	0.25 g/50 ml	1.9 0.4	(Sundaram <i>et al.</i> , 2008a)
Nano sized - HAP	95 mg/l-NaF	2.00 g/1000 ml	11.0	(Sternitzke <i>et al.</i> , 2012)
Mg/Ce/Mn/O-DE	100 mg/l -NaF	0.60 g/100 ml	12.6	(Gitari <i>et al.</i> , 2017)
Heat activated dolomite	500 mg/l-NaF	2.00 g/1000 ml	243.0	(Prasad, 2015)
Bone char	4.0 mg/l-field	1.00 g/480 ml	1.9	(Medellin-Castillo <i>et al.</i> , 2007)
Crab shell -CAP	106 mg/l –NaF 70 mg/l- field	0.25 g/50 ml	21.0 13.5	This study
Prawn shell - CAP	106 mg/l –NaF 70 mg/l- field	0.25 g/50 ml	10.0 8.5	This study
Nano-HAP/chitosan	10 mg/l –NaF 2.33 mg/l - field	0.25 g/50 ml	1.6 0.4	(Sundaram <i>et al.</i> , 2008b)
Chitosan-crab shell HAP	106 mg/l –NaF 70 mg/l- field	0.25 g/50 ml	6.5 6.4	This study
PCB	10 mg/l –NaF	0.25 g/50 ml	1.7	(Viswanathan <i>et al.</i> , 2009a)
PCCs	10 mg/l -NaF	0.25 g/50 ml	1.6	This study

In this work the adsorption capacities of developed adsorbents is reported at the natural environment of fluoride polluted water, no parameters such as pH and temperature were adjusted. This shows that adsorbents be easily applied in defluoridation without other cost of adjusting parameters. The fact CAPs and composite in this work were substituted with traces Sr^{2+} , Mn^{2+} , Si^{4+} , and K^{+} as seen in EDX analysis could have contributed to their better F^{-} adsorption performance as compared to synthetic adsorbents reported in literature, which were purely Ca^{2+} phosphates, mostly hydroxyapatites. Adsorbents developed from crustacean biomass in this work are thus considered superior in treating field water with high fluoride concentration.

5.2 Conclusion

Three adsorbent materials namely, modified chitosan, calcium phosphate systems and composite of calcium phosphate and chitosan were developed from crustacean biomass waste. Each of the adsorbents was characterized and tested for F^{-} removal using batch adsorption tests. The following conclusion were drawn from the results obtained:

Chitosan, which was modified by crosslinking and protonation of the amine groups into PCCs possessed higher F^{-} adsorption capacity than unmodified chitosan. This conclusion was further supported by DFT analysis which showed that protonated β -GlcN had better ability of binding F^{-} than its unprotonated form. The electropositivity of H atoms attached to OH and NH_2 functional groups and the dipole moment of the molecule were shown to highly influence the efficiency of F^{-} binding by electrostatic attraction mechanism. The best adsorption capacity for PCCs recorded was 1.6 mg/l at efficiency of 77%, indicating that PCCs adsorbent would be most appropriate for treating low F^{-} polluted waters (> 5 mg/l).

Two forms CAPs adsorbents developed from crustacean waste had superior defluoridation capacities as compared to synthetic hydroxyapatite (CCHA) adsorbents. Crab shell derived CHA was the most effective adsorbent with highest adsorption capacity of 13.5 mg/g compared to 8.5mg/g and 2.6 mg/g for PHA and CCHA, respectively. Anion exchange was proposed as the main driving force in F^{-} uptake followed by slow adsorption process.

Overall, results indicate that PHA would be most suitable for treating water with F⁻ concentration of 10 mg/l and below while CHA can effectively treat water at higher levels, up to 70 mg/l, with efficiency of over 95%. A slight increase in phosphate level and failure to remove microbes were identified as limitations of the CAPs adsorbents.

Cs-HA composite was seen as a compromise between low efficiency of chitosan and microbial inactivity of CAPS. The best adsorption efficiencies, > 85% were achieved for waters with F⁻ concentration below 10 mg/l. This adsorbent would thus effectively treat water contaminated with microbes and F⁻ in the range of 2-10 mg/l to achieve WHO recommended 1.5 mg/l. Possible mechanisms of fluoride adsorption was predicted as ion exchange and electrostatic attraction via the NH₂ groups of chitosan.

5.3 Recommendations

This research work have developed adsorbent materials that are highly efficient for defluoridation of drinking water with varied concentration, 5 -70 mg/l. It was also shown that different materials are applicable in water of different level of F⁻ contamination. However, for the materials developed here work to be applicable for up-scaling into community filter, more test are required in the following areas:

Testing of the adsorbents in column experiments, which are more applicable in household water treatment setting. The adsorbent tested in the batch experiment mode were in form of fine power that would result to clogging and pressure drops in continuous flow condition. For applicability in column defluoridation, granular form of the adsorbent could be investigated and tested at different flow rates.

Optimization test, to determine the best combination of variables for highest F⁻ adsorption. The findings of this work clearly indicated that adsorption in batch mode followed pseudo 2nd order kinetics, meaning that concentration of F⁻ and adsorbent influenced the rates of adsorption. Also, effects of pH, temperature and contact time were demonstrated.

However, the most suitable combination of the different variables could be worth perusing in details, probably using response surface methodology to clearly understand the applicability of the adsorbent in different situations.

Field water treated with developed adsorbent was analyzed for F^- , phosphates, and microbes before and after treatment. Profiling of the samples with ICP to provide elemental fingerprint of the water in terms trace metal element composition and how the concentration of each element is affected upon interaction with various adsorbent would be important. The information obtained can serve as quality assurance for the suitability of defluoridated water for human consumption.

Regeneration study to investigate usability and lifetime of the material. The CAPs and composite were found to uptake F^- by substitution of OH^- or HPO_4^{2-} with F^- , to form $Ca_{10}(PO_4)_6F_2$. Regeneration studies would then mean working to in the reverse reaction to exchange F^- with OH^- . A detailed study of the chemistry of this reverse reaction is important to understand conditions that would allow generation of fluorapatite and the number of cycles that can be useful for effective defluoridation.

REFERENCES

- Abdou, E.S., Nagy, K.S. and Elsabee, M.Z. (2008). Extraction and characterization of chitin and chitosan from local sources. *Bioresour Technol*. **99**(5): 1359-67.
- Abueva, C.D., Jang, D-W., Padalhin, A. and Lee, B-T. (2017). Phosphonate-chitosan functionalization of a multi-channel hydroxyapatite scaffold for interfacial implant-bone tissue integration. *Journal of Materials Chemistry B*. **5**(6): 1293-1301.
- Akram, M., Ahmed, R., Shakir, I., Ibrahim, W.A. and Hussain, R. (2014). Extracting hydroxyapatite and its precursors from natural resources. *Journal of Materials Science*. **49**(4): 1461-1475.
- Alagumuthu, G. and Rajan, M. (2010). Equilibrium and kinetics of adsorption of fluoride onto zirconium impregnated cashew nut shell carbon. *Chemical Engineering Journal*. **158**(3): 451-457.
- Albertus, J., Bregnhøj, H. and Kongpun, M. (Ed.) (2000). Bone char quality and defluoridation capacity in contact precipitation. *In: 3rd International Workshop on Fluorosis Prevention and Defluoridation of Water*, pp. 61-72, 2000.
- Alkan, E., Kır, E. and Oksuz, L. (2008). Plasma modification of the anion-exchange membrane and its influence on fluoride removal from water. *Separation and Purification Technology*. **61**(3): 455-460.
- Altomare, A., Cuocci, C., Giacobazzo, C., Moliterni, A., Rizzi, R., Corriero, N. and Falcicchio, A. (2013). EXPO2013: a kit of tools for phasing crystal structures from powder data. *Journal of Applied Crystallography*. **46**(4): 1231-1235.
- Anastopoulos, I. and Kyzas, G. (2016). Are the thermodynamic parameters correctly estimated in liquid-phase adsorption phenomena? *Journal of Molecular Liquids*. **218**(1):174-185.

- Anderson, N.P., Hart, J.M., Sullivan, D.M., Horneck, D.A., Pirelli, G.J. and Christensen, N.W. (2013). Applying lime to raise soil pH for crop production (Western Oregon). Corvallis: Extension Service, Oregon State University. 45-66 pp.
- Araújo, J.V., Lopes da Silva, J.A., Almeida, M.M. and Costa, M.E. (2006). Preparation and characterization of chitosan-based scaffolds for biomedical applications. *Materials Science Forum*. **514-516**(4): 1005-1009.
- Arbia, W., Arbia, L., Adour, L. and Amrane, A. (2013). Chitin extraction from crustacean shells using biological methods—a review. *Food Technology and Biotechnology*. **51**(1): 12-25.
- Aynew, T. (2008). The distribution and hydrogeological controls of fluoride in the groundwater of central Ethiopian rift and adjacent highlands. *Environmental Geology*. **54**(6): 1313-1324.
- Ayoob, S. and Gupta, A. (2008). Insights into isotherm making in the sorptive removal of fluoride from drinking water. *Journal of Hazardous Materials*. **152**(3): 976-985.
- Ayoob, S., Gupta, A.K., Bhakat, P.B. and Bhat, V.T. (2008). Investigations on the kinetics and mechanisms of sorptive removal of fluoride from water using alumina cement granules. *Chemical Engineering Journal*. **140**(1): 6-14.
- Becke, A.D. (1993). Density-functional thermochemistry. III. The role of exact exchange. *The Journal of Chemical Physics*. **98**(7): 5648-5652.
- Brugnerotto, J., Lizardi, J., Goycoolea, F.M., Argüelles-Monal, W., Desbrières, J. and Rinaudo, M. (2001). An infrared investigation in relation with chitin and chitosan characterization. *Polymer*. **42**(8): 3569-3580.
- Cahú, T.B., Santos, S.D., Mendes, A., Córdula, C.R., Chavante, S.F., Carvalho, L.B., Nader, H.B. and Bezerra, R.S. (2012). Recovery of protein, chitin, carotenoids and glycosaminoglycans from Pacific white shrimp (*Litopenaeus vannamei*) processing waste. *Process Biochemistry*. **47**(4): 570-577.

- Chandur, V., Badiger, A. and Shambashiva, R. (2011). Characterizing formulations containing derivatized chitosan with polymer blending. *International Journal of Research in Pharmacy Chemistry*. **4**(1): 950-967.
- Chen, A-H. and Chen, S-M. (2009). Biosorption of azo dyes from aqueous solution by glutaraldehyde-crosslinked chitosans. *Journal of Hazardous Materials*. **172**(2): 1111-1121.
- Chen, F., Wang, Z.-C. and Lin, C.-J. (2002). Preparation and characterization of nano-sized hydroxyapatite particles and hydroxyapatite/chitosan nano-composite for use in biomedical materials. *Materials Letters*. **57**(4): 858-861.
- Chen, X. (2015). Modeling of experimental adsorption isotherm data. *Information*. **6**(1): 14-22.
- Chibole, O. (1987). Epidemiology of dental fluorosis in Kenya. *Journal of the Royal Society of Health*. **107**(6): 242-243.
- Dahi, E. (2016). Africa's u-turn in defluoridation policy: from the Nalgonda technique to bone char. 401-416 pp.
- Danilchenko, S.N., Kalinkevich, O.V., Pogorelov, M.V., Kalinkevich, A.N., Sklyar, A.M., Kalinichenko, T.G., Ilyashenko, V.Y., Starikov, V.V., Bumeyster, V.I., Sikora, V.Z. and Sukhodub, L.F. (2011). Characterization and in vivo evaluation of chitosan-hydroxyapatite bone scaffolds made by one step coprecipitation method. *Journal of Biomedical Materials Research A*. **96**(4): 639-47.
- de Queiroz Antonino, R.S., Fook, B.P., de Oliveira, V.A., de Farias, R. Í., Lima, E.N., da Silva, R.J., Peniche, C. A. and Fook, M.V. (2017). Preparation and characterization of chitosan obtained from shells of shrimp (*Litopenaeus vannamei* Boone). *Marine Drugs*. **15**(5): 141-151.
- Demirbas, E., Kobya, M., Senturk, E. and Ozkan, T. (2004). Adsorption kinetics for the removal of chromium (VI) from aqueous solutions on the activated carbons prepared from agricultural wastes. *Water Sanitation*. **30**(4): 533-539.

- Diawara, C.K. (2008). Nanofiltration process efficiency in water desalination. *Separation and Purification Reviews*. **37**(3): 302-324.
- Dissanayake, C.B. (1991). The fluoride problem in the ground water of Sri Lanka-environmental management and health. *International Journal of Environmental Studies*. **38**(2-3): 137-155.
- El Knidri, H., El Khalfaouy, R., Laajeb, A., Addaou, A. and Lahsini, A. (2016). Eco-friendly extraction and characterization of chitin and chitosan from the shrimp shell waste via microwave irradiation. *Process Safety and Environmental Protection*. **104**(5):395-405.
- Fattahi, A., Ghorat, M., Pourjavadi, A., Kurdtabar, M. and Torabi, A. (2008). DFT/B3LYP study of thermochemistry of D-Glucosamine, a representative polyfunctional bioorganic compound. *Scientia Iranica*. **15**(4): 422-429.
- Fawell, J. and Bailey, K. (2006). Fluoride in drinking-water. World Health Organization 65pp.
- Foo, K. and Hameed, B. (2010). Insights into the modeling of adsorption isotherm systems. *Chemical Engineering Journal*. **156**(1): 2-10.
- Freund, F. and Knobel, R.M. (1977). Distribution of fluorine in hydroxyapatite studied by infrared spectroscopy. *Journal of the Chemical Society, Dalton Transactions*11(4): 1136-1140.
- Gao, S., Sun, R., Wei, Z., Zhao, H., Li, H. and Hu, F. (2009). Size-dependent defluoridation properties of synthetic hydroxyapatite. *Journal of Fluorine Chemistry*. **130**(6): 550-556.
- Ghiglieri, G., Balia, R., Oggiano, G. and Pittalis, D. (2010). Prospecting for safe (low fluoride) groundwater in the Eastern African Rift: the Arumeru District (Northern Tanzania). *Hydrology and Earth System Sciences Discussions*. **14**(6): 1081-1091.

- Ghiglieri, G., Pittalis, D., Cerri, G. and Oggiano, G. (2012). Hydrogeology and hydrogeochemistry of an alkaline volcanic area: the NE Mt. Meru slope (East African Rift–Northern Tanzania). *Hydrology and Earth System Sciences*. **16**(2): 529-541.
- Gitari, W.M., Izuagie, A.A. and Gumbo, J.R. (In press). Synthesis, characterization and batch assessment of groundwater fluoride removal capacity of trimetal Mg/Ce/Mn oxide-modified diatomaceous earth. *Arabian Journal of Chemistry*. <http://dx.doi.org/10.1016/j.arabjc.2017.01.002>.
- Goncharuk, V., Bagrii, V., Mel'nik, L., Chebotareva, R. and Bashtan, S.Y. (2010). The use of redox potential in water treatment processes. *Journal of Water Chemistry and Technology*. **32**(1): 1-9.
- Granovsky, A. (2008). Firefly version 8.1.1 <http://classic.chem.su/grad/firefly/index.html>
- Günay, A., Arslankaya, E. and Tosun, I. (2007). Lead removal from aqueous solution by natural and pretreated clinoptilolite: adsorption equilibrium and kinetics. *Journal of Hazardous Materials*. **146**(1): 362-371.
- Guo, Y-P., Guan, J-J., Yang, J., Wang, Y., Zhang, C-Q. and Ke, Q-F. (2015). Hybrid nanostructured hydroxyapatite–chitosan composite scaffold: bioinspired fabrication, mechanical properties and biological properties. *Journal of Materials Chemistry B*. **3**(23): 4679-4689.
- Habuda-Stanić, M., Ravančić, M.E. and Flanagan, A. (2014). A review on adsorption of fluoride from aqueous solution. *Materials*. **7**(9): 6317-6366.
- Hanwell, M.D., Curtis, D.E., Lonie, D.C., Vandermeersch, T., Zurek, E. and Hutchison, G.R. (2012). Avogadro: an advanced semantic chemical editor, visualization, and analysis platform. *Journal of Cheminformatics*. **4**(1): 17-25.

- Haule, W.V. (2001). The United Republic of Tanzania. Reducing the impact of tropical shrimp trawling fisheries on living marine resources through the adoption of environmentally friendly techniques and practices in Tanzania. *FAO Fisheries and Aquaculture Circular*. **974**(6): 216-233.
- He, G. and Cao, S. (1996). Assessment of fluoride removal from drinking water by calcium phosphate systems. *Fluoride*. **29**(4): 212-216.
- He, J., Zhang, K., Wu, S., Cai, X., Chen, K., Li, Y., Sun, B., Jia, Y., Meng, F. and Jin, Z. (2016). Performance of novel hydroxyapatite nanowires in treatment of fluoride contaminated water. *Journal of Hazardous Materials*. **303**(4): 119-130.
- Hou, H., Zhou, R., Wu, P. and Wu, L. (2012). Removal of Congo red dye from aqueous solution with hydroxyapatite/chitosan composite. *Chemical Engineering Journal*. **211** (Supplement C): 336-342.
- Hu, H., Xin, J.H., Hu, H., Chan, A. and He, L. (2013). Glutaraldehyde–chitosan and poly (vinyl alcohol) blends, and fluorescence of their nano-silica composite films. *Carbohydrates Polymer*. **91**(1): 305-313.
- Huang, R., Yang, B., Liu, Q. and Ding, K. (2012). Removal of fluoride ions from aqueous solutions using protonated cross-linked chitosan particles. *Journal of Fluorine Chemistry*. **141**(7): 29-34.
- Ioku, K. (1998). Preparation and application of calcium phosphate fibers, In: Amjad, Z. (Ed.), Calcium phosphates in biological and industrial systems. Springer US, Boston, pp. 357-369.
- Islam, M. and Patel, R. (2011). Thermal activation of basic oxygen furnace slag and evaluation of its fluoride removal efficiency. *Chemical Engineering Journal*. **169**(1): 68-77.
- Jagtap, S., Thakre, D., Wanjari, S., Kamble, S., Labhsetwar, N. and Rayalu, S. (2009). New modified chitosan-based adsorbent for defluoridation of water. *Journal of Colloid and Interface Science*. **332**(2): 280-290.

- Kashkarov, V., Goloshchapov, D., Romyantseva, A., Seredin, P., Domashevskaya, E., Spivakova, I. and Shumilovich, B. (2011). X-ray diffraction and IR spectroscopy investigation of synthesized and biogenic nanocrystalline hydroxyapatite. *Journal of Surface Investigation: X-ray, Synchrotron and Neutron Techniques*. **5**(6): 1162-1167.
- Khairnar, M.R., Dodamani, A.S., Jadhav, H.C., Naik, R.G. and Deshmukh, M.A. (2015). Mitigation of Fluorosis - A Review. *Journal of Clinical and Diagnostic Research*. **9**(6): 5-9.
- Kinniburgh, D.G. (1986). General purpose adsorption isotherms. *Environmental Science and Technology*. **20**(9): 895-904.
- Kucukgulmez, A., Celik, M., Yanar, Y., Sen, D., Polat, H. and Kadak, A.E. (2011). Physicochemical characterization of chitosan extracted from *Metapenaeus stebbingi* shells. *Food Chemistry*. **126**(3): 1144-1148.
- Kumar, K.V. and Sivanesan, S. (2005). Prediction of optimum sorption isotherm: Comparison of linear and non-linear method. *Journal of Hazardous Materials*. **126**(3): 198-201.
- Kumar, S. and Gopal, K. (2000). A review on fluorosis and its preventive strategies. *Indian Journal of Environmental Protection*. **20**(6): 430-440.
- Larsen, M. and Pearce, E. (2002). Defluoridation of drinking water by boiling with brushite and calcite. *Caries Research*. **36**(5): 341-346.
- Lertworasirikul, A., Yokoyama, S., Noguchi, K., Ogawa, K. and Okuyama, K. (2004). Molecular and crystal structures of chitosan/HI type I salt determined by X-ray fiber diffraction. *Carbohydrate Research*. **339**(4): 825-833.
- Li, Z., Yubao, L., Aiping, Y., Xuelin, P., Xuejiang, W. and Xiang, Z. (2005). Preparation and in vitro investigation of chitosan/nano-hydroxyapatite composite used as bone substitute materials. *Journal of Materials Science: Materials in Medicine*. **16**(3): 213-219.

- Liang, P., Zhang, Y., Wang, D., Xu, Y. and Luo, L. (2013). Preparation of mixed rare earths modified chitosan for fluoride adsorption. *Journal of Rare Earths*. **31**(8): 817-822.
- Liu, D., Wei, Y., Yao, P. and Jiang, L. (2006). Determination of the degree of acetylation of chitosan by UV spectrophotometry using dual standards. *Carbohydrates Research*. **341**(6): 782-785.
- Loganathan, P., Vigneswaran, S., Kandasamy, J. and Naidu, R. (2013). Defluoridation of drinking water using adsorption processes. *Journal of Hazardous Materials*. **248**(2): 1-19.
- Lu, Y., Sun, Z., Wu, L., Wang, X., Lu, W. and Liu, S. (2000). Effect of high-fluoride water on intelligence in children. *Fluoride*. **33**(2): 74-78.
- Mane, V.S., Mall, I.D. and Srivastava, V.C. (2007). Use of bagasse fly ash as an adsorbent for the removal of brilliant green dye from aqueous solution. *Dyes and Pigments*. **73**(3): 269-278.
- Mariappan, P. and Vasudevan, T. (2002). Domestic defluoridation techniques and sector approach for fluorosis mitigation. *TWAD Newsletter*.
- Marwa, E. (2016). Quantum chemical study of sodium cation and fluoride anion attachment to the chitosan constituents. Unpublished Dissertation for Award of MSc Degree at NM-AIST. Arusha, Tanzania, pp. 36 – 47.
- Medellin-Castillo, N.A., Leyva-Ramos, R., Ocampo-Perez, R., Garcia de la Cruz, R.F., Aragon-Pina, A., Martinez-Rosales, J.M., Guerrero-Coronado, R.M. and Fuentes-Rubio, L. (2007). Adsorption of fluoride from water solution on bone char. *Industrial and Engineering Chemistry Research*. **46**(26): 9205-9212.
- Meenakshi, S. and Maheshwari, R.C. (2006). Fluoride in drinking water and its removal. *Journal of Hazardous Materials*. **137**(1): 456-463.

- Meta, M. (2014). Improving access to safe drinking water: Prospection for low-fluoride sources. Brief report presenting main findings. Natural Environment Research Council. 67-82 pp.
- Miretzky, P. and Cirelli, A.F. (2011). Fluoride removal from water by chitosan derivatives and composites: A review. *Journal of Fluorine Chemistry*. **132**(4): 231-240.
- Modi, S. and Soni, R. (2013). Merits and demerits of different technologies of defluoridation for drinking water. *Journal of Environmental Science, Toxicology and Food Technol* . **3**(4): 24-27.
- Mohapatra, M., Anand, S., Mishra, B.K., Giles, D.E. and Singh, P. (2009). Review of fluoride removal from drinking water. *Journal of Environmental Management*. **91**(1): 67-77.
- Mourabet, M., El Boujaady, H., El Rhilassi, A., Ramdane, H., Bennani-Ziatni, M., El Hamri, R. and Taitai, A. (2011). Defluoridation of water using brushite: equilibrium, kinetic and thermodynamic studies. *Desalination*. **278**(1): 1-9.
- Mourabet, M., El Rhilassi, A., El Boujaady, H., Bennani-Ziatni, M. and Taitai, A. (2017). Use of response surface methodology for optimization of fluoride adsorption in an aqueous solution by Brushite. *Arabian Journal of Chemistry*. **10**(2): S3292-S3302.
- Namin, H. E., Hashemipour, H. and Ranjbar, M. (2008). Effect of aging and calcination on morphology and properties of synthesized nanocrystalline TiO₂. *International Journal of Modern Physics B*. **22**(19): 3210-3215.
- Panda, R., Hsieh, M., Chung, R. and Chin, T. (2003). FTIR, XRD, SEM and solid state NMR investigations of carbonate-containing hydroxyapatite nano-particles synthesized by hydroxide-gel technique. *Journal of Physics and Chemistry of Solids*. **64**(2): 193-199.
- Peña, I., Kolesniková, L., Cabezas, C., Bermúdez, C., Berdakin, M., Simão, A. and Alonso, J.L. (2014). The shape of D-glucosamine. *Physical Chemistry Chemical Physics*. **16**(42): 23244-23250.

- Perdew, J. P. (1986). Density-functional approximation for the correlation energy of the inhomogeneous electron gas. *Physical Review B*. **33**(12): 8822-8834.
- Phantumvanit, P., Songpaisan, Y. and Moller, I. (1988). A defluoridator for individual households. *World Health Forum*. **9**(4): 555-558.
- Piddennavar, R. and Krishnappa, P. (2013). Review on defluoridation techniques of water. *International Journal of Engineering Science*. **2**(2): 86-94.
- Pighinelli, L. and Kucharska, M. (2013). Chitosan-hydroxyapatite composites. *Carbohydrates Polymer*. **93**(1): 256-62.
- Poinern, G.J., Ghosh, M.K., Ng, Y-J., Issa, T.B., Anand, S. and Singh, P. (2011). Defluoridation behavior of nanostructured hydroxyapatite synthesized through an ultrasonic and microwave combined technique. *Journal of Hazardous Materials*. **185**(1): 29-37.
- Prabhu, S.M., Viswanathan, N. and Meenakshi, S. (2014). Defluoridation of water using chitosan assisted ethylenediamine functionalized synthetic polymeric blends. *International Journal of Biological Macromolecules*. **70**(5): 621-627.
- Prasad, V. (2015). Rapid removal of fluoride from aqueous media using activated dolomite. *Analytical Methods*. **7**(3): 48304-8312.
- Prashanth, K.H., Kittur, F. and Tharanathan, R. (2002). Solid state structure of chitosan prepared under different N-deacetylating conditions. *Carbohydrates-Polymer*. **50**(1): 27-33.
- Qiu, H., Liv, L., Pan, B., Zhang, Q., Zhang, W. and Zhang, Q. (2009). Critical review in adsorption kinetic models. *Journal of Zhejiang University-science A*. **10**(5): 716-724.
- Radin, S. and Ducheyne, P. (1993). The effect of calcium phosphate ceramic composition and structure on in vitro behavior. II. Precipitation. *Journal of Biomedical Materials Research Part A*. **27**(1): 35-45.

- Rajendran, K. and Dale Keefe, C. (2010). Growth and characterization of calcium hydrogen phosphate dihydrate crystals from single diffusion gel technique. *Crystal Research and Technology*. **45**(9): 939-945.
- Roche, E.H. (1968). A fluoride filter for domestic use. *New Zealand Dental Journal* **64**(294): 18-22.
- Rocliffe, S., Peabody, S., Samoily, M. and Hawkins, J.P. (2014). Towards a network of locally managed marine areas (LMMAs) in the Western Indian Ocean. *PloS one*. **9**(7): e103000.
- Rusu, V.M., Ng, C.-H., Wilke, M., Tiersch, B., Fratzl, P. and Peter, M.G. (2005). Size-controlled hydroxyapatite nanoparticles as self-organized organic-inorganic composite materials. *Biomaterials*. **26**(26): 5414-5426.
- Saber-Samandari, S., Saber-Samandari, S., Nezafati, N. and Yahya, K. (2014). Efficient removal of lead (II) ions and methylene blue from aqueous solution using chitosan/Fe-hydroxyapatite nanocomposite beads. *Journal Environmental Management*. **146**(4): 481-490.
- Sagheer, F.A., Al-Sughayer, M.A., Muslim, S. and Elsabee, M.Z. (2009). Extraction and characterization of chitin and chitosan from marine sources in Arabian Gulf. *Carbohydrates Polymer*. **77**(2): 410-419.
- Schmidt, M., Baldrige, K., Boatz, J., Elbert, S., Gordon, M., Jensen, J., Koseki, S., Matsunaga, N., Nguyen, K., Su, S., Windus, T., Dupuis, M. and Montgomery, J. (1993). General atomic and molecular electronic-structure system. *Journal of Computational Chemistry*. **14**(4): 345-356.
- Sluiter, A., Hames, B., Ruiz, R., Scarlata, C., Sluiter, J. and Templeton, D. (2004). Determination of ash in biomass: LAP-005 NREL analytical procedure. *National Renewable Energy Laboratory*, 89 pp.

- Smedley, P., Nkotagu, H., Pelig-Ba, K., MacDonald, A., Tyler-Whittle, R., Whitehead, E. and Kinniburgh, D. (2002). Fluoride in groundwater from high-fluoride areas of Ghana and Tanzania. Nottingham, UK, British Geological Survey, 74 pp.
- Sternitzke, V., Kaegi, R., Audinot, J.N., Lewin, E., Hering, J.G. and Johnson, C.A. (2012). Uptake of fluoride from aqueous solution on nano-sized hydroxyapatite: examination of a fluoridated surface layer. *Environmental Science Technology*. **46**(2): 802-809.
- Sundaram, C.S., Viswanathan, N. and Meenakshi, S. (2008a). Defluoridation chemistry of synthetic hydroxyapatite at nano scale: equilibrium and kinetic studies. *Journal of Hazardous Materials*. **155**(1): 206-215.
- Sundaram, C.S., Viswanathan, N. and Meenakshi, S. (2008b). Uptake of fluoride by nano-hydroxyapatite/chitosan, a bioinorganic composite. *Bioresour Technol*. **99**(17): 8226-8230.
- Swain, S., Padhi, T., Patnaik, T., Patel, R., Jha, U. and Dey, R. (2010). Kinetics and thermodynamics of fluoride removal using cerium-impregnated chitosan. *Desalination and Water Treatment*. **13**(1-3): 369-381.
- Tafu, M. and Chohji, T. (2006). Reaction between calcium phosphate and fluoride in phosphogypsum. *Journal of the European Ceramic Society*. **26**(4): 767-770.
- Tang, Y., Guan, X., Wang, J., Gao, N., McPhail, M.R. and Chusuei, C.C. (2009). Fluoride adsorption onto granular ferric hydroxide: Effects of ionic strength, pH, surface loading, and major co-existing anions. *Journal of Hazardous Materials*. **171**(1): 774-779.
- Tebo, B.M., Bargar, J.R., Clement, B.G., Dick, G.J., Murray, K.J., Parker, D., Verity, R. and Webb, S.M. (2004). Biogenic manganese oxides: properties and mechanisms of formation. *Annual Review of Earth and Planetary Sciences*. **32**(4): 287-328.

- Terreux, R., Domard, M., Viton, C. and Domard, A. (2006). Interactions study between the copper II ion and constitutive elements of chitosan structure by DFT calculation. *Biomacromolecules*. **7**(1): 31-37.
- Thakre, D., Jagtap, S., Bansiwala, A., Labhsetwar, N. and Rayalu, S. (2010). Synthesis of La-incorporated chitosan beads for fluoride removal from water. *Journal of Fluorine Chemistry*. **131**(3): 373-377.
- Thole, B. (2013). Ground Water Contamination with Fluoride and Potential Fluoride Removal Technologies for East and Southern Africa. In: Imran Ahmad Dar (Ed), *Perspectives in Water Pollution*. IntechOpen. pp. 107-189.
- Venkatesan, J. and Kim, S.-K. (2010). Chitosan composites for bone tissue engineering-an overview. *Marine Drugs*. **8**(8): 2252-2266.
- Viswanathan, N., Pandi, K. and Meenakshi, S. (2014). Synthesis of metal ion entrapped silica gel/chitosan biocomposite for defluoridation studies. *International Journal of Biological Macromolecules*. **70**(6): 347-353.
- Viswanathan, N., Sundaram, C.S. and Meenakshi, S. (2009a). Removal of fluoride from aqueous solution using protonated chitosan beads. *Journal of Hazardous Materials*. **161**(1): 423-30.
- Viswanathan, N., Sundaram, C.S. and Meenakshi, S. (2009b). Sorption behaviour of fluoride on carboxylated cross-linked chitosan beads. *Colloids and Surfaces B: Biointerfaces*. **68**(1): 48-54.
- Wang, L. and Li, C. (2007). Preparation and physicochemical properties of a novel hydroxyapatite/chitosan–silk fibroin composite. *Carbohydrates Polymer*. **68**(4): 740-745.
- Wang, X., Ding, M., Liu, Z. and Wang, D. (2015). Synthesis of a chitosan-based functional biopolymer with both catalytic and binding groups for protein and DNA hydrolysis. *RSC Advances*. **5**(25): 19541-19551.

- WHO (2011). Guidelines for Drinking-water Quality. WHO Press, Geneva , Switzerland. 89-103 pp.
- Wong, Y., Szeto, Y., Cheung, W. and McKay, G. (2004). Adsorption of acid dyes on chitosan-equilibrium isotherm analyses. *Process Biochemistry*. **39**(6): 695-704.
- Yamaguchi, I., Tokuchi, K., Fukuzaki, H., Koyama, Y., Takakuda, K., Monma, H. and Tanaka, J. (2001). Preparation and microstructure analysis of chitosan/hydroxyapatite nanocomposites. *Journal of Biomedical Materials Research Part A*. **55**(1): 20-27.
- Yan, N. and Chen, X. (2015). Don't waste seafood waste: Turning cast-off shells into nitrogen-rich chemicals would benefit economies and the environment. *Nature*. **524**(7564): 155-158.
- Yen, M-T., Yang, J-H. and Mau, J-L. (2009). Physicochemical characterization of chitin and chitosan from crab shells. *Carbohydrates Polymer*. **75**(1): 15-21.
- Yoder, K.M., Mabelya, L., Robison, V.A., Dunipace, A.J., Brizendine, E.J. and Stookey, G.K. (1998). Severe dental fluorosis in a Tanzanian population consuming water with negligible fluoride concentration. *Community Dentistry and Oral Epidemiology*. **26**(6): 382-393.
- Yong Lei, J.-J.G., Wei Chen, Qin-Fei Ke, Chang-Qing Zhangb and Ya-Ping Guo (2015). Fabrication of hydroxyapatite/chitosan porous materials for Pb(II) removal from aqueous solution. *RSC Advances*. **5**(3): 25462-25470.
- Yong, S.K., Shrivastava, M., Srivastava, P., Kunhikrishnan, A. and Bolan, N. (2015). Environmental applications of chitosan and its derivatives. In: Whitacre, D. M. (Ed.), Reviews of environmental contamination and toxicology (233). Springer International Publishing, pp. 1-43.
- Younes, I. and Rinaudo, M. (2015). Chitin and chitosan preparation from marine sources. Structure, properties and applications. *Marine Drugs*. **13**(3): 1133-1174.

Zhang, D., Luo, H., Zheng, L., Wang, K., Li, H., Wang, Y. and Feng, H. (2012). Utilization of waste phosphogypsum to prepare hydroxyapatite nanoparticles and its application towards removal of fluoride from aqueous solution. *Journal of Hazardous Materials*. **241**(4): 418-426.

Zhurko, G.A. (2017). ChemCraft 1.8 <http://www.chemcraftprog.com>.